

Numerical renormalization group studies
in complex quantum impurity systems

Dissertation

zur

Erlangung des Doktorgrades (Dr. rer. nat.)

der

Mathematisch-Naturwissenschaftlichen Fakultät

der

Rheinischen Friedrich-Wilhelms Universität Bonn

vorgelegt von

Christian Kolf

aus Siegburg

Tag der Abgabe: 29.9.2006

Angefertigt mit Genehmigung der Mathematisch-Naturwissenschaftlichen Fakultät
der Rheinischen Friedrich-Wilhelms-Universität Bonn

Diese Dissertation ist auf dem Hochschulschriftenserver der ULB Bonn http://hss.ulb.uni-bonn.de/diss_online elektronisch publiziert.

Ich versichere, dass ich diese Arbeit selbständig verfasst und keine anderen als die angegebenen Quellen und Hilfsmittel benutzt sowie die Zitate kenntlich gemacht habe.

Köln, den 08.12.2006

1. Referent: Prof. Dr. J. Kroha
2. Referent: Prof. Dr. R. Flume

Tag der Prüfung: 6. Dezember 2006

Numerical Renormalization Group studies in complex quantum impurity systems

Christian Kolf



Rheinische Friedrich-Wilhelms-Universität Bonn

Abstract

In this thesis we summarize several theoretical studies in the context of quantum impurity systems. We implement the numerical renormalization group (NRG) technique as a powerful method for the solution of the Kondo and the Anderson impurity model. The extension of the standard NRG, which deals with static properties and the calculation of thermodynamics, towards the calculation of dynamical properties is accurately described in our work.

We study the distribution of the Kondo temperature T_K versus the Kondo coupling strength J in the two-channel Kondo (2CK) model by means of an extended NRG program. We show that a wide distribution of the couplings J leads to a peaked distribution of T_K . This gives an explanation of the zero-bias anomalies measured in quantum point contact experiments.

Conductance measurements in scanning tunneling microscopy (STM) experiments of transition metal impurities on metal surfaces are analyzed in this thesis. By combining correlated electron techniques with density functional calculations we show that the transport occurs through the atomic multi-electron states, and we identify their signature in the STM lineshape. A careful analysis of the different relative strengths of the transmission channels allows to determine the spatial orientation of the atomic orbitals of Kondo atoms on a metal surface. Our interpretation is that the tunneling predominantly occurs into the local orbital, which sticks out most out of the metal surface.

Contents

Introduction	1
1 The Kondo effect	5
1.1 The Kondo problem	5
1.2 The Anderson model	7
1.2.1 The Schrieffer-Wolff transformation	8
1.3 Poor man's scaling	9
1.4 Solution of the Kondo problem	10
1.5 Revival of the Kondo effect	11
2 Solution methods for quantum impurity systems	15
2.1 Other methods for the Kondo problem	16
2.1.1 Bethe Ansatz	16
2.1.2 Density matrix renormalization group (DMRG)	16
2.2 The Non-Crossing Approximation (NCA)	18
2.2.1 Renormalized perturbation theory for the SIAM	18
2.2.2 Pseudoparticle representation and projection onto the physical Hilbert space	18
2.2.3 Conserving approximations: NCA	20
2.2.4 Advanced NCA techniques: SUNCA and CTMA	21
2.2.5 The NCA for multi-orbital Anderson impurities	22
3 The Numerical Renormalization Group (NRG)	25
3.1 The NRG procedure	26
3.1.1 Model Hamiltonian	26
3.1.2 Logarithmic discretization	27
3.1.3 Mapping on a semi-infinite chain	31
3.1.4 Iterative diagonalization	32
3.1.5 Symmetries in the NRG	34
3.1.6 Results of the iterative diagonalization	35
3.2 Measurements with the NRG	36
3.2.1 Fixed points, the free electron Hamiltonian	36

3.2.2	Static properties, thermodynamics	41
3.2.3	Dynamical properties	42
3.3	Extensions	53
3.3.1	Non-equilibrium	53
3.4	Dynamical mean-field theory with the NRG	56
3.4.1	A model for europium oxide (EuO)	56
4	Multi-channel models	59
4.1	Two-channel Kondo effect (2CK)	59
4.1.1	Motivation	59
4.1.2	Solution with the NRG	61
4.1.3	Results and discussion	66
4.1.4	Conclusion and outlook	72
5	Multiorbital Anderson impurities	73
5.1	Experimental/Theoretical Situation	73
5.1.1	The Kondo effect in STM experiments	73
5.1.2	A microscopic theory in the Kondo regime	76
5.2	Motivation	79
5.2.1	A theory for the mixed valence regime	79
5.2.2	Multible Kondo resonances	81
5.3	A more realistic model	82
5.3.1	Method of solution	83
5.4	Results and interpretation	84
6	Summary and Outlook	89
7	Deutsche Zusammenfassung	93
A	Technical details for deriving the NRG equations	97
A.1	Mapping on a semi-infinite chain	97
A.2	Details on the solution by iterative diagonalization	100
B	Details on the two-channel Kondo (2CK) NRG	105
	Bibliography	125

Introduction

To describe the electronic properties of a solid it is important to investigate the different interactions in the system, whereas the Coulomb interaction between the electrons plays the most important role. In many substances, such as metals, the Coulomb interactions are screened as a result of the large extent of the electronic wavefunctions, and thus can be treated with perturbative methods. However, during the last decades, new classes of materials were discovered, where localized electron states mainly determine the physical properties. In such substances, the local Coulomb repulsion U is the highest energy scale in the problem and cannot be treated by perturbative approaches anymore. One characterizes this kind of solids as “strongly correlated systems”.

One example for a strongly correlated system are non-magnetic metals with magnetic impurities. During the last 40 years there has been significant progress in the theory and the experiments of the quantum impurity systems [1], which led to a better understanding of their physical properties. The field of complex many-body phenomena is still a very active field of modern condensed matter research, e. g. in the context of nanotechnology and molecular electronics. A prime example for a strongly correlated model is the *Kondo model*, which was used by Jun Kondo in 1964 [2] to explain the resistance minimum in metals with non-magnetic contaminations. The new arising problem in the explanation was the breakdown of the theory below a characteristic temperature, called the Kondo temperature T_K . Logarithmically diverging terms in the calculations mirrored an infinitely strong coupling of the impurity to the surrounding conduction electrons, leading to a singlet ground state. Consequently, new non-perturbative methods had to be developed for the description of the physics below the Kondo scale T_K . The solution to the Kondo problem was achieved by K. G. Wilson as he devised the *numerical renormalization group (NRG)* [3] method in the 1970s.

The NRG will be the central topic of this thesis and it will be employed in the solution of complex quantum impurity systems. The thesis is organized as follows:

In chapter 1 we will introduce the *Kondo effect* as one of the archetype problems in correlated many-body physics. Beginning with the long time unexplained resistance minimum in metals with magnetic impurities, we describe how J. Kondo explained this behavior by means of his perturbative calculations on a model of the exchange scattering between the electron spin and the impurity spin. The then arising *Kondo problem* was that the calculations break down at low temperatures due to logarithmic

mically diverging terms. We present the first steps towards a solution of the Kondo problem via the single impurity Anderson model (SIAM) and Anderson's poor man's scaling approach. Then we briefly sketch how the Kondo problem was firstly solved by a non-perturbative approach, Wilson's numerical renormalization group (NRG), and how Wilson's results were confirmed later by an analytical method, the Bethe ansatz (BA). At the end of chapter 1, we motivate why the Kondo effect is still an active field of modern condensed matter physics.

Chapter 2 contains a short insight into methods which solve quantum impurity problems either analytically or numerically. We shortly describe how the Bethe ansatz technique gives reliable results on exact wave functions, spectra and thermodynamics of the Kondo problem for the entire range of temperatures and magnetic field. As the BA cannot access dynamical properties, we subsequently sketch a prominent method for one-dimensional quantum systems, the density matrix renormalization group (DMRG), which also yields results on dynamical correlation functions. The rest of chapter 2 is devoted to an approximate, but systematic technique, which can describe the high and low temperature behavior of quantum impurity models – the so-called Non-Crossing Approximation (NCA). The NCA provides a very flexible solution method for more complex impurity models as e. g. multi-orbital Anderson models, which becomes useful in our work on the electronic transport through Kondo atoms in chapter 5.

The main part of this thesis is contained in chapter 3, where we describe in detail the numerical renormalization group (NRG) technique. Originally developed by Wilson for the solution of the Kondo problem, this non-perturbative method has been used to tackle even more complex quantum impurity problems. The first part of chapter 3 presents how the NRG procedure works for the SIAM. The following chapter describes how the NRG, which was developed for this thesis, is applied to quantum impurity models. We present the analysis of fixed points, the calculation of thermodynamics and the calculation of dynamic properties as the local impurity spectral function. Section 3.3 shows how the NRG was extended towards more complicated models, including the application of the NRG in non-equilibrium problems. A modern approach of describing strongly correlated materials is the dynamical mean-field theory (DMFT). The last section of chapter 3 contains an introduction of how the NRG is used within DMFT calculations. Thereafter we describe how we plan to apply our NRG program within our proposed microscopic model for europium oxide.

In chapter 4, we give our results on a multi-channel impurity model, the two-channel Kondo (2CK) model, as obtained via an extended NRG. We motivate why the study of the 2CK model is relevant in the description of strongly correlated materials and how only the 2CK effect can explain experimental results on quantum point contacts. We describe how the usual NRG program had to be adapted and compare our results with existing 2CK NRG solutions. We then show our new results on the distribution of the 2CK Kondo temperature versus the Kondo coupling J .

Chapter 5 is devoted to multiorbital Anderson impurities and how we use this extended impurity model to explain scanning tunneling microscopy (STM) experiments.

First we overview the experimental and theoretical background of the Kondo effect, which plays a crucial role in STM experiments of transition metal atoms on metal surfaces. We then show how we improved the theoretical explanation of the STM lineshapes occurring in experiments with titanium atoms on gold and silver surfaces. We therefore combined density functional theory calculations with an extended NCA to recover the experimental spectra. It is shown in section 5.4 that with our method we can gain insight into the electronic transport and the geometry of transition metal Kondo atoms.

We offer a conclusion in English and in German in chapters 6 and 7.

The appendix contains technical details used for the calculations in the conventional, one-channel NRG (appendix A) and in the 2CK NRG (appendix B). Finally, the thesis contains miscellaneous information as a list of abbreviations, a list of publications, the bibliography, a curriculum vitae and acknowledgements.

Chapter 1

The Kondo effect

The presence of magnetic impurities in metals changes the physical properties of a system drastically, leading to non-trivial many-body physics referred to as *Kondo physics* [1]. This chapter explains the *Kondo effect*, which has been a topic of central interest for condensed matter physics since many years now. Many experimental and theoretical progress has been made since the discovery of the *Kondo problem* in the 1960s. It is still a very active field of research and Kondo physics also makes a big contribution to modern applications as e. g. to nanotechnology.

1.1 The Kondo problem

The first manifestation of the effect of magnetic impurities in metals has been known since the early 1930s, where de Haas *et al.* [4] observed a shallow minimum in the resistance of some metals (see Figure 1.1).

Later it has been recognized that this minimum is related to small contaminations of the supposed clean metal with (magnetic) 3d transition metal impurities, such as iron.

Significant theoretical progress was the explanation of this effect by J. Kondo in 1964 [2]. Kondo's calculations were based on a model of the exchange scattering between the electron spin and the impurity spin, known as the s-d model:

$$\mathcal{H}_{s-d} = \mathcal{H}_c + \sum_{\vec{k}\vec{k}'} J_{\vec{k}\vec{k}'} c_{\vec{k}\sigma}^\dagger \vec{\sigma}_{\sigma\sigma'} c_{\vec{k}'\sigma'} \vec{S}_I, \quad (1.1)$$

where $\mathcal{H}_c = \sum_{\vec{k}\sigma} \varepsilon_{\vec{k}\sigma} c_{\vec{k}\sigma}^\dagger c_{\vec{k}\sigma}$ is the conduction band (CB) Hamiltonian and the second term represents a Heisenberg exchange interaction between the conduction electrons and the impurity spin S_I ($\vec{\sigma}_{\sigma\sigma'}$ is a vector of the Pauli matrices). An eventual potential scattering term can be absorbed in \mathcal{H}_c .

To describe the scattering events, Kondo computed the matrix elements of the \mathcal{T} matrix, $\langle \vec{k}'\sigma' | \mathcal{T} | \vec{k}\sigma \rangle$, in which a conduction electron is scattered from a state $|\vec{k}\sigma\rangle$

to a state $|\vec{k}'\sigma'\rangle$. To calculate the resistivity to third order in J (to be considered \vec{k} -independent from now on) one needs the \mathcal{T} matrix to second order in J . Among many terms, the most important terms are the ones in which a spin flip event between conduction electrons and local impurity spin occurs (see Figure 1.3).

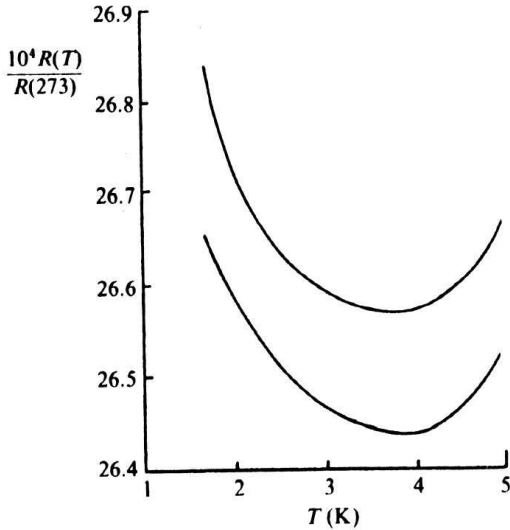


Figure 1.1: The minimum in the electrical resistivity of gold [4].

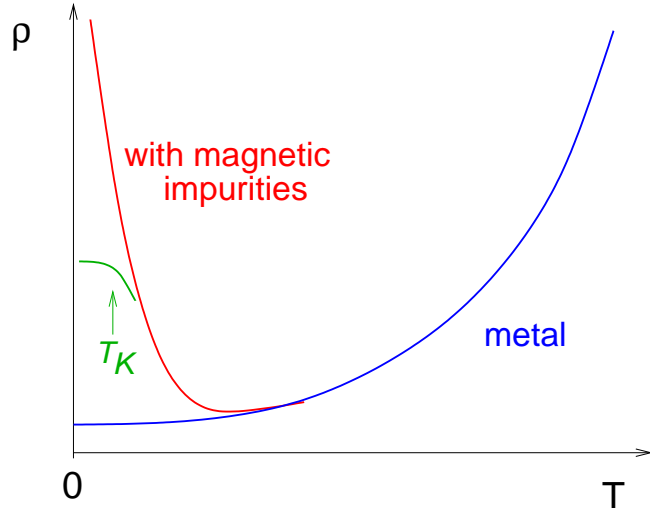


Figure 1.2: Temperature dependence of the resistivity of pure metals (*blue*). As a metal contains a small fraction of magnetic impurities, the resistance increases due to the Kondo effect (*red*). If the impurity moment is screened, the resistance saturates below the Kondo scale T_K (*green*).

Kondo's final result was that the interaction between local impurity spin S_I and the conduction electrons of the host metal leads to singular scattering near the Fermi level and a logarithmic ($\ln T$) contribution to the resistivity. The observed resistance minimum could be explained when the $\ln T$ term (which increases at low T) is included with the phonon contribution (which vanishes for $T \rightarrow 0$ as T^5).

The problem (called the *Kondo problem*) with this theory is that Kondo's perturbational calculations could not be valid at low temperatures, as the logarithmic terms diverge as $T \rightarrow 0$. When the spins couple anti-ferromagnetically ($J > 0$), all perturbation expansions summing leading order logarithmically divergent terms break down at a finite temperature T_K , known as the *Kondo temperature*. In the late 60s Anderson introduced the theoretical framework for understanding the results of magnetic impurity systems also in the region $T < T_K$. The key idea was that of scaling (see section

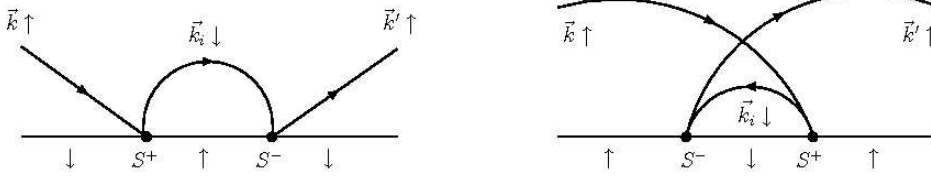


Figure 1.3: Feynman diagrams of a second order spin flip contribution to the matrix element $\langle \vec{k}' \uparrow | \mathcal{T} | \vec{k} \uparrow \rangle$. The lower line represents the local impurity spin, whereas the upper, arrowed lines are the CB electrons.

1.3): If higher order excitations were traced out to give an effective model valid on a lower energy scale, the effective coupling between the impurity and the conduction electrons increased. For $T \ll T_K$ this scaling behavior implies a ground state with an infinitely strong coupling in which impurity and surrounding conduction electrons are bound into a singlet state. The low temperature behavior would then be similar to that of a non-magnetic impurity – the impurity spin having been compensated – see Figure 1.2.

A model which incorporates the key ingredients for the solution of the Kondo problem, (1) the formation of local moments, (2) the scattering off conduction electrons and (3) the screening of local moments below a temperature scale T_K is the *single impurity Anderson model (SIAM)*, presented in the following paragraph.

1.2 The Anderson model

The resistance minimum was observed to depend on the impurity concentration, indicating that it is an impurity phenomenon. However, the depth of the minimum, measured relative to the value at $T = 0K$, was found to be roughly proportional to the impurity concentration c_{imp} , and its ratio with the resistivity at $T = 0K$ was found independent of c_{imp} . Therefore the minimum is essentially a *single impurity* effect, and inter-impurity effects could be excluded at first sight.

P. W. Anderson [5] introduced a model to describe a local moment in a metal, where he included a local Coulomb interaction U between the electrons on a single impurity site. This model is called single impurity Anderson model (SIAM) and will often be used in this thesis. It reads

$$\mathcal{H}_{SIAM} = \sum_{\sigma} \varepsilon_d d_{\sigma}^{\dagger} d_{\sigma} + U d_{\uparrow}^{\dagger} d_{\uparrow} d_{\downarrow}^{\dagger} d_{\downarrow} + \sum_{\vec{k}\sigma} \varepsilon_{\vec{k}\sigma} c_{\vec{k}\sigma}^{\dagger} c_{\vec{k}\sigma} + V \sum_{\vec{k}\sigma} \left(d_{\sigma}^{\dagger} c_{\vec{k}\sigma} + c_{\vec{k}\sigma}^{\dagger} d_{\sigma} \right) \quad (1.2)$$

This model describes a single impurity level (where d_{σ}^{\dagger} creates a state with spin σ and energy ε_d), subject to a Coulomb repulsion U if doubly occupied, in a conduction band

(CB) with dispersion $\varepsilon_{\vec{k}\sigma}$ ¹. The impurity and the CB are coupled via a hybridization V .

In order to get some insight into this model, one might consider the 'atomic limit' $V = 0$, where impurity and conduction band are decoupled and the model can be trivially solved. There are three total energy configurations for the d-states: (1) zero occupation with a total energy $E_0 = 0$; (2) single occupation by a spin σ with a total energy $E_{1,\sigma} = \varepsilon_d$ where $\sigma = \uparrow, \downarrow$; (3) double occupation with two spins (one spin \uparrow and one spin \downarrow) on the impurity giving a total energy of $E_2 = 2\varepsilon_d + U$. In this simplified model the condition for a 'local moment' (a magnetic moment at the impurity site) is that the singly occupied configuration ($\hat{n} = 1$) lies lowest, which requires $\varepsilon_d < \varepsilon_F$ and $\varepsilon_d + U > \varepsilon_F$. The Fermi energy ε_F is usually taken to be zero in this models if not stated otherwise.

The SIAM is a model which is more general than the s-d model Kondo used for his explanation of the resistance minimum. If the hybridization V is sufficiently small, the two models are equivalent to each other.

The SIAM attracted new attention when it was realized that it is the appropriate effective model in the context of dynamical mean-field theory (DMFT) (see also chapter 3.4).

1.2.1 The Schrieffer-Wolff transformation

The connection between the SIAM and the s-d model can be derived within lowest order perturbation theory, if one takes $\hat{n} = 1$ as the ground state and considers virtual excitations to the unoccupied and doubly occupied states. Even though $\varepsilon_d < \varepsilon_F$ and $\varepsilon_d + U > \varepsilon_F$ and small V is fulfilled, or more precisely:

$$\varepsilon_d \ll -|\Delta| \ll \varepsilon_F \ll |\Delta| \ll \varepsilon_d + U \quad \text{with } \Delta = \pi V^2 \rho(\varepsilon_F) \quad (1.3)$$

there is a small, finite probability to have a d-occupation of 0 or 2, respectively. During the virtual excitation, the impurity spin might (1) flip its spin from up to down; (2) flip from down to up; (3) remain unchanged. As the total spin is conserved, the CB electron spin has to flip oppositely to the impurity spin (or remain unchanged in case (3)). Therefore, the Hamiltonian in the local moment regime should contain a term of the form $\vec{S}_c \cdot \vec{S}_I = \frac{1}{2}(S_c^+ S_I^- + S_c^- S_I^+) + S_c^z S_I^z$. \vec{S}_c represents the conduction electron spin operator. An excitation to the unoccupied (doubly occupied) level lowers the total energy by ΔE_0 (ΔE_2)

$$\Delta E_0 = \frac{V^2(1 - f(\varepsilon_k))}{\varepsilon_k - \varepsilon_d}, \quad (1.4)$$

$$\Delta E_2 = \frac{V^2 f(\varepsilon_k)}{U + \varepsilon_d - \varepsilon_k}, \quad (1.5)$$

¹The density of states $\rho_\sigma(\varepsilon)$ of the conduction band relates to the energy dispersion as follows: $\rho_\sigma(\varepsilon) = \sum_{\vec{k}} \delta(\varepsilon - \varepsilon_{\vec{k}\sigma})$.

where $f(\varepsilon_k) = (1 + e^{\beta(\varepsilon_k - \varepsilon_F)})^{-1}$ is the Fermi function.

Because of Eq. 1.3 one can approximate the denominators by their smallest possible values ($\varepsilon_k \approx \varepsilon_F$) and thus the virtual processes lower the energy by

$$J = \frac{V^2}{\varepsilon_F - \varepsilon_d} + \frac{V^2}{U + \varepsilon_d - \varepsilon_F} \quad (1.6)$$

Summing up all possible virtual excitations to lowest order perturbation theory yields the following effective Hamiltonian for the local moment regime:

$$H_K = \sum_{\vec{k}\sigma} \varepsilon_{\vec{k}\sigma} c_{\vec{k}\sigma}^\dagger c_{\vec{k}\sigma} + 2J\vec{S}_c \cdot \vec{S}_I \quad (1.7)$$

which is also called the *Kondo model*.

The projection of the SIAM onto the local moment subspace was first accomplished by Schrieffer and Wolff [6], using a canonical transformation.

1.3 Poor man's scaling

The logarithmic terms which lead to the breakdown of perturbation theory depend on the conduction electron bandwidth via $\ln D$. P. W. Anderson [7] found a method in which he progressively reduced D and perturbatively calculated the renormalized interactions due to the elimination of virtual excitations to the band edges. Thus higher energy excitations are taken into account and the $\ln D$ terms enter only in the parameters of the effective Hamiltonian for the calculation of the low lying levels. This so-called ‘‘poor man’s scaling’’ method is illustrated in Figure 1.4. By integrating out the high energy states at the band edges, an effective model on a lower energy scale is obtained (the bandwidth is reduced from D to $\tilde{D} = D - \delta D$).

The physical parameters of the system (in case of the Kondo model: the coupling $J \rightarrow \tilde{J}$) have to be adapted such that the scattering between CB electrons and impurity is invariant. This procedure leads to a cutoff dependent ‘flow’ of $\tilde{J}(\tilde{D})$ so that the derived Hamiltonian describes the low energy behavior of the system correctly. For the Kondo model, the poor man’s scaling approach leads to the scaling equation

$$\frac{dJ}{d \ln D} = -2\rho_0 J^2, \quad (1.8)$$

where a flat conduction band ($\rho_0 = \text{const.}$) was assumed. Integrating Eq. 1.8 from D to \tilde{D} gives

$$\tilde{J}(\tilde{D}) = \frac{J}{1 + 2\rho_0 J \ln(\tilde{D}/D)} \quad (1.9)$$

which tells us that in the weak coupling regime ($\rho_0 J \ll 1$) the effective coupling \tilde{J} continuously grows on reducing the bandwidth. If one continues until the desired

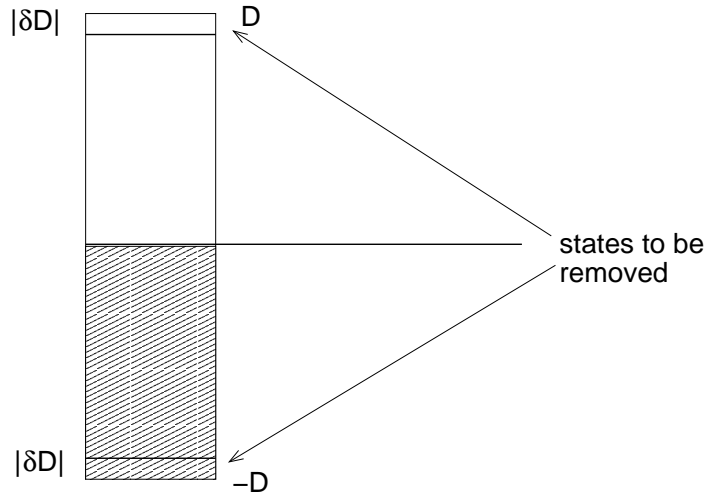


Figure 1.4: Poor man's scaling: The particle and hole states which are removed from the conduction band on reducing the bandwidth by $|\delta D|$.

temperature scale $T \sim \tilde{D}$, one realizes that \tilde{J} diverges at a temperature

$$De^{-1/(2\rho_0 J)} = \tilde{D}e^{-1/(2\rho_0 \tilde{J})} \sim k_B T_K, \quad (1.10)$$

which is the *Kondo temperature* T_K .

The scaling approach shows that one can use perturbative approaches only down to the temperature scale T_K and that for $T \ll T_K$ the conduction electrons are infinitely strong bound to the impurity spin ($J \rightarrow \infty$), forming a spin singlet ground state.

1.4 Solution of the Kondo problem

A non-perturbative way of deriving a model for the calculation of the low temperature behavior was devised by Wilson [3] with his *numerical renormalization group (NRG)*, which is the central topic of this thesis and will be described in chapter 3 in great detail.

For describing the low temperature physics of the Kondo model one might expect that high energy states can be disregarded and only states of energy $|\omega| \leq T$ contribute. One clearly sees that this assumption is wrong when we remember the second order diagrams in the perturbation expansion (see Figure 1.3): The intermediate states in the scattering can carry *arbitrary* momentum \vec{k}_i and thus *all* energy scales have to be taken into account in the solution of the Kondo problem. To incorporate all energies of the problem, the idea of the renormalization group (RG) was introduced. Wilson used the RG approach [8] together with Anderson's scaling ideas to construct the NRG as the first non-perturbative solution of the Kondo model, for which he was awarded the Nobel prize in 1982.

The NRG verified that the local magnetic moment vanishes for $T \rightarrow 0$ and thus the resistivity no longer diverges. Krishna-murthy *et al.* [9, 10] applied the NRG to the SIAM to calculate various static properties for the symmetric and the asymmetric case. A confirmation of Wilson's NRG result was given by the first exact analytical solution of the Kondo model by Andrei [11] and Wiegmann [12] in 1980 (see section 2.1.1).

Although the Kondo problem has been solved in the 1970s, Kondo physics is still a widely studied field of condensed matter research. Due to new experimental techniques from the rapidly developing field of nanotechnology the Kondo effect has gained renewed interest.

1.5 Revival of the Kondo effect

Interest in the Kondo effect has persisted since it provides clues to understand the electronic properties of a wide variety of materials with strong interactions, for instance in heavy-fermion materials and high- T_c superconductors [13]. In modern chip technology, small semiconductor devices are used to systematically investigate fundamental quantum mechanical problems. One such device is the quantum dot (QD) – small electron droplets which are confined in a small semiconductor box. With a QD it is possible to realize one of the simplest strongly correlated models, the Kondo model, experimentally. The first experimental observation of the Kondo effect in QDs was in 1998 by Goldhaber-Gordon *et al.* [14]. They showed that Kondo physics occurs in a transistor-type semiconductor device (see Figure 1.5), as already predicted in 1998 [15, 16]. Another group measured the conduction of this so-called “single-electron transistor” (as electrons are transported through the dot one at a time) as a function of gate voltage, which changes the number of electrons within the QD [17]. For an odd number of electrons on the dot, the Kondo effect produces a many-body ground state at the Fermi level, providing a transport channel for the electrons tunneling from one lead to the other. Moreover, for low temperatures the conductance is increased and approaches the ‘unitary limit’ of $2e^2/h$, where e is the electron charge (see Figure 1.6). The Kondo effect can also be seen in scanning tunneling microscopy (STM) experiments. STM is a central tool in nanotechnology which aims to manipulate and control matter at the atomic scale. If one uses STM to investigate magnetic impurities on the surface of metals, the Kondo effect plays a key role in the physical properties of the system. In 1998, two groups independently found signatures of the Kondo resonance in the STM conductance spectra [19, 20]. It is also possible to directly “photograph” the metal surface with STM. A very illustrative picture of the Kondo effect is shown in Figure 1.7. Cobalt atoms are placed on a copper surface with STM. By placing a single cobalt atom at the focal point of an ellipse built from other cobalt atoms, the density of states reveals the Kondo resonance (left peak). Due to elliptical confinement a second, smaller Kondo resonance can be seen at the other focal point (right), even

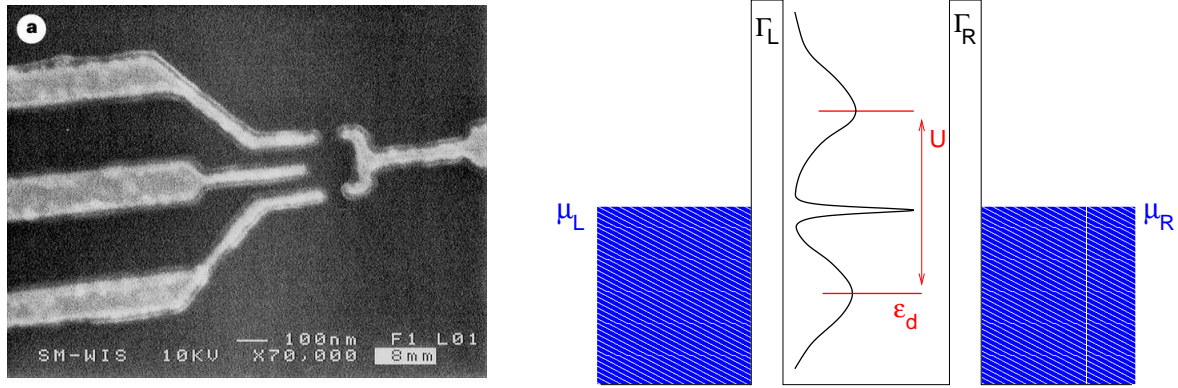


Figure 1.5: *Left:* Image of the device used by [14, 18] to measure the Kondo effect. Several gates are used to accurately control the electronic transport from the top electron reservoir through the confined region to the lower reservoir (i. e. from a source to a drain region). *Right:* Schematic energy diagram of the single-electron transistor, showing an electron droplet separated by tunnel barriers from conducting leads. For an odd number of electrons on the dot, the local density of states exhibits a sharp Kondo resonance at the Fermi level.

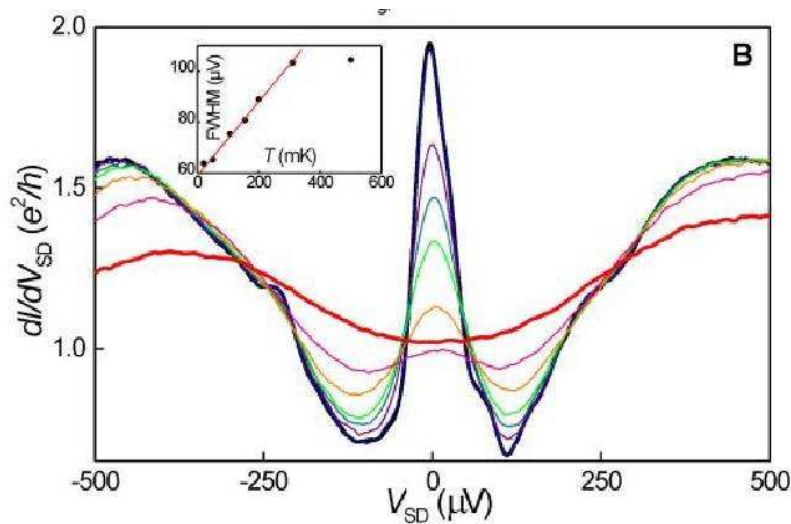


Figure 1.6: The differential conductance dI/dV vs. source-drain voltage V_{SD} in a QD for different temperatures as measured by [17]. On lowering the temperature, the Kondo effect increases the conductance at the Fermi level.

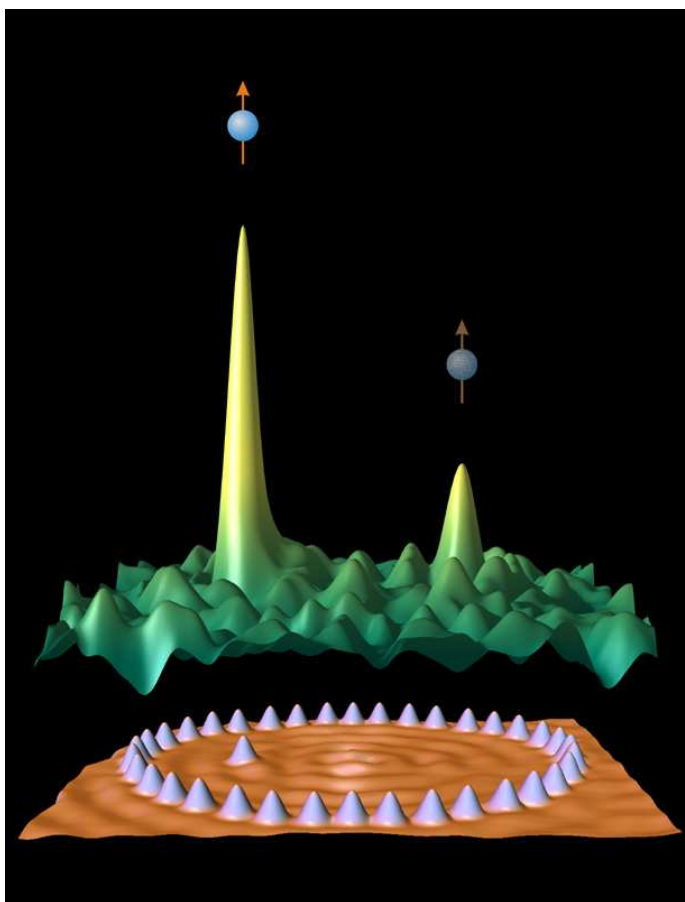


Figure 1.7: "Quantum mirage": STM image of cobalt atoms on a copper surface [21, 22]. By placing a single cobalt atom at the focal point of an ellipse built from other cobalt atoms, the density of states reveals the Kondo resonance (left peak). Due to elliptical confinement a second, smaller Kondo resonance can be seen at the other focal point (right), even though there is no cobalt atom present.

though there is no cobalt atom present.

The Kondo effect in STM experiments will become important in our analysis of STM lineshapes of transition metal Kondo atoms on metal surfaces (see chapter 5).

Chapter 2

Solution methods for quantum impurity systems

After Kondo's successful explanation of the resistance minimum in metals with magnetic impurities [2], it was recognized that the electronic correlations play a crucial role in magnetic impurity systems. Since 40 years, much effort has been expended on the theoretical study of the Kondo problem as an archetype of a correlated many-body system.

In this chapter we present some of the numerical techniques, which help to gain a better understanding of the Kondo problem. The numerical renormalization group (NRG) developed by Wilson [3] in 1975 was the first method which confirmed that the Kondo model and the SIAM have a singlet ground state and that the low energy excitation spectrum can be described well by Fermi liquid (FL) theory. As the NRG is the central topic of this thesis, it will be covered in the following chapter 3 in great detail. In this chapter, we briefly introduce other methods which deal with the solution of the Kondo problem, like the analytical solution, the Bethe ansatz (BA), or the density matrix renormalization group (DMRG).

Besides these "exact" solution methods it is desirable to develop approximate, but systematic techniques which do not rely on special symmetry conditions, a relatively simple model structure (like NRG), or on integrability conditions (like the BA), while still describing the high and low energy behavior of the model as well as the crossover region around T_K correctly. It turned out that advanced perturbation theory methods and especially conserving approximation techniques like the Non-Crossing Approximation (NCA), described below in detail (section 2.2), provide such very flexible solution methods [23]. They are not restricted to simple structures of the conduction electron density of states and thus may be employed as impurity solvers for self-consistent models of the dynamical mean-field theory (DMFT). Furthermore they are applicable to more complex impurity models like multi-orbital Anderson models, which became useful in the context of our work on electronic transport through Kondo atoms (see chapter 5).

For a comprehensive review on the theories in the context of the Kondo problem, also on methods we do not mention in this thesis, we refer to the book of Hewson [1].

2.1 Other methods for the Kondo problem

2.1.1 Bethe Ansatz

The Bethe ansatz (BA) [24], originally developed for the solution of the one-dimensional Heisenberg model, was used in 1980 independently by Andrei *et al.* [25, 11] and Tsvetick and Wiegmann [12, 26] to give the first analytical solution to the one-channel Kondo model, fully confirming Wilson's NRG results. Later, also the multi-channel model was solved by the two different groups [27, 28].

The solution via the BA modifies the original Kondo model Hamiltonian. It utilizes a linear dispersion ($\varepsilon(\vec{k}) = k$) for the conduction electrons near the Fermi energy and thus, after a Fourier transform, the term $\sum_k k c_{k\sigma}^\dagger c_{k\sigma}$ gets replaced by $\int dx c_\sigma^\dagger(x) \frac{\partial}{\partial x} c_\sigma(x)$. The resulting Hamiltonian corresponds to a system of conduction electrons in one dimension, coupling to the impurity only at $x = 0$. Consequently it is possible to build up the solution of the problem at $x \neq 0$ out of single-particle states and incorporate the impurity degrees of freedom only at $x = 0$.

To obtain results on the thermodynamics, a functional of the free energy is set up and its minimization leads to an infinite set of non-linear integral equations, which have to be solved numerically. With the Bethe ansatz solution, earlier results could be confirmed, like the correct 'Wilson ratio' $R = 2$ or a formula for the Kondo temperature T_K . Also the universality hypothesis could be confirmed, i. e. all thermodynamic properties at low temperatures depend only on the ratio T/T_K . The comparison between BA and NRG results for the effective magnetic moment $T\chi_{imp}(T)$ shows a perfect agreement of the two methods (see Fig. 2.1). While the BA yields reliable results for exact wave functions, spectra and thermodynamics for the entire range of temperature and magnetic field, it cannot access dynamic properties like correlation functions. It is an unsolved problem to properly express the operators which couple to external probes in terms of the exact many-body states which are provided by the BA. Therefore it is desirable to develop methods which can also access dynamical properties. An example besides the NRG is another RG method, the density matrix renormalization group (DMRG).

2.1.2 Density matrix renormalization group (DMRG)

Numerical approaches aim at the numerical diagonalization of a given Hamiltonian. As the matrix to be diagonalized grows exponentially with the system size, one has to think about a proper truncation scheme which restricts the calculations onto a numerically feasible subspace. It is the essence of every renormalization group (RG)

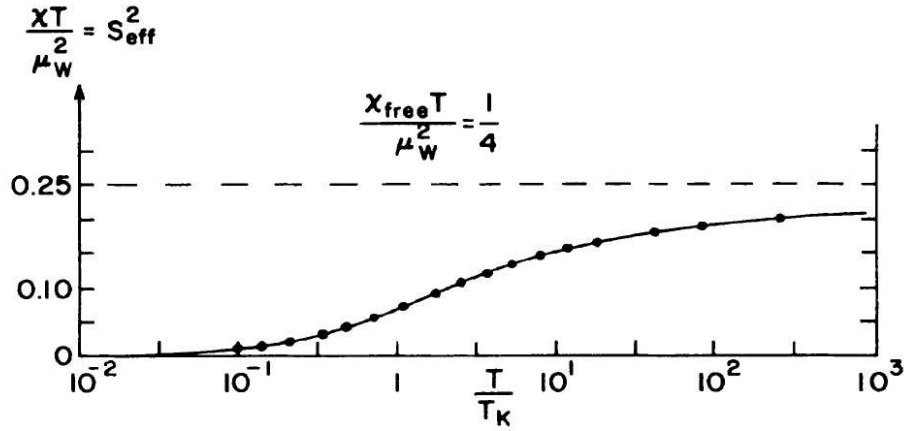


Figure 2.1: Bethe ansatz solution for the effective spin χT . The dots represent the NRG results of [9]. Figure taken from [11].

method, to bring in an energy scale in which the theory can be formulated. The NRG is a renormalization procedure in momentum or energy space, thus one separates the whole problem into different energy scales. However, this truncation scheme (keeping only the energetically lowest lying states) does not work for models where the same energy scales are added at each step of the RG procedure. This is the case for lattice models, e. g. for the one-dimensional Hubbard model. The solution to the problem of finding a truncation scheme in this case is given in the context of the density matrix renormalization group (DMRG).

The DMRG is a numerical variational technique invented by White [29, 30] devised to obtain the low energy physics of quantum many-body systems with high accuracy. One starts with a numerically manageable system of only a few sites (*system block*) and iteratively enlarges the system by successively adding small clusters of one or more sites (*environment block*). The ground state of the complete system (*superblock* = *system block* + *environment block*) is calculated and the reduced density matrix of the *system block* is evaluated, through tracing out the *environment block*. The truncation now happens according to the largest entries in the diagonalized, reduced density matrix and all the operators have to be transformed accordingly. The procedure described above is called *infinite system algorithm*, as one proceeds until the desired chain length is reached, which in principle can be an infinitely long system. Other DMRG techniques like the *finite size algorithm* are well described in [31].

The DMRG is one of the most common numerical techniques for one-dimensional quantum systems. Besides exact determination of ground state energies, dynamical correlation functions can be calculated accurately.

2.2 The Non-Crossing Approximation (NCA)

2.2.1 Renormalized perturbation theory for the SIAM

Again, the starting point for a system dealing with Kondo physics is the single-impurity Anderson model, as already described by Eq. (1.2):

$$\mathcal{H}_{SIAM} = \sum_{\sigma} \varepsilon_d d_{\sigma}^{\dagger} d_{\sigma} + U d_{\uparrow}^{\dagger} d_{\uparrow} d_{\downarrow}^{\dagger} d_{\downarrow} + \sum_{\vec{k}\sigma} \varepsilon_{\vec{k}\sigma} c_{\vec{k}\sigma}^{\dagger} c_{\vec{k}\sigma} + V \sum_{\vec{k}\sigma} \left(d_{\sigma}^{\dagger} c_{\vec{k}\sigma} + c_{\vec{k}\sigma}^{\dagger} d_{\sigma} \right)$$

Provided a large Coulomb interaction U and the impurity level ε_d sufficiently far below E_F , the impurity will on average be occupied by one electron. The system is then said to be in the *Kondo regime*, when a local spin $S = 1/2$ resides at the impurity.

Due to the high value of the local Coulomb interaction a perturbation expansion in U becomes senseless, but for small hybridization V compared to the impurity level $|\varepsilon_d|$, a perturbation theory in V seems reasonable, while absorbing the Coulomb term in the unperturbed Hamiltonian. There are two complications for the perturbational treatment: (1) the impurity is an interacting system for which powerful methods like Wick's theorem, Feynman diagrams and renormalization of propagators and vertices are not immediately applicable; (2) logarithmic diverging terms (like the ones in the Kondo exchange coupling J) arise in the perturbation theory in V .

Problem (1) will be solved by the pseudoparticle representation which is presented in the next paragraph. The solution to problem (2) by so-called ‘‘conserving approximations’’ is the topic of the subsequent section.

2.2.2 Pseudoparticle representation and projection onto the physical Hilbert space

The dynamics of an electron on a local level will depend crucially on whether that level is singly or doubly occupied. Therefore it is useful to divide up the Hilbert space into sectors which are labeled by the occupation number of the quantum impurity. For each Fock state one defines a creation operator, which, when operating on the vacuum state $|vac\rangle$ creates the corresponding state: For a two-fold (spin-)degenerate impurity one defines two bosonic operators a and b and two fermionic operators f_{σ} ($\sigma = \uparrow, \downarrow$), which create the doubly occupied and empty states $|2\rangle = a^{\dagger}|vac\rangle$, $|0\rangle = b^{\dagger}|vac\rangle$ and the singly occupied states $|\sigma\rangle = f_{\sigma}^{\dagger}|vac\rangle$, respectively. In terms of the pseudoparticle operators, the creation of an electron of spin σ in an empty level is described as

$$d_{\sigma}^{\dagger} = f_{\sigma}^{\dagger} b + \sigma a^{\dagger} f_{-\sigma} \quad (2.1)$$

The Hamiltonian then takes the form

$$\begin{aligned} \mathcal{H} = & \varepsilon_d \left(\sum_{\sigma} f_{\sigma}^{\dagger} f_{\sigma} + 2a^{\dagger} a \right) + U a^{\dagger} a + \sum_{\vec{k}\sigma} \varepsilon_{\vec{k}\sigma} c_{\vec{k}\sigma}^{\dagger} c_{\vec{k}\sigma} \\ & + V \sum_{\vec{k}\sigma} \left(c_{\vec{k}\sigma}^{\dagger} b^{\dagger} f_{\sigma} + \sigma c_{\vec{k}\sigma}^{\dagger} f_{-\sigma}^{\dagger} a + h.c. \right) \end{aligned} \quad (2.2)$$

The Hilbert space is now vastly enlarged into unphysical regions. As the impurity must be occupied by exactly one pseudoparticle at any time (corresponding to a definite state), the following constraint on the pseudoparticle number Q is to be met:

$$Q = \sum_{\sigma} f_{\sigma}^{\dagger} f_{\sigma} + b^{\dagger} b + a^{\dagger} a = 1 \quad (2.3)$$

This constraint can be thought of as charge quantization with an integer Q as conserved, quantized charge. As in quantum field theory, charge conservation is related to the existence of a local gauge symmetry, which in our case is a local $U(1)$ symmetry of the model described by Hamiltonian Eq. (2.2): The system is invariant under simultaneous gauge transformations $f_{\sigma} \rightarrow f_{\sigma} e^{i\phi(\tau)}$, $b \rightarrow b e^{i\phi(\tau)}$, $a \rightarrow a e^{i\phi(\tau)}$, with $\phi(\tau)$ an arbitrary, time-dependent phase. The gauge symmetry now guarantees the conservation of Q at all times.

In order to project onto the physically relevant subspace $Q = 1$, one starts with the grand-canonical ensemble with respect to Q and the associated chemical potential $-\lambda$. The projection is achieved by taking the limit $\lambda \rightarrow \infty$ of any grand-canonical expectation value of a physical operator \hat{A} :

$$\langle \hat{A} \rangle = \lim_{\lambda \rightarrow \infty} \frac{\langle \hat{A} \rangle_{GC}}{\langle \hat{Q} \rangle_{GC}}, \quad (2.4)$$

The extra factor Q in the denominator has been introduced to project out the $Q = 0$ subspace. Since $\langle \dots \rangle$ denotes the average of the grand canonical ensemble with respect to Q , this procedure allows one to apply the complete machinery of quantum field theory, especially one may use Wick's theorem.

Physically observable quantities are given by two pseudoparticle correlation functions (or higher), which in principle requires the calculation of both self-energy and vertex corrections. Details on the evaluation of the pseudoparticle diagrams can be found in [32].

Explicitly, the imaginary time single-particle Green's functions

$$G_{f\sigma}(\tau_1 - \tau_2) = - \left\langle \hat{T} [f_{\sigma}(\tau_1) f_{\sigma}^{\dagger}(\tau_2)] \right\rangle_{GC} \quad (2.5)$$

where \hat{T} is the time-ordering operator, and analogous expressions for the bosons a, b may be expressed in terms of the selfenergies $\Sigma_{f,b,c}(i\omega)$ as

$$\begin{aligned} G_{f\sigma}(i\omega) &= [i\omega - \lambda - \varepsilon_d - \Sigma_{f\sigma}(i\omega)]^{-1} \\ G_b(i\omega) &= [i\omega - \lambda - \Sigma_b(i\omega)]^{-1} \\ G_a(i\omega) &= [i\omega - \lambda - 2\varepsilon_d - U - \Sigma_a(i\omega)]^{-1} \end{aligned} \quad (2.6)$$

2.2.3 Conserving approximations: NCA

To tackle the problem of logarithmically diverging terms in the perturbation theory in V , one has to pick the essential terms in pseudoparticle representation. In order to be able to perform the projection onto the physical subspace, one requires the conservation of the local charge Q . Gauge invariant approximations conserving Q may be derived from a Luttinger-Ward generating functional Φ [33, 34]. The self-energies Σ_x , $x = a, b, f, c$ are obtained by taking the functional derivatives

$$\Sigma_x = \frac{\delta\Phi}{\delta G_x} \quad (2.7)$$

and are thus functionals of the dressed G_x . For any choice of Φ a closed set of integral equations for the G_x 's is obtained, which have to be solved numerically.

The Non-Crossing Approximation (NCA) is the lowest (second order in V) approximation for Φ . Its name originates from the corresponding Feynman diagrams, which do not have any crossing lines (see Fig. 2.2).

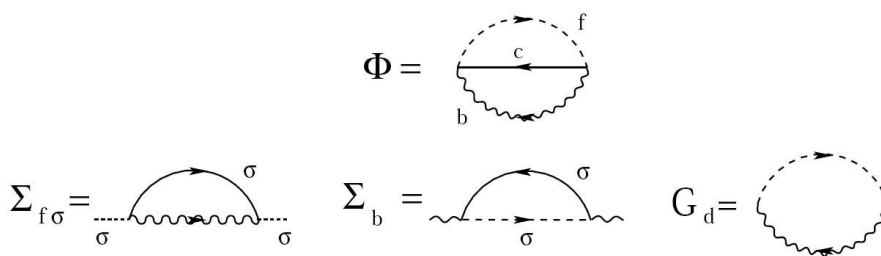


Figure 2.2: Diagrammatic representation of the generating functional Φ of the NCA. Also shown are the pseudoparticle self-energies and the local d -electron Green's function derived from Φ . Dashed, wavy and solid lines represent fermion, boson and conduction electron lines, respectively. Figure taken from [35].

A comprehensive review, also on the original works and the development of the NCA can be found in [36]. Most of the NCA works are concerned with infinite on-site repulsion $U \rightarrow \infty$, where double occupancy of the impurity is strictly excluded. In

this case the self-consistent NCA equations together with Eq. 2.6 read (compare Fig. 2.2)

$$\Sigma_{f\sigma}^{NCA}(\omega) = \Gamma \int \frac{d\varepsilon}{\pi} f(\varepsilon) A_{c\sigma}^0(-\varepsilon) G_b(\omega + \varepsilon) \quad (2.8)$$

$$\Sigma_b^{NCA}(\omega) = \Gamma \sum_{\Sigma} \int \frac{d\varepsilon}{\pi} f(\varepsilon) A_{c\sigma}^0(\varepsilon) G_{f\sigma}(\omega + \varepsilon) \quad (2.9)$$

$$G_{d\sigma}^{NCA} = \int d\varepsilon e^{-\beta\varepsilon} [G_{f\sigma}(\omega + \varepsilon) A_b(\varepsilon) - A_{f\sigma}(\varepsilon) G_b(\varepsilon - \omega)] \quad (2.10)$$

where $\Gamma = \pi N_0 |V|^2$ with $N_0 = 1/2D$ the conduction electron DoS at E_F , the frequency ω is $\omega \pm i0$ for the retarded/advanced functions and $A_{c\sigma}^0 = (1/\pi) \text{Im} G_{c\sigma}^0/N_0$ is the local conduction electron DoS per spin. $f(\varepsilon) = 1/(\exp(\beta\varepsilon) + 1)$ is the Fermi distribution function.

The NCA nicely works for the calculation of dynamical properties in a wide parameter range. It reliably describes the Kondo scale T_K and the position, the spectral weight, and the lifetime broadening of the peaks in the local spectral density down to $T \approx 0.1T_K$ [36]. However it fails for very low temperatures $T \ll T_K$, where it yields the wrong infrared exponents, in contradiction to the expected FL behavior. The inclusion of a local magnetic field produces a spurious resonance in the impurity spectral function at $\omega = 0$ and the NCA analysis then even fails in the high-temperature regime $T \gg T_K$. As by contrast the NRG is by construction well suited for low temperature spectral information, even with a locally applied field, we decided to use the NRG instead of the NCA in our mean-field treatment of europium oxide (for details, see chapter 3.4.1).

2.2.4 Advanced NCA techniques: SUNCA and CTMA

For finite Coulomb interaction U , contributions from both virtual excitations to the empty state and to the double occupied impurity state play a role in the exchange coupling J . Simply modifying the NCA such that second order perturbation theory is added for both of these processes fails since one cannot capture the simultaneous contribution of both channels in each order of bare perturbation theory correctly. An infinite summation of vertex corrections (the symmetrized finite- U NCA or SUNCA [37]) cures this problem [23].

To overcome the failures of the NCA in the low temperature regime $T \ll T_K$, proper vertex corrections which account for the dominant spin and charge fluctuations have to be taken into account. The conserving T -matrix approximation (CTMA) is able to reproduce the correct FL behavior of the SIAM strong coupling fixed point [23].

2.2.5 The NCA for multi-orbital Anderson impurities

In contrast to the NRG, conserving techniques can be generalized in a straightforward way to include more than one local impurity orbital. Consequently, the low energy spectra of transition and rare earth metal systems could be understood on the level of the NCA, specifically experimental photoemission spectroscopy (PES) data of a cerium (Ce) impurity in a metallic host were explained in [38]. There the results of the multi-orbital impurity model are in striking agreement with the PES data of the heavy fermion compound CeCu_2Si_2 .

Ce, as a 4f system, has seven spin-degenerate levels, which are split by spin-orbit (SO) coupling into a total angular momentum $J = 5/2$ sextet and an excited $J = 7/2$ octet, which is in turn split by crystal field (CF) interaction into three and four Kramers' degenerate doublets, respectively. It is known from inverse photoemission spectroscopy (IPES) that the on-site Coulomb repulsion U between all 4f orbitals is substantially larger than the single particle energies $|\varepsilon_{fm}|$ and thus the overall valence of the orbitals is close to 1. Hence for $U \rightarrow \infty$ the model Hamiltonian reads

$$H = \sum_{\vec{k}\sigma} \varepsilon_{\vec{k}} c_{\vec{k}\sigma}^\dagger c_{\vec{k}\sigma} + \sum_{m\sigma} \varepsilon_{fm} f_{m\sigma}^\dagger f_{m\sigma} + \sum_{m\vec{k}\sigma} \left(V_{\vec{k}m} c_{\vec{k}\sigma}^\dagger f_{m\sigma} + h.c. \right), \quad (2.11)$$

where $c_{\vec{k}\sigma}^\dagger$ describes creation operators for electrons with spin σ . $\varepsilon_{fm} < E_F$, $m = 1 \dots 7$ are the seven SO and CF split 4f single-particle levels with creation operators $f_{m\sigma}^\dagger$. The hybridization matrix elements $V_{\vec{k}m}$ lead to an effective coupling matrix $\Gamma_{mm'} = \pi \sum_{\vec{k}} V_{m\vec{k}}^* A_{\vec{k}}(\omega) V_{\vec{k}m'}$, where $A_{\vec{k}}(\omega)$ is the conduction electron spectral function.

As shown in Fig. 2.3 the spectrum gets some generical features (peaks A-F).

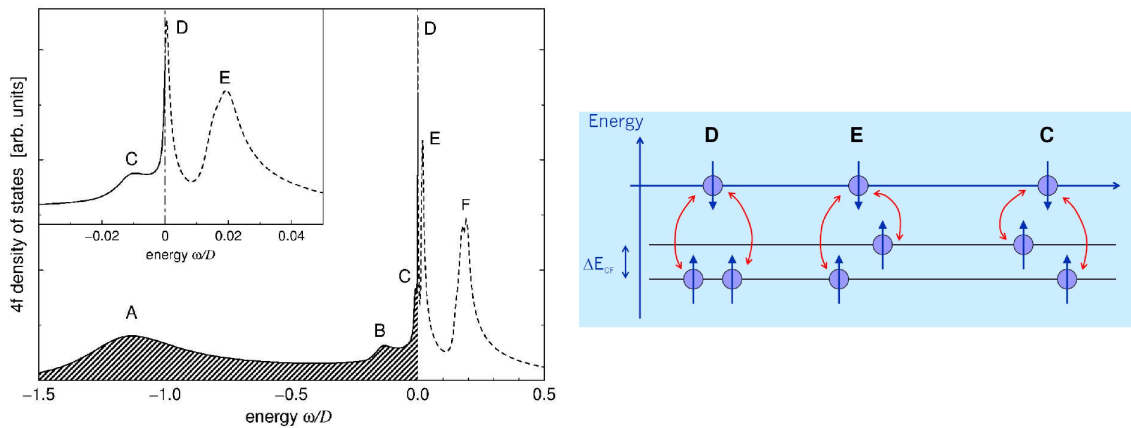


Figure 2.3: *Left:* Sketch of the theoretical 4f spectral function from calculations based on the multi-orbital SIAM, using the NCA. Figure taken from [38]. *Right:* Sketch of the spin-flip events responsible for the CF satellites (C,E) and the Kondo peak (D)

While there is the usual Kondo resonance (D) at the Fermi level and the 'single-particle peak' (A) at ε_{fm} (more precisely that is a superposition of all seven single-particle peaks, thus better termed $4f^1 \rightarrow 4f^0$ ionization peak of width $\Gamma \approx \sum_m \Gamma_{1m}$), additional structure in the form of satellite peaks appears. Due to spin-flip scattering with CF (peaks C and E) or SO (peaks B and F) excited impurity levels as initial or final state, Kondo resonances show up in pairs approximately symmetrical around E_F (see also Fig. 2.3). While the peaks above E_F carry significant spectral weight, below the Fermi level the satellites often appear as mere 'shoulders'. This is because in this case the virtual transition starts from an excited level, which is only thermally populated. Thus the transition carries a detailed balance factor $w = n^i(1 - n^f)$, where n^i (n^f) is the occupation of the 4f orbital in the initial (final) state. Reinert *et al.* [38] were able to explain the PES data of CeCu_2Si_2 with this multi-orbital NCA (see Fig. 2.4).

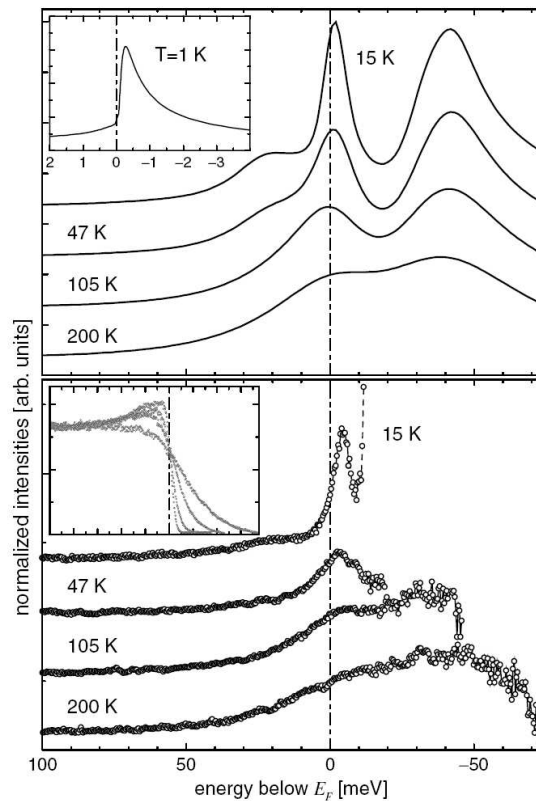


Figure 2.4: *Upper panel:* Theoretical T -dependence of the 4f spectra using the multi-orbital NCA. *Lower panel:* Photoemission spectra of CeCu_2Si_2 , normalized to the same intensity at 100 meV. Above E_F the experimental spectra are divided by the Fermi-Dirac distribution up to $5k_B T$. Figure taken from [38].

The results of the multi-orbital NCA will be the starting point for our program devel-

oped to analyze the scanning tunneling microscopy (STM) experiments of transition metal atoms on metal surfaces (see chapter 5).

Chapter 3

The Numerical Renormalization Group (NRG)

This chapter gives a detailed description of the numerical renormalization group (NRG) procedure, which was set up for this thesis.

The NRG was developed in the 1970s by K. G. Wilson to investigate the Kondo problem. Wilson was the first one who constructed a non-perturbative solution of the one-channel Kondo model [3]. Krishna-murthy *et al.* applied the NRG method to evaluate static properties of the Anderson model, as e. g. the temperature dependence of the magnetic susceptibility [9, 10]. The first calculation of dynamical properties were described for the first time by Frota and Oliveira [39] and Sakai *et al.*[40]. Later Costi and Hewson [41, 42, 43] determined besides the spectral function also transport properties like electrical resistivity, thermopower, thermal conductivity and Hall coefficient via the NRG.

The calculations were done assuming a flat conduction band (CB), which is equivalent to an energy-independent hybridization between impurity and conduction electrons. For the application of the NRG in dynamical mean-field theory (DMFT) calculations, however, it turns out that an arbitrary density of states (DoS) of the conduction band is important (see also section 3.4). This generalization was developed by Bulla [44, 45] for the single-impurity Anderson model (SIAM).

The NRG is a powerful method for quantum impurity problems. Besides for the explanation of the original, one-channel Kondo model it has widely been used in the context of more complex models with e. g. more than one conduction electron band. It gives valuable assistance in the investigation of modern physical experiments like semiconductor quantum dots. Particularly it serves as a reliable 'impurity solver' in DMFT calculations. We shortly describe further recent extensions to the NRG like the calculation of time-dependent problems in later sections. The derivations in the following sections use in part derivations also made by [46, 47].

3.1 The NRG procedure

3.1.1 Model Hamiltonian

The crucial step in the NRG procedure will be the mapping of the conduction band electrons onto a semi-infinite chain, the *Wilson chain*. For simplicity the calculations in this chapter are restricted to the SIAM, but can be extended to more complicated models as e. g. multi-channel Kondo models straightforwardly (see chapter 4). Our starting point is the Hamiltonian of the SIAM, as already introduced in chapter 1.2:

$$\mathcal{H}_{SIAM} = \underbrace{\sum_{\sigma} \varepsilon_d d_{\sigma}^{\dagger} d_{\sigma}}_{\mathcal{H}_d} + U d_{\uparrow}^{\dagger} d_{\uparrow} d_{\downarrow}^{\dagger} d_{\downarrow} + \underbrace{\sum_{\vec{k}\sigma} \varepsilon_{\vec{k}\sigma} c_{\vec{k}\sigma}^{\dagger} c_{\vec{k}\sigma}}_{\mathcal{H}_c} + \underbrace{\sum_{\vec{k}\sigma} V_{\vec{k}\sigma} \left(d_{\sigma}^{\dagger} c_{\vec{k}\sigma} + c_{\vec{k}\sigma}^{\dagger} d_{\sigma} \right)}_{\mathcal{H}_{hyb}} \quad (3.1)$$

The single impurity level (with the usual electron creation operator d_{σ}^{\dagger} and on-site Coulomb term U) is described by \mathcal{H}_d and embedded in a conduction band¹ with dispersion $\varepsilon_{\vec{k}\sigma}$ (described by \mathcal{H}_c). \mathcal{H}_d and \mathcal{H}_c are coupled via an energy dependent hybridization $V_{\vec{k}\sigma}$.

For the derivation of the NRG equations, a continuous representation of the Hamiltonian (3.1) is more convenient [45]:

$$\mathcal{H}_{SIAM} = \mathcal{H}_d + \sum_{\sigma} \int_{-1}^1 d\varepsilon g_{\sigma}(\varepsilon) a_{\varepsilon\sigma}^{\dagger} a_{\varepsilon\sigma} + \sum_{\sigma} \int_{-1}^1 d\varepsilon h_{\sigma}(\varepsilon) \left(d_{\sigma}^{\dagger} a_{\varepsilon\sigma} + a_{\varepsilon\sigma}^{\dagger} d_{\sigma} \right) \quad (3.2)$$

Here a one-dimensional energy representation for the CB was introduced with band cut-offs at ± 1 , dispersion $g_{\sigma}(\varepsilon)$ and hybridization $h_{\sigma}(\varepsilon)$. The continuous CB operators fulfil standard fermionic anti-commutation rules: $\{a_{\varepsilon\sigma}^{\dagger}, a_{\varepsilon'\sigma'}\} = \delta_{\sigma\sigma'} \delta(\varepsilon - \varepsilon')$. The equivalence of the Hamiltonians (3.1) and (3.2) was shown in [45] by proving that a specific choice of $g_{\sigma}(\varepsilon)$ and $h_{\sigma}(\varepsilon)$ leads to the same effective action on the impurity degree of freedom. If one defines the following hybridization function

$$\Delta_{\sigma}(\varepsilon) = \pi \rho_{\sigma}(\varepsilon) [V_{\sigma}(\varepsilon)]^2, \quad (3.3)$$

the equivalence of the effective actions is only fulfilled when the following relation holds:

$$\pi \frac{dg_{\sigma}^{-1}(\varepsilon)}{d\varepsilon} [h_{\sigma}(g_{\sigma}^{-1}(\varepsilon))]^2 = \Delta_{\sigma}(\varepsilon) \quad (3.4)$$

where $g_{\sigma}^{-1}(\varepsilon)$ is the inverse function of $g_{\sigma}(\varepsilon)$.

¹The density of states $\rho_{\sigma}(\varepsilon)$ of the conduction band relates to the energy dispersion as follows: $\rho_{\sigma}(\varepsilon) = \sum_{\vec{k}} \delta(\varepsilon - \varepsilon_{\vec{k}\sigma})$

For a given $\Delta_\sigma(\varepsilon)$ there are many ways of satisfying Equation (3.4). For a sufficiently smooth (or even constant) hybridization $\Delta_\sigma(\varepsilon)$ one can choose:

$$g_\sigma(\varepsilon) = \varepsilon \quad \text{and} \quad [h_\sigma(\varepsilon)]^2 = \frac{1}{\pi} \Delta_\sigma(\varepsilon) \quad (3.5)$$

For an energy-dependent hybridization [48], however, this choice has a conceptual disadvantage arising from the logarithmic discretization of the conduction band (see next sections). In this case, the energy-dependence of $\Delta_\sigma(\varepsilon)$ is taken into account in the hybridization by defining $[h_\sigma(\varepsilon)]^2$ as a mean value in each interval of the logarithmic discretization. The remaining energy dependence will be incorporated in the dispersion $g_\sigma(\varepsilon)$ (for details, see [45]).

3.1.2 Logarithmic discretization

As Eq. 3.2 implies, the impurity couples via $V_\sigma(\varepsilon)$ to all energy scales in the problem (as depicted in Figure 3.1).

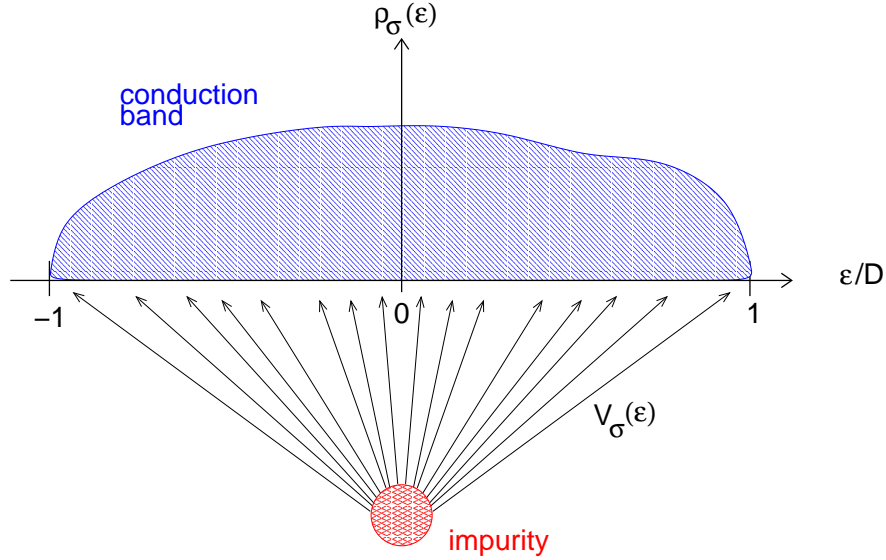


Figure 3.1: The impurity couples to all energy scales

As one is interested mainly in the low-temperature properties of the system, Wilson's ingenious idea was to logarithmically discretize the conduction band with a discretization parameter $\Lambda > 1$ [3] (see Figure 3.2). This enabled him to take all energy scales into account (which is the central idea of Anderson's scaling approach) and resolve the low-energy excitations with high accuracy. The parameter Λ defines a set of intervals with discretization points

$$x_n = \Lambda^{-n} \quad (3.6)$$

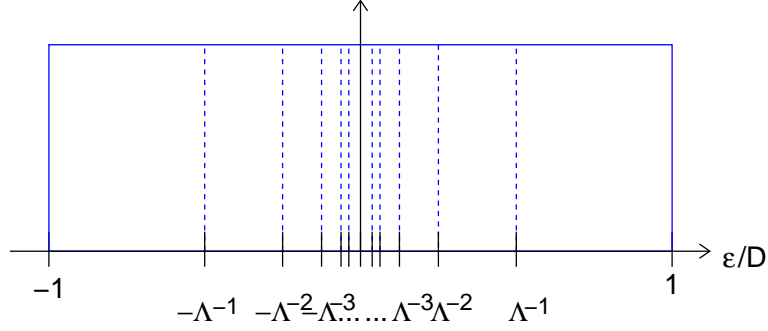


Figure 3.2: Logarithmic discretization of a flat conduction band

and width $d_n = \Lambda^{-n}(1 - \Lambda^{-1})$. Within each logarithmic interval a Fourier series is defined:

$$\psi_{np}^{\pm}(\varepsilon) = \begin{cases} \frac{1}{\sqrt{d_n}} e^{\pm i\omega_n p \varepsilon} & \text{for } x_{n+1} < \pm \varepsilon < x_n \\ 0 & \text{outside this interval} \end{cases} \quad (3.7)$$

($p \in \mathbb{Z}$ and $\omega_n = 2\pi/d_n$). n is the interval index, p the harmonic index of the Fourier expansion and the superscript $+$ ($-$) denotes a basis function defined for positive (negative) energies.

Now the continuous operators $a_{\varepsilon\sigma}$ and $a_{\varepsilon\sigma}^{\dagger}$ can be expanded in this complete set of orthonormal functions:

$$a_{\varepsilon\sigma} = \sum_{np} [a_{np\sigma} \psi_{np}^+(\varepsilon) + b_{np\sigma} \psi_{np}^-(\varepsilon)] \quad (3.8)$$

$$a_{np\sigma} = \int_{-1}^1 d\varepsilon [\psi_{np}^+(\varepsilon)]^* a_{\varepsilon\sigma},$$

$$b_{np\sigma} = \int_{-1}^1 d\varepsilon [\psi_{np}^-(\varepsilon)]^* a_{\varepsilon\sigma},$$

The operators $a_{np\sigma}$ and $b_{np\sigma}$ form a complete set of independent, *discrete*, electron operators obeying the usual fermionic anti-commutation rules. Consequently, the continuous Hamiltonian (Eq. 3.2) can now be expressed in terms of discrete operators.

In order to transform the hybridization part, one takes the hybridization function $h_{\sigma}(\varepsilon)^2$ as the mean value in each logarithmic interval:

$$[h_{n\sigma}^{\pm}]^2 = \frac{1}{d_n} \int^{\pm} d\varepsilon \frac{1}{\pi} \Delta_{\sigma}(\varepsilon) \quad (3.9)$$

where we have defined

$$\int^+ d\varepsilon \equiv \int_{\Lambda^{-n-1}}^{\Lambda^{-n}} d\varepsilon \quad \int^- d\varepsilon \equiv \int_{-\Lambda^{-n}}^{-\Lambda^{-n-1}} d\varepsilon \quad (3.10)$$

As long as $h_\sigma(\varepsilon)^2$ is constant in each interval, the impurity couples to the average component ($p = 0$) of the conduction electrons only (Riemann-Lebesgue Lemma) [45, 46], and consequently the $p \neq 0$ -states can be neglected. The remaining energy dependence will be incorporated in the dispersion $g_\sigma(\varepsilon)$ such that the relation (3.4) still holds. In general, the resulting dispersion will be non-linear, but is leading to a scaling behavior of the resulting hopping matrix elements $t_{n\sigma} \propto \Lambda^{-n/2}$ (see next chapter). The representation Eq. (3.5) would lead to a scaling behavior with an effective Λ_{eff} not equal to Λ which might even depend on the number of iterations, thus making the analysis more difficult [45]. The choice (3.9) leads to a transformation of the hybridization part to the following form:

$$\mathcal{H}_{hyb} = \sqrt{\frac{1}{\pi}} \sum_{\sigma} \left[d_{\sigma}^{\dagger} \sum_n (\gamma_{n\sigma}^{+} a_{n\sigma} + \gamma_{n\sigma}^{-} b_{n\sigma}) + h.c. \right] \quad (3.11)$$

with

$$\gamma_{n\sigma}^{\pm} = \sqrt{\int^{\pm} d\varepsilon \Delta_{\sigma}(\varepsilon)} \quad (3.12)$$

If one now defines a fermionic operator $c_{0\sigma}$ of the form

$$c_{0\sigma} \equiv \frac{1}{\sqrt{\xi_{0\sigma}}} \sum_n (\gamma_{n\sigma}^{+} a_{n\sigma} + \gamma_{n\sigma}^{-} b_{n\sigma}) \quad (3.13)$$

with

$$\xi_{0\sigma} = \sum_n \left((\gamma_{n\sigma}^{+})^2 + (\gamma_{n\sigma}^{-})^2 \right) = \int_{-1}^1 d\varepsilon \Delta_{\sigma}(\varepsilon), \quad (3.14)$$

the hybridization term finally takes the following, simple form:

$$\mathcal{H}_{hyb} = \int_{-1}^1 d\varepsilon h_{\sigma}(\varepsilon) (d_{\sigma}^{\dagger} a_{\varepsilon\sigma} + a_{\varepsilon\sigma}^{\dagger} d_{\sigma}) = \sum_{\sigma} \left[\sqrt{\frac{\xi_{0\sigma}}{\pi}} d_{\sigma}^{\dagger} c_{0\sigma} + h.c. \right], \quad (3.15)$$

which nicely illustrates that the impurity couples to a *single* fermionic degree of freedom only.

The expansion of the conduction electron part within the new basis (3.8) reads:

$$\mathcal{H}_c = \sum_{\sigma} \int_{-1}^1 d\varepsilon g_{\sigma}(\varepsilon) \sum_{npp'} \left[a_{np\sigma}^{\dagger} [\Psi_{np}^{+}(\varepsilon)]^{*} a_{np'\sigma} \Psi_{np'}^{+}(\varepsilon) + b_{np\sigma}^{\dagger} [\Psi_{np}^{-}(\varepsilon)]^{*} b_{np'\sigma} \Psi_{np'}^{-}(\varepsilon) \right] \quad (3.16)$$

As pointed out, with the choice (3.9) for the hybridization, only the ($p = 0$)-terms couple directly to the impurity. But through indirect coupling (via the ($p = 0$)-mode),

also the ($p \neq 0$)-contributions may become important. Therefore, the two following parts of the sum in (3.16) have to be considered:

$$\mathcal{H}_c = \mathcal{H}_c^{(1)} + \mathcal{H}_c^{(2)} = \sum_{p=0,p'} [\dots] = \sum_{p=0,p'=0} [\dots] + \sum_{p=0,p' \neq 0} [\dots] \quad (3.17)$$

The condition ($p = p' = 0$) reduces the Hamiltonian (3.16) to the form:

$$\mathcal{H}_c^{(1)} = \sum_{n\sigma} [\xi_{n\sigma}^+ a_{n\sigma}^\dagger a_{n\sigma} + \xi_{n\sigma}^- b_{n\sigma}^\dagger b_{n\sigma}] \quad (3.18)$$

with the single-particle energies $\xi_{n\sigma}^+$ and $\xi_{n\sigma}^-$ only depending on the integral over $g_\sigma(\varepsilon)$ [45]: $\xi_{n\sigma}^\pm = \frac{1}{dn} \int^\pm d\varepsilon g_\sigma(\varepsilon)$. Thus an exact knowledge of $g_\sigma(\varepsilon)$ (that could be obtained by solving the differential equation (3.4)) is not required. It is shown in [45] that the discrete energies $\xi_{n\sigma}^\pm$ can be calculated by

$$\xi_{n\sigma}^\pm = \frac{\int^\pm d\varepsilon \Delta_\sigma(\varepsilon) \cdot \varepsilon}{\int^\pm d\varepsilon \Delta_\sigma(\varepsilon)} \quad (3.19)$$

It can be seen that a linear dispersion ($g_\sigma(\varepsilon) = \varepsilon$) is recovered for constant hybridization (see (3.5)).

So far the mapping of the original Hamiltonian (3.1) to the discretized version is exact. What remains to be discussed is the second part $\mathcal{H}_c^{(2)}$ of the (pp')-sum in the conduction band Hamiltonian. As shown in [9], it reduces to

$$\mathcal{H}_c^{(2)} = \frac{1 - \Lambda^{-1}}{2\pi i} \sum_{n\sigma} \sum_{p \neq p'} \left[\frac{\Lambda^{-n}}{p' - p} (a_{np\sigma}^\dagger a_{np\sigma} - b_{np\sigma}^\dagger b_{np\sigma}) \exp \frac{2\pi i(p - p')}{1 - \Lambda^{-1}} \right] \quad (3.20)$$

The contribution of $\mathcal{H}_c^{(2)}$ vanishes in the limit $\Lambda \rightarrow 1$. As a first approximation, $\mathcal{H}_c^{(2)}$ is disregarded and the conduction band consist only of the first term of the (pp')-sum:

$$\mathcal{H}_c \approx \mathcal{H}_c^{(1)} \quad (3.21)$$

Wilson [3] showed in his calculations for the Kondo problem, that this is a good approximation even for a discretization parameter Λ as large as 3. In this thesis, mostly $\Lambda = 2$ was used.

Finally, the discretized version of the Hamiltonian, depicted in Figure 3.3, takes the form

$$\begin{aligned} \mathcal{H}_{SIAM} &= \sum_{\sigma} \varepsilon_d d_{\sigma}^{\dagger} d_{\sigma} + U d_{\uparrow}^{\dagger} d_{\uparrow} d_{\downarrow}^{\dagger} d_{\downarrow} \\ &+ \sum_{n\sigma} [\xi_{n\sigma}^+ a_{n\sigma}^\dagger a_{n\sigma} + \xi_{n\sigma}^- b_{n\sigma}^\dagger b_{n\sigma}] \\ &+ \sum_{\sigma} \left[\sqrt{\frac{\xi_{0\sigma}}{\pi}} d_{\sigma}^{\dagger} c_{0\sigma} + h.c. \right] \end{aligned} \quad (3.22)$$

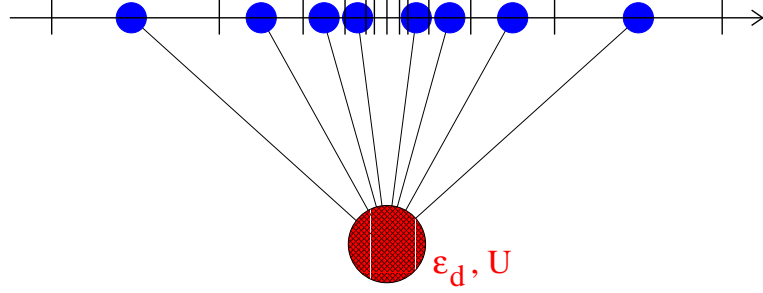


Figure 3.3: Discretized Anderson Hamiltonian

3.1.3 Mapping on a semi-infinite chain

In the discretized version (3.23) of the SIAM Hamiltonian, the impurity still couples to an infinite number of CB electrons (though only to the average part in each logarithmic interval). To solve the the system numerically, the conduction band part is mapped onto the semi-infinite (Wilson) chain:

$$\underbrace{\sum_{n=0,\sigma}^{\infty} (\xi_{n\sigma}^+ a_{n\sigma}^\dagger a_{n\sigma} + \xi_{n\sigma}^- b_{n\sigma}^\dagger b_{n\sigma})}_{\mathcal{H}_{cond.band}} = \underbrace{\sum_{n=0,\sigma}^{\infty} \left[\varepsilon_{n\sigma} c_{n\sigma}^\dagger c_{n\sigma} + t_{n\sigma} (c_{n\sigma}^\dagger c_{n+1\sigma} + h.c.) \right]}_{\mathcal{H}_{Wilsonchain}} \quad (3.23)$$

Therefore a tridiagonalization procedure developed by Lánczos [49] with diagonal matrix elements $\varepsilon_{n\sigma}$ and off-diagonal elements $t_{n\sigma}$ is used, equivalent to a Gram-Schmidt orthonormalization. Starting from an initial one-particle state $|\Psi_0\rangle = c_{0\sigma}^\dagger |0\rangle$ (where $|0\rangle$ denotes the Fock vacuum²), a new single-particle basis is constructed [46] according to:

$$\begin{aligned} & \overbrace{\langle \Psi_{n+1\sigma} | \mathcal{H}_{CB} | \Psi_{n\sigma} \rangle}^{t_{n\sigma}} | \Psi_{n+1\sigma} \rangle = \\ & \mathcal{H}_{CB} | \Psi_{n\sigma} \rangle - \underbrace{\langle \Psi_{n\sigma} | \mathcal{H}_{CB} | \Psi_{n\sigma} \rangle}_{\varepsilon_{n\sigma}} | \Psi_{n\sigma} \rangle - \underbrace{\langle \Psi_{n-1\sigma} | \mathcal{H}_{CB} | \Psi_{n\sigma} \rangle}_{t_{n-1\sigma}} | \Psi_{n-1\sigma} \rangle \end{aligned} \quad (3.24)$$

where the $c_{n\sigma}$ are defined via $|\Psi_n\rangle = c_{n\sigma}^\dagger |0\rangle$, $n \in \mathbb{N}$.

With a recursion procedure, described in appendix A, the coefficients $t_{n\sigma}$ and $\varepsilon_{n\sigma}$ can be determined with arbitrary precision routines for a spin- and energy-dependent hybridization $\Delta_\sigma(\varepsilon)$.

Note that for a flat conduction band, as in the original work of Wilson [3], and for a power-law density of states (in pseudo-gap Fermi systems) [45], analytical expressions

² $|\Psi_0\rangle$ is called the *maximally localized* state, since it is maximally delocalized in momentum space and hence maximally localized at the impurity site in position space

for the hopping matrix elements t_n exist. For the flat conduction electron DoS ($\Delta_\sigma(\varepsilon) = \Delta$), as also considered in Krishna-murthy *et al.*'s work [9], the hopping matrix elements are

$$t_{n\sigma} = \frac{1}{2} (1 + \Lambda^{-1}) \Lambda^{-n/2} \frac{\overbrace{1 - \Lambda^{-n-1}}^{\xi_n^K}}{\sqrt{(1 - \Lambda^{-(2n+1)})(1 - \Lambda^{-(2n+3)})}} \quad (3.25)$$

(Compare the ξ_n^K to Eq. (2.15) of [9] and the $t_{n\sigma}$ to Eq. (VII.35) of [3]). The $\varepsilon_{n\sigma}$ vanish for symmetric hybridization functions as considered in the original papers.

3.1.4 Iterative diagonalization

After mapping of the conduction electron part onto the semi-infinite Wilson chain (Eq. 3.23) one finally arrives at the following Hamiltonian

$$\begin{aligned} \mathcal{H}_{SIAM} &= \sum_{\sigma} \varepsilon_d d_{\sigma}^{\dagger} d_{\sigma} + U d_{\uparrow}^{\dagger} d_{\uparrow} d_{\downarrow}^{\dagger} d_{\downarrow} \\ &+ \sum_{n=0, \sigma}^{\infty} \left[\varepsilon_{n\sigma} c_{n\sigma}^{\dagger} c_{n\sigma} + t_{n\sigma} \left(c_{n\sigma}^{\dagger} c_{n+1\sigma} + h.c. \right) \right] \\ &+ \sum_{\sigma} \left[\sqrt{\frac{\xi_{0\sigma}}{\pi}} d_{\sigma}^{\dagger} c_{0\sigma} + h.c. \right], \end{aligned} \quad (3.26)$$

which has to be iteratively diagonalized *numerically*, hence giving the NRG its name.

The infinite-dimensional problem (compare Eq. (3.23)) is cast into the Wilson chain-Hamiltonian 3.26, which is sketched in Fig. 3.4.

The Hamiltonian 3.26 can be viewed as a series of Hamiltonians H_N ($N \geq -1$), whereas the original Hamiltonian \mathcal{H}_{SIAM} is recovered in the case of an infinitely long chain ($N \rightarrow \infty$):

$$\mathcal{H}_{SIAM} = \lim_{N \rightarrow \infty} \Lambda^{-(N-1)/2} H_N \quad (3.27)$$

with

$$H_N = \Lambda^{(N-1)/2} \left[U n_{\uparrow} n_{\downarrow} + \sum_{n=-1, \sigma}^N \varepsilon_{n\sigma} c_{n\sigma}^{\dagger} c_{n\sigma} + \sum_{n=-1, \sigma}^{N-1} t_{n\sigma} \left(c_{n\sigma}^{\dagger} c_{n+1\sigma} + c_{n+1\sigma}^{\dagger} c_{n\sigma} \right) \right] \quad (3.28)$$

For this short-hand notation it was defined: $c_{-1\sigma} \equiv d_{\sigma}$, $\varepsilon_{-1\sigma} \equiv \varepsilon_d$ and $t_{-1\sigma} = \sqrt{\frac{\xi_{0\sigma}}{\pi}}$. Here, H_{-1} corresponds to the impurity alone:

$$H_{-1} = \frac{1}{\Lambda} \left[\sum_{\sigma} \varepsilon_d d_{\sigma}^{\dagger} d_{\sigma} + U d_{\uparrow}^{\dagger} d_{\uparrow} d_{\downarrow}^{\dagger} d_{\downarrow} \right] \quad (3.29)$$

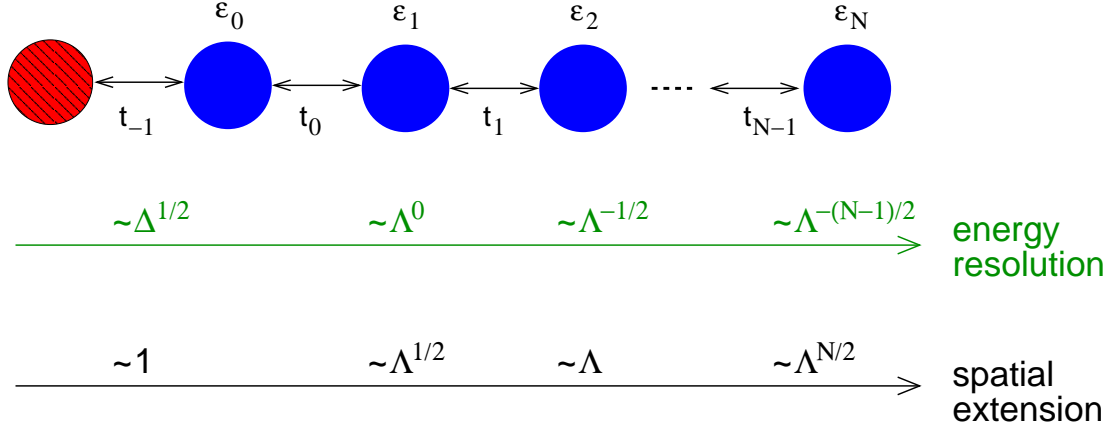


Figure 3.4: The Wilson chain: The impurity (*red*) couples to a semi-infinite chain of conduction electron ‘shell states’ (*blue*) with exponentially decreasing hopping matrix elements. Going along the chain, the energy resolution increases, while the states are spatially more and more extent. Thus this model is often referred to as “onion skin” model (see e.g the original work of Wilson [3]). As only neighbouring sites are coupled to each other, the Wilson chain Hamiltonian can be iteratively diagonalized.

Eq. (3.28) allows one to set up a renormalization group transformation R , which relates two successive Hamiltonians, i.e. two effective Hamiltonians on successively lower energy scales:

$$\begin{aligned}
 H_{N+1} &= R[H_N] \\
 &= \sqrt{\Lambda}H_N + \Lambda^{N/2} \sum_{\sigma} \varepsilon_{N+1\sigma} c_{N+1\sigma}^{\dagger} c_{N+1\sigma} \\
 &\quad + \Lambda^{N/2} \sum_{\sigma} t_{N\sigma} \left(c_{N\sigma}^{\dagger} c_{N+1\sigma} + c_{N+1\sigma}^{\dagger} c_{N\sigma} \right)
 \end{aligned} \tag{3.30}$$

Note that the rescaling factor $\Lambda^{(N-1)/2}$ is introduced in Eq. (3.28) to ensure that H_N contains numerically convenient numbers of $\mathcal{O}(1)$.

With the prescription described in this chapter for the Anderson model, it is fairly simple to solve also other models like e.g. the Kondo model: The only thing that has to be adjusted is the initial Hamiltonian H_0 . Here the coupling between impurity and 0^{th} site of the Wilson chain is $\sim J$.

The iterative solution can be described by the following algorithm (for details, see appendix A):

- (1) Initialize the start Hamiltonian:

All eigenenergies E_m and eigenstates $|\psi_m\rangle$ in a useful representation have to be computed (for the SIAM, this is just the impurity Hamiltonian H_{-1} , which is

4-dimensional). Eventually, for the calculation of correlation functions, initial matrix elements have to be set up (as e. g. $\langle \psi_m | d_\sigma | \psi_{m'} \rangle$).

- (2) Append one additional site of the Wilson chain ($H_N \rightarrow H_{N+1}$), according to Eq. 3.30, using the information of the previous NRG step.
- (3) Diagonalize the Hamiltonian ($H_{N+1} \rightarrow H_{N+1}^{diag}$) and store all eigenvalues and eigenvectors.
- (4) Calculation of an expectation value of any operator requires the knowledge of the corresponding matrix elements in the basis of H_{N+1}^{diag} .
- (5) Continue with step (2)

As the Hilbert space grows exponentially fast during the NRG procedure, one has to use a truncation scheme, where only a set of the lowest states are kept at each stage (see also next section about symmetries). Thus to succeed with the algorithm listed above, after the diagonalization (step (3)), one has to sort the spectrum with respect to increasing eigenenergies and truncate it such that enough information is retained (for the SIAM this is typically achieved with keeping ~ 500 states). This truncation scheme relies on the fact that the hopping matrix elements $t_{n\sigma}$ fall off exponentially. High energy states thus do not change the low frequency behavior and can safely be neglected. The fact that the $t_{n\sigma}$ fall off exponentially with n is a consequence of the logarithmic discretization rather than due to a special feature of the shape of the conduction band. In models, where the same energy scales are added at each step of the RG procedure (as e. g. in the one-dimensional Hubbard model), the NRG truncation scheme fails. The low energy spectrum of the cluster with one additional site depends on states from the whole energy spectrum of the previous iteration. One overcomes the problems if one uses another truncation scheme (see our section 2.1.2 about the DMRG).

3.1.5 Symmetries in the NRG

In the course of an NRG iteration, the most CPU expensive step is the diagonalization of the Hamiltonian H_{N+1} of size $N_{states,N+1} \times N_{states,N+1}$, including the determination of all eigenvectors. $N_{states,N+1}$ is typically in the order of $1000 \cdot 4 = 4000$ states for the one-channel case. Since these computational processes scale like N^3 it is crucial to exploit symmetries in the problem and divide the Hilbert space into smaller subspaces. Then each numerical diagonalization is carried out independently in each subspace. Although the logarithmic discretization together with this use of symmetries thins out the number of states to keep quite substantially with respect to the usual exact diagonalization approaches, the large degeneracy of states usually makes full diagonalization of H_{N+1} impossible. Explicitly, for the single impurity Anderson model as for the (one-channel) Kondo model, the degeneracy is 4^N at the N -th shell, thus allowing only for exact

diagonalization up to steps about $N = 7$ in a reasonable way. For the two-channel Kondo model, the degeneracy is even 16^N . To keep manageable numerics but still ensuring sufficient precision while solving the problem, one typically has to retain only the (energetically) lowest-lying few hundred states at each iteration. While there is no direct proof of this method, convergence tests in the original works [3, 9, 10] and *a posteriori* comparison with other exact methods (e.g. Bethe ansatz solutions) confirmed the validity of this approach [50].

For the usual SIAM or one-channel Kondo model (as well as the isotropic two-channel Kondo model), one may exploit the $SU(2)$ symmetry under spin rotations and use the total spin \hat{S}_{tot}^z and its z -component

$$\hat{S}_{tot}^z = \sum_{n=1,\sigma} \sigma c_{n\sigma}^\dagger c_{n\sigma} + S_I^z \quad (3.31)$$

as conserved quantities ($\sigma = \uparrow, \downarrow$ is the spin index and S_I^z the impurity spin). The implementation of the full spin symmetry would involve Clebsch-Gordon coefficients (see e.g. [9]). As the application of a magnetic field along the z -direction breaks the $SU(2)$ spin symmetry down to a $U(1)$ symmetry (with S_{tot}^z as the conserved charge), in the program developed in this thesis only S_{tot}^z is used as a good spin quantum number.

Since all the Hamiltonians considered conserve electron number, the use of another $U(1)$ -symmetry is reasonable. The conduction charge operator \hat{Q} (defined to be zero at half filling) is defined as follows:

$$\hat{Q} = \sum_{n,\sigma} \left[c_{n\sigma}^\dagger c_{n\sigma} - \frac{1}{2} \right] \quad (3.32)$$

For the calculations of the SIAM, the classification according to quantum numbers (Q, S_{tot}^z) together with retaining about 512 states was sufficient to obtain reliable results. In the calculations of higher-degenerate models (as the two-channel Kondo model), additional symmetries had to be used (see chapter 4).

3.1.6 Results of the iterative diagonalization

After step $(N + 1)$ in the NRG procedure, one gets the whole spectrum of eigenstates $|\psi_m\rangle_{N+1}$ ($m = 1 \dots N_{states,N+1}$) and eigenenergies E_m . As the N^{th} iteration corresponds to a computation at a scale $\omega_N \sim \Lambda^{-(N-1)/2} D$, one can deduce the energy dependence (or equivalently the temperature dependence) of every thermodynamic quantity. Usually, one proceeds with the NRG iterations until the spectrum does not change anymore and, in RG language, a stable *fixed point* is reached. By analyzing the structure of the fixed point and calculating perturbative corrections about it, Wilson [3] and Krishna-murthy *et al.* [9, 10] were able to confirm the strong-coupling fixed point in the Kondo model, i. e. that the impurity spin is completely screened. Furthermore,

they approved that the thermodynamic properties are Fermi-liquid like on approaching the fixed point (for details, see the next chapter).

Besides the energy spectrum one obtains information on dynamic quantities such as the impurity spectral function $A_{d\sigma}(\omega)$ by evaluating matrix elements of the involved operators (in this case of the impurity operator d_σ). Details on the calculation of dynamic quantities are also found in the following sections.

3.2 Measurements with the NRG

In the following chapter, we present the results which can be obtained with the program which was set up for this thesis. We begin with the confirmation of the original results of Wilson and Krishna-murthy *et al.* In addition to this 'basic' NRG code, we implemented the extension to allow for the calculation of the impurity spectral function, as described in the subsequent section.

3.2.1 Fixed points, the free electron Hamiltonian

In this section, the numerical results for the energy levels of the symmetric SIAM will be presented for typical values of Δ and U . What is important to notice is that the results can be understood in terms of H_N crossing over between various fixed points of the RG transformation 3.30 as N increases (which corresponds to going down in energy).

A 'fixed point' is reached, when the energy eigenvalues do not change from one to the next NRG step. This can be seen from the definition of a fixed point H^* of a renormalization group transformation R :

$$R[H^*] = H^*$$

Actually R itself does not have any fixed points, but R^2 (R operating twice), taking H_N to H_{N+2} , does. One realizes the occurrence of a fixed point in the numerical results, if one finds a set of energy levels that change very little from iteration N to iteration $(N + 2)$.

The free electron Hamiltonian

The interesting fixed points of the symmetric SIAM can be understood easily once one understands the structure of the free electron Hamiltonian H_N^0 . That corresponds to the situation where no impurity is present:

$$H_N^0 = \Lambda^{(N-1)/2} \sum_{n=0,\sigma}^{N-1} t_{n\sigma} \left(c_{n\sigma}^\dagger c_{n+1\sigma} + c_{n+1\sigma}^\dagger c_{n\sigma} \right), \quad (3.33)$$

where we supposed a flat conduction band and thus all on-site energies $\varepsilon_{n\sigma}$ of the Wilson chain to be zero.

As Eq. 3.33 denotes a quadratic form, it can be diagonalized exactly into $(N + 1)$ single-particle levels, as shown in the original NRG papers [3, 9]. The single-particle energies are the eigenvalues of the $(N + 1) \times (N + 1)$ matrix \mathcal{H}_N^0 whose only non-zero matrix elements are

$$(\mathcal{H}_N^0)_{n,n+1} = (\mathcal{H}_N^0)_{n+1,n} = \Lambda^{(N-1)/2} t_n, \quad (3.34)$$

where we have dropped the spin index σ .

By numerical diagonalization we find the eigenvalues η_j of \mathcal{H}_N^0 , which occur symmetrically ($\pm\eta_j$) due to the particle-hole symmetry of H_N^0 . When $(N + 1)$ is even there are $\frac{1}{2}(N + 1)$ positive eigenvalues, which are denoted by $\eta_j(N)$ and the rest are the negative ones. For $(N + 1)$ odd, there is one zero eigenvalue, denoted $\hat{\eta}_0$ and $\frac{1}{2}N$ positive eigenvalues $\hat{\eta}_j(N)$. What one finds on evaluating $\eta_j(N)$ and $\hat{\eta}_j(N)$ for a given Λ is that they approach limiting values η_j^* and $\hat{\eta}_j^*$, respectively, as N increases. As an example, at $\Lambda = 2.5$ one has

$$\eta_j^* : \quad 0.74686, 2.49321, 6.24999, (2.5)^3, (2.5)^4, \dots, (2.5)^{j-1} \quad (N + 1) \text{ even}; \quad (3.35)$$

$$\hat{\eta}_j^* : \quad 1.52048, 3.95255, 9.88212, (2.5)^{7/2}, \dots, (2.5)^{j-1/2} \quad (N + 1) \text{ odd}; \quad (3.36)$$

The free electron Hamiltonian H_N^0 can now be built up out of these single-particle levels.

For a successfully implemented NRG code one can check whether the single particle levels are obtained in the non-interacting limit $\Delta = 0$.

Fixed points for the symmetric SIAM

All fixed points (FPs) of the symmetric Anderson model can be obtained by choosing special values for Δ and U and comparing the resulting Hamiltonian H_N (Eq. 3.28) (in the limit $N \rightarrow \infty$) to the free electron Hamiltonian. The fixed points are

- (1) *Free orbital FP*: In the limit $\Delta = 0$ and $U = 0$, the impurity is decoupled from the conduction electrons and the effective free orbital Hamiltonian $H_{N,FO}^*$ is just the free electron Hamiltonian plus a free-impurity orbital of zero energy.
- (2) *Local moment FP*: Suppose that, keeping Δ fixed, one lets U become larger than the energies of interest. This would mean that it is energetically favourable to occupy the impurity by just one electron. In other words it is as if the impurity has become a 'local moment' of spin- $\frac{1}{2}$, leading to the local moment fixed point Hamiltonian $H_{N,LM}^*$.
- (3) *Strong coupling FP*: When the impurity is infinitely strong bound to the conduction electrons ($\Delta \rightarrow \infty$) at fixed U , the fixed point Hamiltonian $H_{N,SC}^*$ corresponds to the situation where the impurity and the first site of the Wilson

chain are bound into a singlet and effectively 'frozen out' from the rest of the chain. Thus the strong coupling fixed point levels for odd N correspond to the decoupled (free orbital) FP levels for even N .

Numerical results for the energy levels

By plotting the energy eigenvalues of each step versus the step number N , one can study the RG 'flow' during an NRG procedure. In doing so, one realizes that the spectra for an even number of iterations N differ from those with odd N . The reason for this *even-odd alternation* can be understood in the non-interacting limit $V \rightarrow 0$: For an even number of shells there is an odd number of electrons at half-filling and thus the Fermi level cuts right through a level which is two-fold degenerate because of the spin. For an odd number of shells (and thus an even number of electrons) the Fermi level passes through a gap above a non-degenerate Fermi sea.

Figure 3.5 shows the low-lying energy levels for the SIAM for the same parameters as chosen by Krishna-murthy *et al.* in their Fig. 5 [9], plotted versus odd iteration number N . There are three different fixed point (FP) regimes visible: For small N there is an unstable high-energy fixed point, the free orbital FP. At intermediate N the flow goes to another unstable FP, which turns out to be the local moment FP. Finally, for low energies (large N), we arrive at the stable strong coupling fixed point.

The crossover at large N from the local moment fixed point to the low energy strong coupling fixed point is associated with the Kondo scale T_K . As the temperature is related to the iteration number N as $k_B T = \Lambda^{-(N-1)/2}$, the scale of the crossover N_K corresponds to T_K according to:

$$N_K = \left(1 - 2 \frac{\log k_B T_K}{\log \Lambda} \right) \quad (3.37)$$

Note that the single-particles for η_j^* and $\hat{\eta}_j^*$, which are also indicated in Fig. 3.5, agree well with the fixed point energy levels.

The parameters of the SIAM can be chosen such that the flow goes directly from the high-energy free orbital fixed point to the low-energy strong coupling fixed point, without passing the local moment regime. This is shown in Fig. 3.6. Again, the fixed point energy levels can be associated with the eigenenergies η_j^* and $\hat{\eta}_j^*$ of the free electron Hamiltonian. The fact that one passes the various fixed points can also be seen in the static susceptibility data (see next section). First we want to comment on further conclusions which can be drawn out of the energy level flow diagrams.

Effective Hamiltonians

In the vicinity of a fixed point H^* of R^2 , one can carry out analytic calculations by setting up effective Hamiltonians

$$H_{eff} = H^* + \sum_l w_l O_l, \quad (3.38)$$

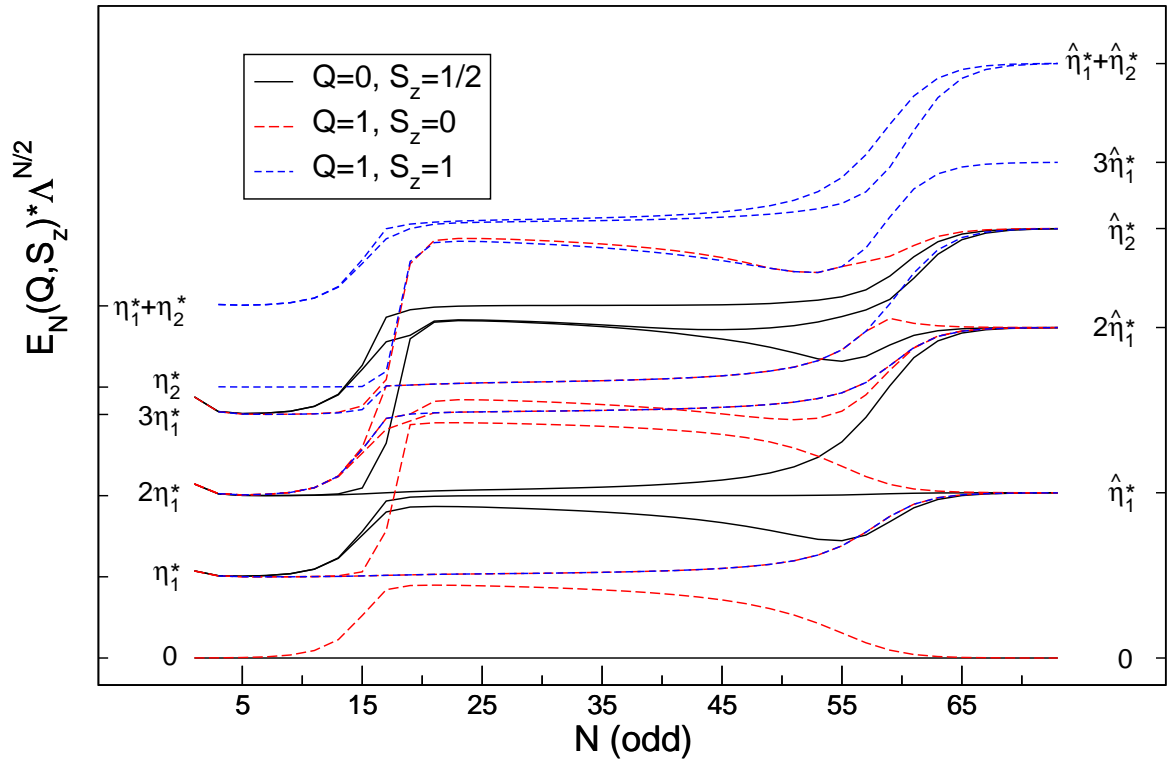


Figure 3.5: NRG energy flow diagram of the SIAM for the low-lying energy levels of H_N as a function of odd N . Parameters are: $U/D = 10^{-3}$, $U/\pi\Delta = 12.66$, $\Lambda = 2.5$ with 550 states kept in each iteration. Compare to Fig. 5 of [9]. The following fixed-point regimes are visible: Free orbital for $5 < N < 15$, local moment for $20 < N < 50$ and strong coupling for $N > 65$.

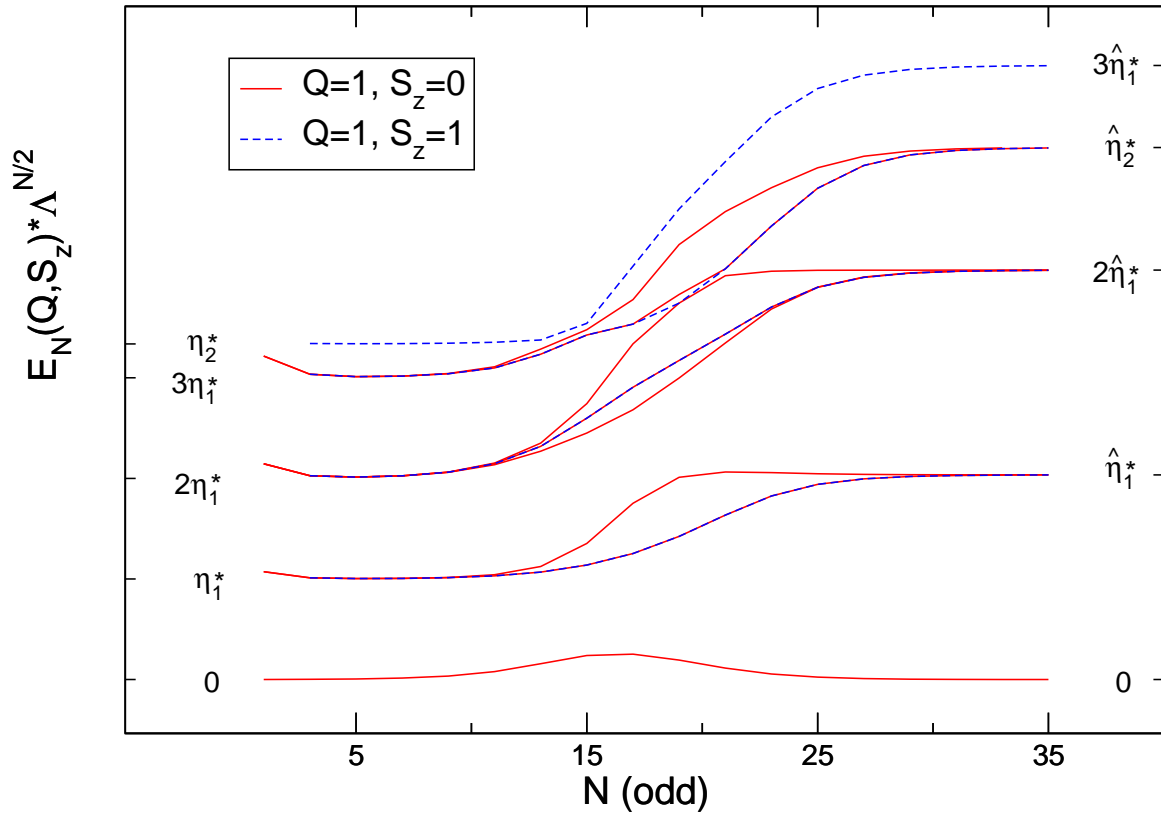


Figure 3.6: NRG energy flow diagram of the SIAM for the low-lying energy levels of H_N as a function of odd N . Parameters are: $U/D = 10^{-3}$, $U/\pi\Delta = 1.013$, $\Lambda = 2.5$ with 550 states kept in each iteration. Compare to Fig. 6 of [9]. The crossover happens from the free orbital regime at low N to the strong coupling regime at large N , without passing through the local moment regime.

where the leading deviations O_l about H^* are obtained by general symmetry arguments. For instance for the symmetric SIAM one has to consider operators δH that conserve charge, spin and particle-hole symmetry. Near any fixed point, one fits the energy spectra to the following form

$$H_{N,eff} = H_N^* + w_1 \Lambda^{(N-1)/2} \delta H_1 + w_2 \Lambda^{(N-1)/2} \delta H_2 + \dots \quad (3.39)$$

and determines the coefficients w_l . For further details we refer to a detailed description of this procedure in the original NRG works [3, 9].

The main results of this analytic treatment around the fixed points were

- (1) Right at the strong coupling fixed point, the impurity spin is completely screened.
- (2) On approaching the fixed point, the magnetic susceptibility $\chi(T)$ converges to a constant value for $T \rightarrow 0$ and the specific heat $C = \gamma T$ is linear in T for $T \rightarrow 0$.
- (3) The ratio $R = \chi/\gamma$, known as the *Wilson ratio*, takes the universal value $R = 2$ in the Kondo model.

3.2.2 Static properties, thermodynamics

As one calculates the whole many-body eigenstates and eigenvalues, one can in principle calculate every desired thermodynamic quantity. If one denotes the many-body eigenvalues of the Hamiltonian H with E_m and the eigenstates $|m\rangle$, one sees that out of

$$H = \sum_m E_m |m\rangle \langle m| \quad (3.40)$$

one can calculate the partition function

$$Z(T) \equiv \text{Tr} e^{-H/k_B T} = \sum_m e^{-E_m/k_B T} \quad (3.41)$$

and hence the complete thermodynamics.

In the NRG procedure we are only able to calculate partition functions Z_N for the sequence of truncated Hamiltonians H_N .

$$Z_N(T) \equiv \text{Tr} e^{-H_N/k_B T} = \sum_m e^{-E_m^N/k_B T} \quad (3.42)$$

For a reasonable thermodynamic calculation one has to retain enough states at each iteration so that the contribution to the partition function from excited states, not contained in Z_N , is negligible. The truncation error made in replacing H by H_N was estimated in [9] to be approximately $\Lambda^{-1} D_N / k_B T_N$.

Thus the choice $k_B T = k_B T_N \approx D_N$ is reasonable and the thermodynamics can be calculated at a sequence of decreasing temperatures $k_B T_N \sim D_N = \Lambda^{-(N-1)/2} D$.

As every property is calculated as an impurity contribution, one always has to subtract out the values when no impurity is present. The definitions for the (zero-field) static magnetic susceptibility, the free energy, entropy and specific heat are

$$\chi_{imp}(T) = \frac{(g\mu_B)^2}{k_B T} \left(\frac{1}{Z} \text{Tr} (S_z^{tot})^2 e^{-H/k_B T} - \frac{1}{Z_c} \text{Tr} (S_{z,c}^{tot})^2 e^{-H_c/k_B T} \right) \quad (3.43)$$

$$F_{imp}(T) = -k_B T (\ln Z - \ln Z_c) \quad (3.44)$$

$$S_{imp}(T) = -\frac{\partial F_{imp}(T)}{\partial T} \quad (3.45)$$

$$C_{imp}(T) = -T \frac{\partial^2}{\partial T^2} F_{imp}(T), \quad (3.46)$$

with the partition functions $Z = \text{Tr} e^{-H/k_B T}$ and $Z_c = \text{Tr} e^{-H_c/k_B T}$. The subscript 'c' refers to the non-interacting conduction electrons alone.

With this definitions, we calculated the impurity susceptibility for the same parameters as considered for Fig. 3.5 and Fig. 3.6. The results are shown in Figure 3.7 and are plotted in the form $k_B T \chi(T)$ vs $\ln(k_B T/D)$. The reason for this seemingly unconventional choice is that one makes a one to one correspondence between such a plot and the development of H_N with N as discussed in the previous section.

If one compares Fig. 3.5 with the black curve of Fig. 3.7, which both correspond to the same parameters $U/\pi\Delta = 12.66$, one realizes for small N , thus for high energies, that the main contribution to the susceptibility contribution Eq. 3.43 comes from the free orbital fixed point $H_{N,FO}^*$. This is just the free electron Hamiltonian H_N^0 plus a free impurity orbital and thus for $k_B T \chi$ one just gets $\frac{1}{8}$. If the flow goes to the local moment fixed point $H_{N,LM}^*$, the resulting answer for $k_B T \chi$ would be the value $\frac{1}{4}$, characteristic of a free spin- $\frac{1}{2}$ impurity. As the temperature is decreased further, the gradual crossover of H_N to the strong coupling fixed point $H_{N,SC}^*$ is observed. As was shown in [9], the replacement of H_N by $H_{N,SC}^*$ in Eq. 3.43 makes $k_B T \chi$ vanish.

We note that a precise determination of susceptibilities and specific heats requires a careful analysis of the influence of the discretization parameter Λ . Large values of Λ pushes the procedure away from the continuum, introducing errors in the calculation of physical properties, like oscillations in the susceptibility curves [51]. A simple procedure that eliminates the artificial susceptibility oscillations and yields accurate results for discretizations Λ as large as 10 was developed by [52].

3.2.3 Dynamical properties

The generalization of the NRG to the calculation of dynamical properties requires the knowledge of additional matrix elements and therefore a significantly enhanced numerical effort. The first calculations of the impurity spectral function for the SIAM were obtained by Frota and Oliveira [39], Sakai *et al.* [40] and Costi and Hewson [41].

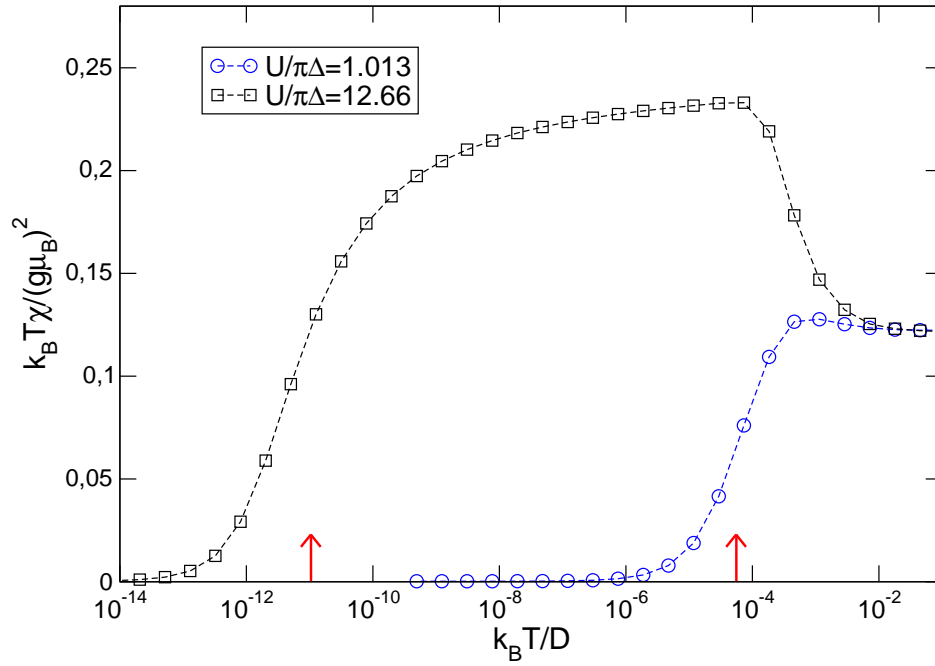


Figure 3.7: Plots of $k_B T \chi(T) / (g \mu_B)^2$ vs $\ln(k_B T / D)$ for $U/D = 10^{-3}$ and two different $U/\pi\Delta$. Compare Figure 9 of [9]. The curves mirror the pattern of the energy levels in Fig. 3.5 and Fig. 3.6. For $U \gg \pi\Delta$ there is a well developed local-moment regime ($T\chi = \frac{1}{4}$), while for $U \sim \pi\Delta$ there is just the direct transition from the free orbital regime ($T\chi = \frac{1}{8}$) to the strong coupling regime ($\chi = \text{const.}$). The arrows indicate the effective Kondo temperature as also obtained within [9].

We now describe in detail the calculation of the *finite*-temperature spectral function

$$A_{d\sigma}(\omega) = -\frac{1}{\pi} \text{Im} G_{d\sigma}(\omega + i\delta^+) \quad (3.47)$$

with

$$G_{d\sigma}(z) = i \int_0^\infty dt e^{izt} \langle [d_\sigma(t), d_\sigma^\dagger]_+ \rangle, \quad (3.48)$$

as described in [53].

Due to the logarithmic discretization of the conduction band, the spectral function is given by a discrete set of δ -peaks. With the results of the iterative diagonalization one can compute the spectral function for each cluster of size N via

$$A_{d\sigma N}(\omega) = \frac{1}{Z_N} \sum_{mm'} |{}_N \langle m' | d_\sigma^\dagger | m \rangle_N|^2 \delta(\omega - (E_{m'}^N - E_m^N)) (e^{-\beta E_{m'}^N} + e^{-\beta E_m^N}), \quad (3.49)$$

with $\{|m\rangle_N\}$ and $\{|m'\rangle_N\}$ being sets of eigenstates of the Hamiltonian H_N with corresponding eigenenergies E_m^N and $E_{m'}^N$, and Z_N is the grand canonical partition function. A typical result for subsequent iterations N is shown in Fig. 3.8.

The question which arises is what information of which cluster is needed to calculate the spectral function for either zero or finite temperature. The iterative diagonalization yields the excitation spectrum $\omega_{mm'} = E_m^N - E_{m'}^N$ on a set of decreasing energy scales $\omega_0 > \omega_1 > \omega_2 > \dots$ (ω_N is the smallest energy scale of the Hamiltonian H_N with $\omega_N \sim D\Lambda^{-(N-1)/2}$). Excitations $\omega \gg \omega_N$ are already outside the energy range which is sampled by H_N , due to the truncation; they have to be extracted out of previous iterations $N' < N$. Similarly, excitations $\omega \ll \omega_N$ are not yet described by the cluster of size N ; they are accurately obtained by subsequent iterations with larger N .

For $T = 0$, the spectral density can therefore be calculated, using Eq. 3.49, according to

$$\begin{aligned} A_{d\sigma N}(\omega, T = 0) &= \frac{1}{Z_N(T = 0)} \sum_m |{}_N \langle m | d_\sigma^\dagger | 0 \rangle_N|^2 \delta(\omega + E_m^N) \\ &+ \frac{1}{Z_N(T = 0)} \sum_{m'} |{}_N \langle 0 | d_\sigma^\dagger | m' \rangle_N|^2 \delta(\omega - E_{m'}^N) \end{aligned} \quad (3.50)$$

This is done at an appropriate set of decreasing frequencies, which are typically chosen to be $\omega = 2\omega_N$.

At finite T , there are some modifications to this procedure. For a given temperature T , which is identified by $T_M \approx \omega_M$, one similarly evaluates the spectral function, using Eq. 3.49, at $\omega = 2\omega_N$ down to a minimum frequency corresponding to $\omega \approx T = T_M$. As shown in Figure 3.9, many more excitations contribute for finite- T calculations as compared to the $T = 0$ case.

When $\omega = 2\omega_N$ gets in the range of or smaller than the temperature of interest, $T = T_M$, excitations that are not contained in cluster N will start to contribute to the

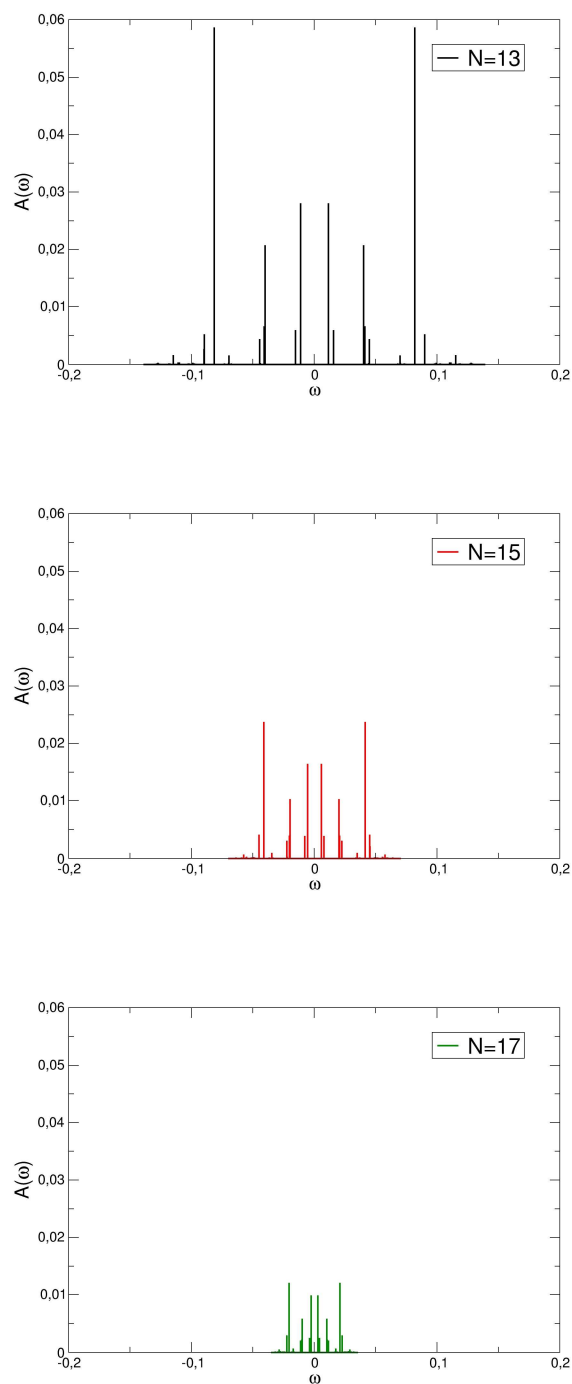


Figure 3.8: Spectral functions $A_N(\omega)$ for different cluster sizes $N=13, 15$ and 17 . The weight of the δ -peaks is given by their height.

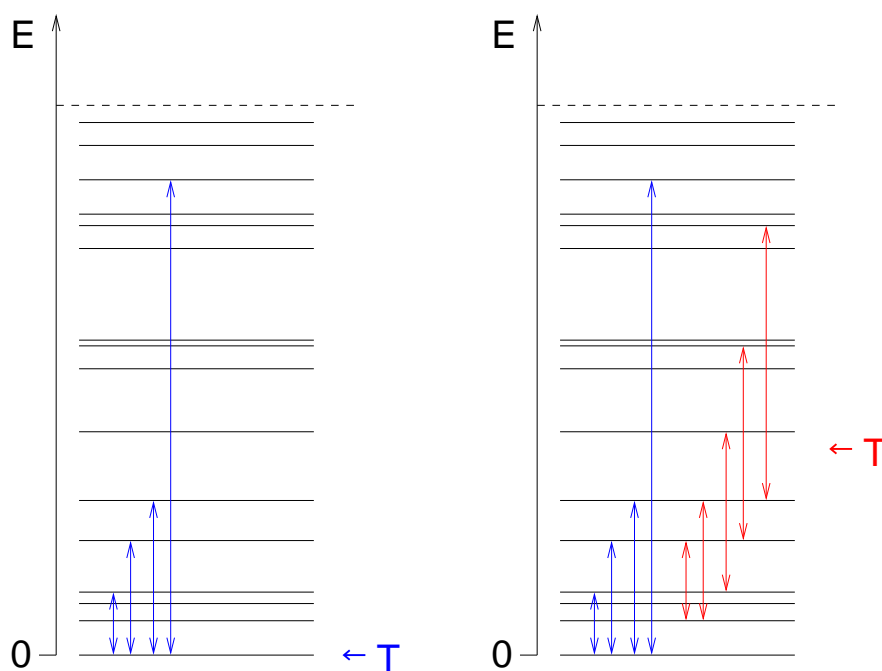


Figure 3.9: The spectrum of many-body excitations measured with respect to the ground state $E = 0$, up to the cutoff due to the truncation of states, as indicated by the dotted line. Some possible transitions, contributing to the spectral function, are shown as arrows. *Left plot:* For $T = 0$, only transitions starting from the ground state are possible. *Right plot:* For finite T , also transitions between excited states become possible.

spectral density. If one wants to calculate $A_d(\omega)$ at $\omega = 2\omega_N$ such that $|\omega| \leq T_M$ one has to use the cluster of size M corresponding to the temperature. The δ functions in the spectrum of cluster M are then broadened with functions of width T . This procedure recovers the known Fermi liquid relations for the transport quantities of the Anderson model [41, 43].

There exist several ways to combine the different discrete information of each cluster to arrive at continuous curves for the spectral function. The approach of [41, 43] is to replace the δ functions of Eq. 3.49 by appropriate broadening functions and then evaluating the spectral function at characteristic frequencies as described above. The program of this thesis uses an approach of [53], where, in a first step, the information of successive clusters N and $N + 2$ is combined and then, secondly, the spectra are broadened.

Starting point for combining the spectral information of two successive iterations (N and $N+2$ to avoid even-odd effects) is the set of δ peaks obtained for a cluster of size N , where there has been no truncation yet (see upper plot of Fig. 3.10). The spectral peaks for the next cluster of size $N + 2$ are shown below the peaks for cluster N . The minimal frequency appearing in cluster $N + 2$, ω_{min}^{N+2} , is roughly by a factor Λ smaller than the minimal frequency of cluster N , ω_{min}^N , while the maximum frequency ω_{max}^{N+2} is determined by the number of states retained after the truncation. The superposition of the δ peaks now happens such that the regions, where subsequent clusters do not overlap, thus in the interval $[\omega_{min}^{N+2}, \omega_{min}^N]$ and the region above ω_{max}^{N+2} , are equally kept for the combined set (as indicated by the broad arrows in Fig. 3.10). The region where the spectral information of cluster N and $N+2$ overlaps ($[\omega_{min}^N, \omega_{max}^{N+2}]$) is built using an appropriate weighting function, which, for simplicity, is a linear function. The peaks of the previous clusters are taken with a linear function with values from 0 to 1 for arguments between ω_{min}^N and ω_{max}^{N+2} , the peaks for the cluster of length $N + 2$ are taken with values from 1 to 0 (see Fig. 3.10).

The resulting set of δ peaks is then combined with the next cluster (of length $N+4$) and the procedure is iterated until the cluster of length M (defined by $T = T_M$) is reached.

Of course the resulting spectrum is still discrete, with δ peaks getting closer and closer as $\omega \rightarrow 0$. It is convenient for visualizing the distribution of spectral weight and for using the results in further calculations to broaden the peaks using appropriate broadening functions. In our program, this is done by Gaussians on a logarithmic scale with width b (typically between 0.3 and 0.6):

$$\delta(\omega - \omega_n) \longrightarrow \frac{e^{-b^2/4}}{b\omega_n\sqrt{\pi}} \exp\left[-\frac{(\ln \omega - \ln \omega_n)^2}{b^2}\right] \quad (3.51)$$

In Figure 3.11 we show the resulting local spectral function for the SIAM for different local level positions. A symmetric, spin-independent conduction band density of states $\rho(\omega) = 1/(2D)$ was assumed. In the particle-hole symmetric case ($\varepsilon_d = -U/2$), one nicely sees the different features of the impurity spectral function:

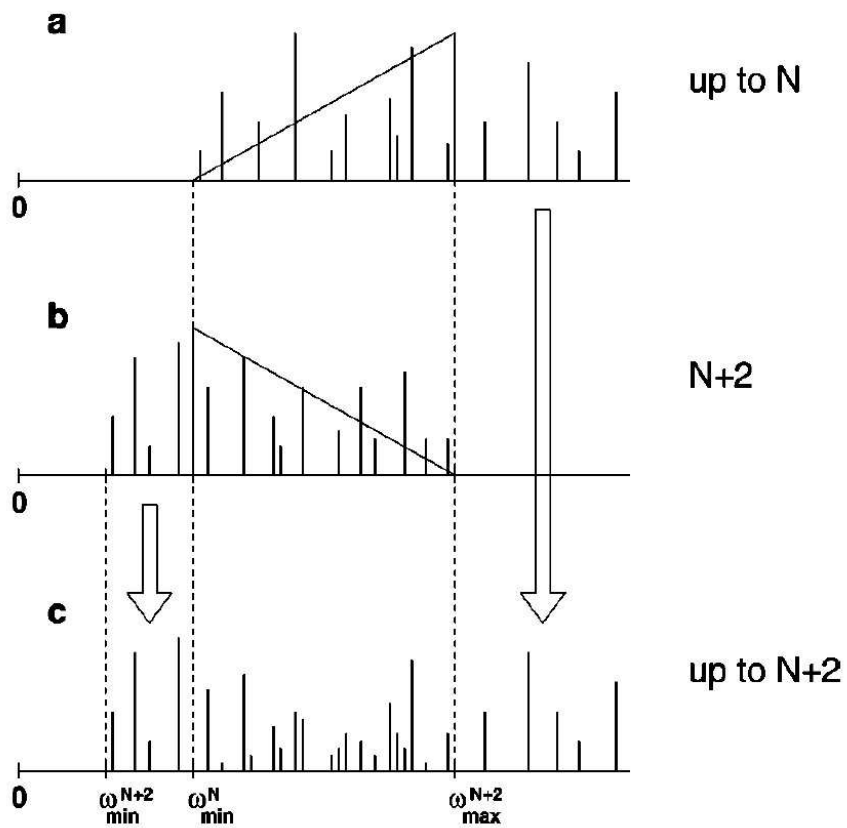


Figure 3.10: Superposition of the δ peaks in the spectral density up to length N [see (a)] with the peaks of the cluster of length $N + 2$. This procedure (described in the text) gives the spectral information contained in all clusters up to length $N + 2$ [see (c)]. Figure taken from [53].

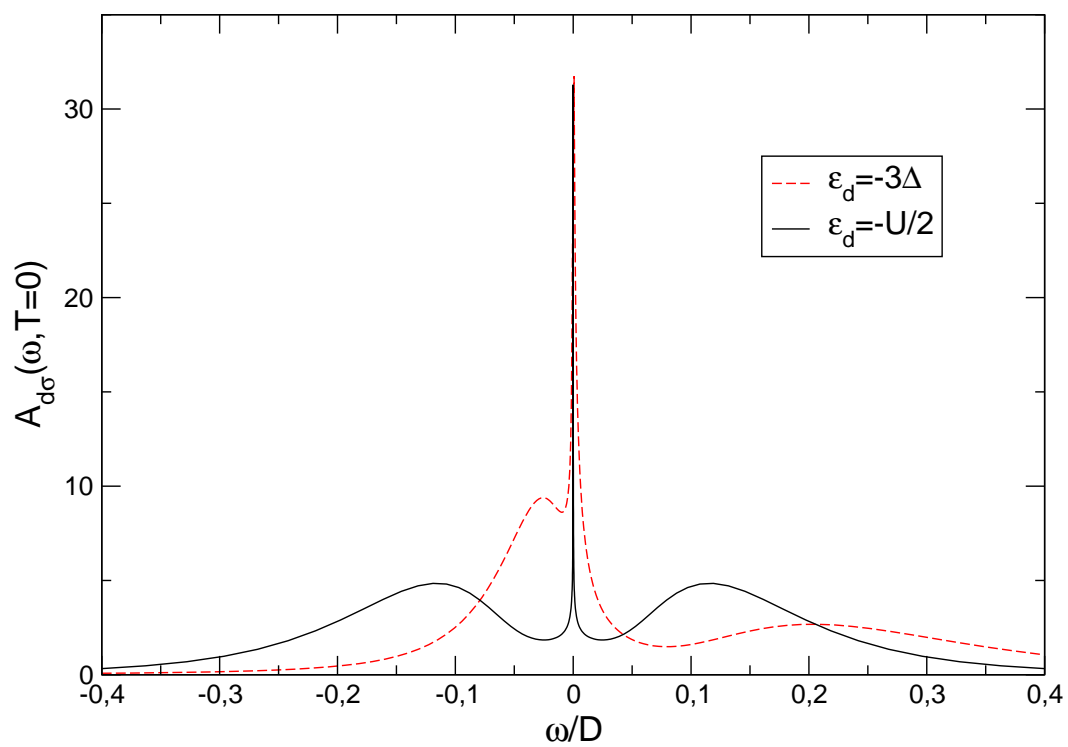


Figure 3.11: Zero temperature spectral function for the SIAM for different local level positions and $U/\pi\Delta = 6$. In each iteration, 1024 states were retained and we used a discretization of $\Lambda = 2$.

- Single particle excitations (“charge fluctuation peaks”) of width $\sim \Delta$ near ε_d and $\varepsilon_d + U$, corresponding to a singly and doubly occupied impurity, respectively.
- The sharp Kondo resonance of width $\sim T_K$ at the Fermi level, due to the spin fluctuations.

If one moves away from particle-hole symmetry (as shown for $\varepsilon_d = -3\Delta$ in Fig. 3.11), the spectral function is not symmetric anymore and the single particle excitations shift accordingly. The numerical accuracy of the $T = 0$ spectral densities obtained by the NRG can be checked by the Friedel sum rule, a Fermi-liquid relation which states that [54]

$$A_{d\sigma}(\omega = 0, T = 0) = \frac{1}{\pi\Delta} \sin^2(\pi n_d/2), \quad n_d = \int_{-\infty}^0 d\omega A_{d\sigma}(\omega, T = 0), \quad (3.52)$$

where n_d is the impurity occupation. The integrated spectral weight up to the Fermi level yields 0.985 for the particle-hole symmetric case in Fig. 3.11. Together with Eq. 3.52 this gives $A_{d\sigma}(0, 0) = 31.82$. The value extracted directly from Fig. 3.11 is $A_{d\sigma}(0, 0) = 31.29$, resulting in a 1.5% error. The error for the spectral density at the Fermi level remains small in the whole range of interaction strengths $0 \leq U \leq \infty$. The resolution of the high-frequency features is limited, as the NRG is designed to sample the low frequency behavior with high accuracy. The shape of the charge fluctuation peaks is strongly influenced by the broadening procedure. A modification in the calculation of the spectral function due to Bulla *et al.* [55], involving the Anderson model’s self-energy, turns out to yield more reliable and accurate results also for the high-frequency features.

A scaling analysis of the SIAM shows that the Kondo temperature T_K depends exponentially on the interaction strength U [1]:

$$k_B T_K \sim D \left(\frac{U\Delta}{|\varepsilon_d||\varepsilon_d + U|} \right)^{1/2} e^{-\frac{\pi|\varepsilon_d||\varepsilon_d + U|}{2U\Delta}}. \quad (3.53)$$

To illustrate this fact, the local spectral functions are shown in Figure 3.12 for the symmetric SIAM for different values of U . With increasing Coulomb repulsion, the Kondo temperature is decreased exponentially, as the inset of the Figure reveals.

The spectral density is the central starting point in order to make contact with experiments. The calculation of transport properties requires the knowledge of both frequency and temperature dependence of the spectral density. As done in [43], one can, for instance, calculate the resistivity $\rho(T)$ of conduction electrons scattering from a single Anderson impurity by $\rho(T)^{-1} = -e^2 \int_{-\infty}^{+\infty} \tau_{tr}(\omega, T) \frac{\partial f}{\partial \omega} d\omega$, where the transport time $\tau_{tr}(\omega, T)$ is related to the spectral density by $\tau_{tr}^{-1}(\omega, T) = \Delta A_{d\sigma}(\omega, T)$. Similar expressions hold for other transport coefficients (see [43]).

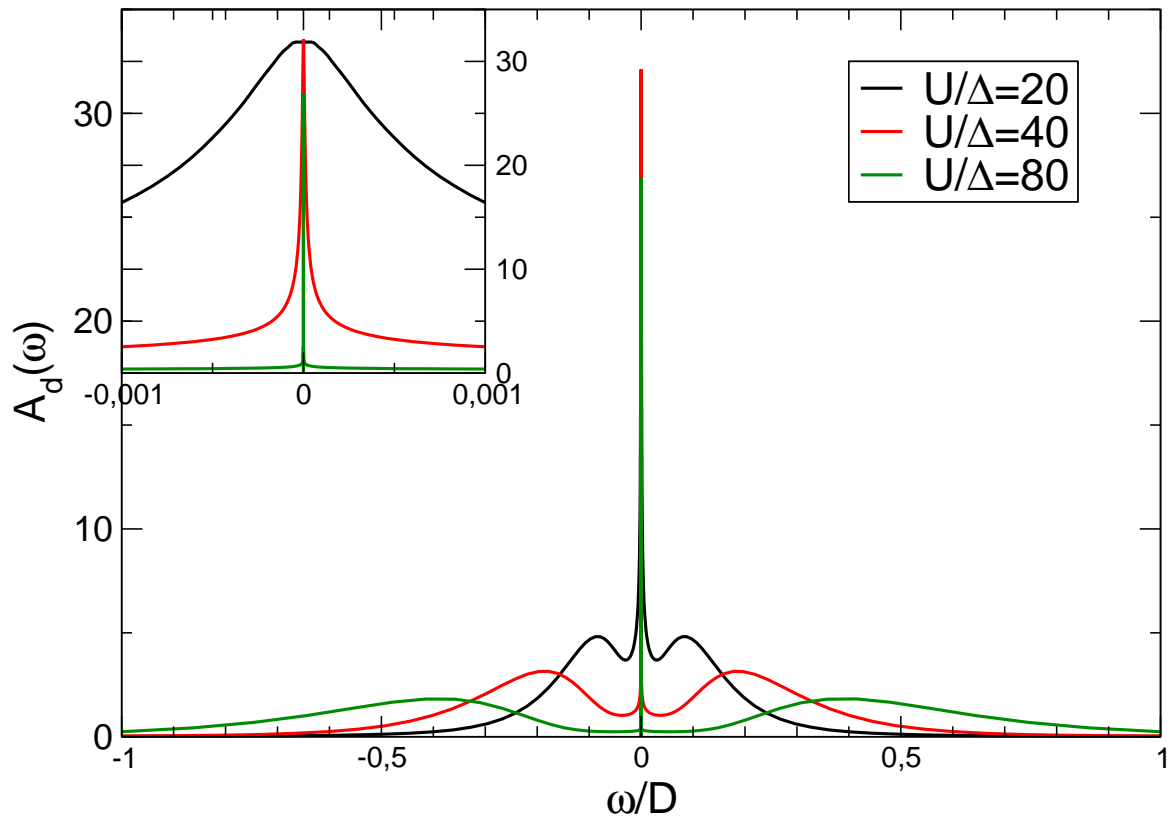


Figure 3.12: Local spectral function for the symmetric SIAM for different values of the Coulomb repulsion U . With increasing U , the width of the Kondo peak (as a measure for T_K) gets exponentially smaller. The inset shows the region around the Fermi level in more detail.

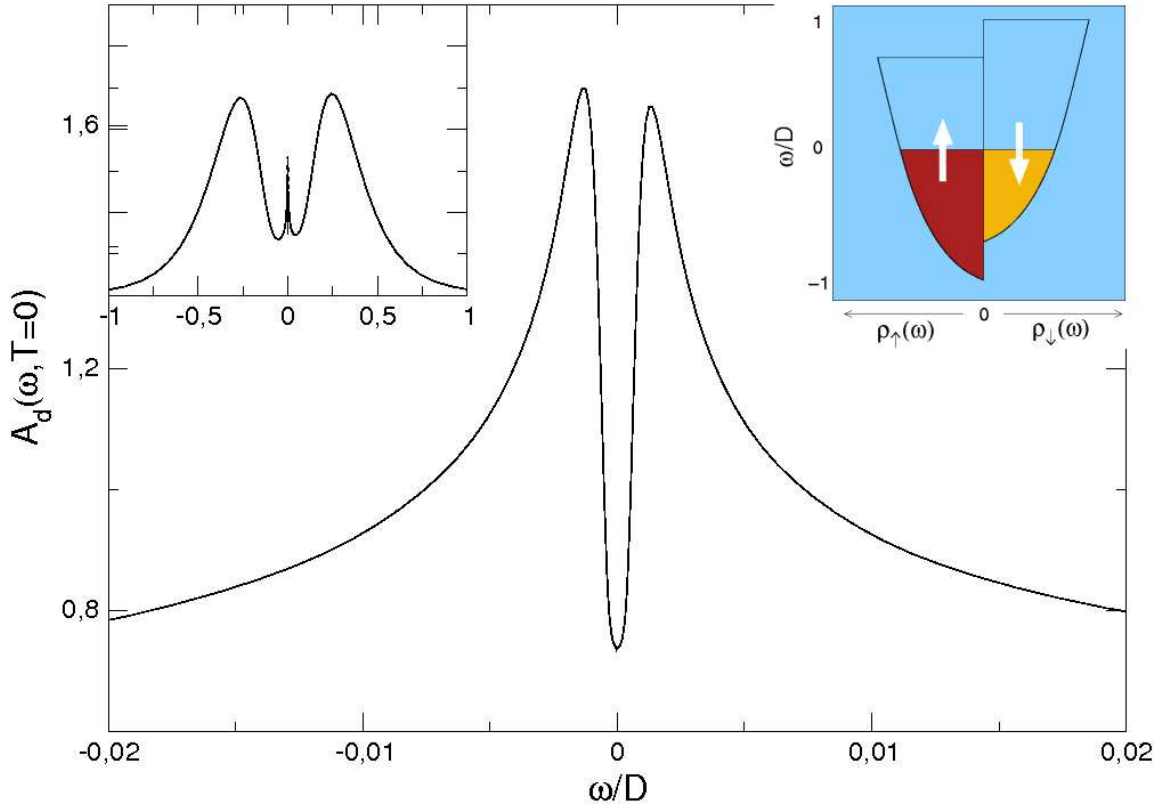


Figure 3.13: SIAM spectral function for a square-root shaped conduction electron DoS, including a Stoner splitting (see right inset). While the general structure of two charge fluctuation peaks and the Kondo resonance is maintained (left inset), the Kondo resonance at the Fermi level is spin-split.

Spectral densities for arbitrary conduction electron DoS, inclusion of a magnetic field

As already stated, the NRG, developed for this thesis, is capable of dealing with an arbitrary conduction electron density of states, which corresponds to a frequency-dependent hybridization function $\Delta_\sigma(\omega)$. The difference to the standard Wilson NRG is the iterative calculation of the Wilson chain parameters $\varepsilon_{n\sigma}$ and $t_{n\sigma}$ with arbitrary precision, as described in detail in appendix A. A structured hybridization function will become important in the context of dynamical mean-field theory (DMFT), which will be described during the following sections.

An example of the calculation of the SIAM impurity spectral function for a spin- and energy-dependent conduction electron DoS is given in Fig. 3.13. Similar to the work of Martinek *et al.* [56] we calculated the SIAM spectral function for a square-root shape DoS equivalent to a parabolic band (as for free electrons) with a Stoner splitting, as illustrated in the right inset of Fig. 3.13.

The resulting spectral function exhibits the usual three peak structure (2 charge fluctuation peaks and the Kondo resonance), but a zoom picture around the Fermi energy reveals that the Kondo peak is now spin-split.

The effects of a spin-split conduction band and thus a splitting of the Kondo resonance in the spectral density are similar to the ones observed when one includes a local magnetic field B at the impurity site. The usual Anderson Hamiltonian acquires an additional term $-g\mu_B BS^z$ in the impurity part \mathcal{H}_d , where μ_B is the Bohr magneton, g the gyro-magnetic ratio (usually set $g = 2$) and S^z the z -component of the total spin. As was outlined in [57], the inclusion of the additional energy scale $\omega_{mag} \sim g\mu_B B$ causes problems in the calculation of the spectral function. As the magnetic field with characteristic energy ω_{mag} affects the spectral function $A_d(\omega, T)$ on *all* frequencies ω , one has to distinguish carefully between the influence of the scales ω and ω_{mag} . The so-called 'DM-NRG', invented by Hofstetter [57], improves the calculation of the spectral function, especially in the high-energy regime. However, the traditional NRG implemented for this thesis can still show the impact of a local magnetic field on the spectral function. In Fig. 3.14 the spectral functions for different values of a local magnetic field B clearly show the Zeeman splitting of the Kondo resonance.

3.3 Extensions

The NRG, as it is described so far in this thesis, has proven to be a powerful method for the investigation of quantum impurity models. It gives information on the complete many-body spectrum of the Kondo model and the single impurity Anderson model on all energy scales. Static and dynamic properties can be calculated and through computation of transport properties, direct comparison with experiments becomes possible.

There is nevertheless room for further extensions of the NRG method. The study of multi-channel models with the NRG allows to investigate the large field of non-Fermi liquid physics. We will consider aspects of the two-channel Kondo effect, as computed by an extended NRG, in chapter 4.

Originally designed for quantum impurities coupling to a fermionic system, the NRG was adapted by Bulla *et al.* [58] to work also for the interaction with a bosonic bath.

For the investigation of the non-equilibrium transport through correlated impurity systems such as quantum dots, the NRG was extended quite recently by Anders and Schiller [59, 60], triggered through earlier ideas of Costi [61]. This will be described in the next section.

3.3.1 Non-equilibrium

Away from equilibrium, the absence of a groundstate requires new criteria how to select the states which have to be truncated after each NRG iteration. The philosophy of

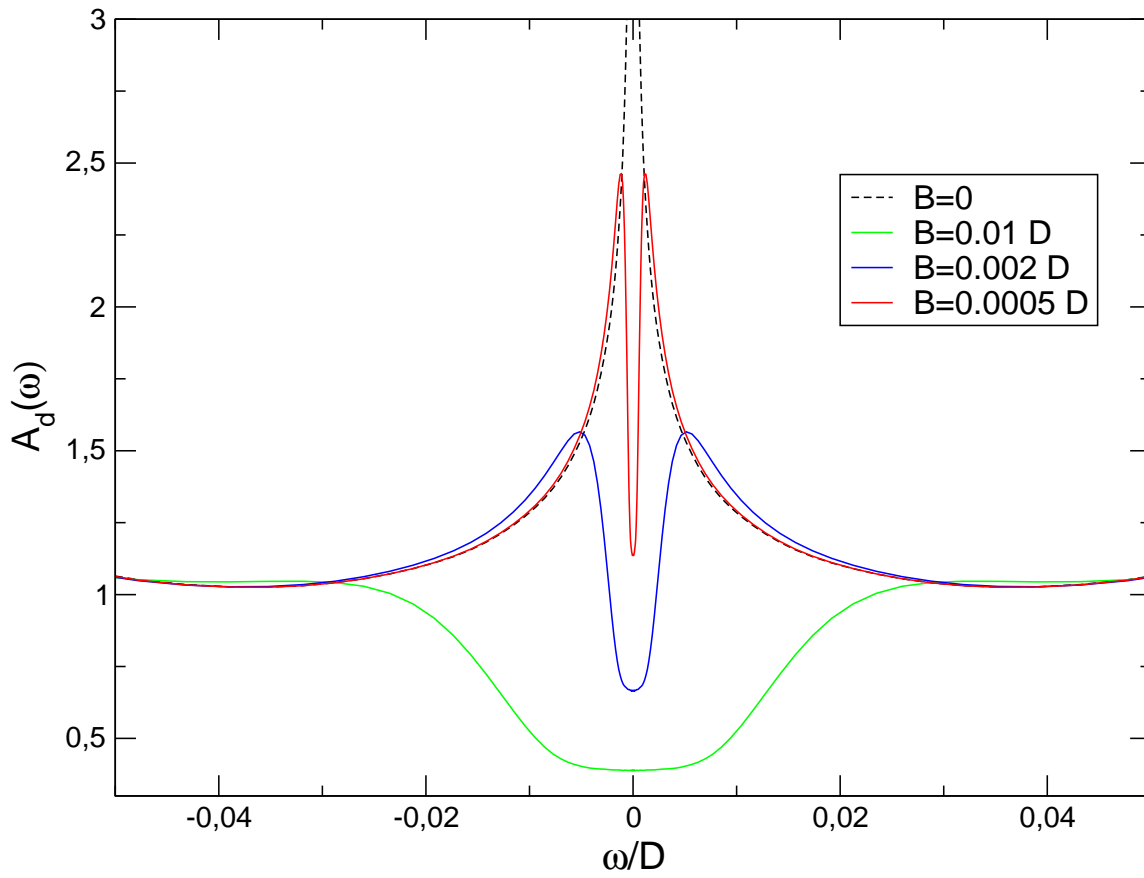


Figure 3.14: Local spectral function for the symmetric SIAM with a local magnetic field B . The Kondo resonance shows the Zeeman splitting with the Zeeman energy $\omega_{mag} \sim g\mu_B B$.

the novel approach due to Anders and Schiller [59, 60] is now to 'put the RG upside down' and let all discarded states contribute to the calculations and thus to change the truncation scheme rigorously [62]. The newly developed time-dependent NRG (TD-NRG) is capable of describing the dynamics on short and long time scales and works for all temperatures.

As usual the conduction band is mapped onto the semi-infinite Wilson chain (see Figure 3.15).

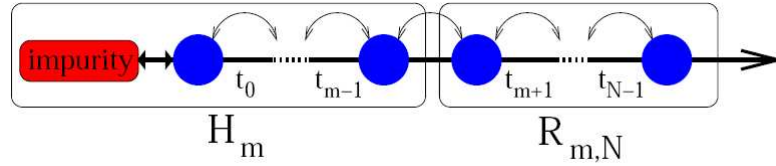


Figure 3.15: As usual in the NRG, also in the TD-NRG there is an exact mapping onto a semi-infinite chain (figure taken from [62]).

The main modification in the TD-NRG in contrast to the standard equilibrium NRG is now to take a set of all discarded states plus “environment” e to form a complete basis set of the NRG chain: $\{|l, e; m\rangle\}$. All discarded states contain information on the non-equilibrium dynamics. The real-time dynamics of an arbitrary local operator \hat{O} can now be computed as

$$\langle \hat{O} \rangle(t) = \sum_m \sum_{l, l' \text{ truncated}} \langle l | \hat{O} | l \rangle e^{i(E_l - E_{l'})t} \rho_{ll'}^{\text{red}}(m) \quad (3.54)$$

with the reduced density matrix $\rho_{ll'}^{\text{red}}(m)$, similar to the one used in the DMRG approach (see section 2.1.2). Starting from the initial ($t = 0$) density matrix $\hat{\rho}_0$, one traces out the “environment” e :

$$\rho_{ll'}^{\text{red}}(m) = \sum_e \langle l, e; m | \hat{\rho}_0 | l', e; m \rangle. \quad (3.55)$$

Thus all states and energy scales contribute and in this sense there is no truncation of states. Another advantage of the TD-NRG is that there is no accumulated error in time and that it is valid for all temperatures. For further details on the TD-NRG and its applications to the Spin-Bose model or the Kondo model we refer to the original papers [59, 60].

3.4 Dynamical mean-field theory with the NRG

The dynamical mean-field theory (DMFT) [63] has become a very powerful tool for the investigation of lattice models of correlated electrons since the first investigation of the Hubbard model in the limit of infinite dimensions by Metzner and Vollhardt [64]. The combination of the DMFT approach with ab-initio methods led to significant progress for a realistic description of strongly correlated materials (a brief overview can be found in [65]).

In DMFT the lattice model is mapped on an effective quantum impurity model in a bath which has to be determined self-consistently [66]. The impurity model is a single-impurity Anderson model with an energy-dependent hybridization function $\Delta_\sigma(\omega)$. Thus the NRG program developed for this thesis can serve as a reliable 'impurity solver' in DMFT calculations [53, 55].

In the last section of this chapter we want to describe how we plan to use our NRG program to contribute to the explanation of the simultaneous para-to-ferromagnetic and semiconductor to metal transition in oxygen-depleted europium oxide. The approach followed there is quite similar to the DMFT, as although the starting point is not a lattice model, a quantum impurity model is solved in a self-consistency loop.

3.4.1 A model for europium oxide (EuO)

At room temperature, europium oxide (EuO) is a paramagnetic semiconductor with a wide band gap of 1.2 eV. Below a critical temperature $T_c = 69K$, it becomes a ferromagnetic metal, where the polarization of the charge carriers is found to be nearly 100 per cent (for details, see [67] and references therein).

There was already work done by our group in order to find a microscopic model describing the nature and the simultaneity of the magnetic and the metallic transition for oxygen depleted EuO [67]. There an extended Hubbard-Anderson model with a correlated band is set up, treating the correlations within a mean-field (Hartree-Fock) approximation. The spin-dependent spectral densities of the conduction electrons are calculated using the Non-Crossing Approximation (NCA). But as already mentioned in section 2.2, the NCA is not able to describe the spectral function correctly in the presence of a local magnetic field, producing a spurious resonance at the Fermi level. We believe that the application of the NRG can provide valuable progress in the analysis of our microscopic model.

Starting with a suitable, spin- and energy dependent conduction electron DoS $\rho_{c\sigma}(\omega)$, we calculate the spin-resolved impurity spectral function $A_{d\sigma}(\omega)$ using the NRG, as already described in the previous sections. Through a Kramers-Kronig transformation one can then get the full impurity propagator $G_{d\sigma}(\omega)$. The conduction electron self-energy $\Sigma_{c\sigma}(\omega)$, consisting of the Stoner and the impurity scattering contributions, can be computed via

$$\Sigma_{c\sigma}(\omega) = U\langle\hat{n}_{c-\sigma}\rangle + n_{imp}|V|^2G_{d\sigma}(\omega), \quad (3.56)$$

where the first term is the Stoner term with the conduction electron number operator and n_{imp} is the oxygen defect concentration.

Subsequently the retarded conduction electron propagator is obtained by

$$G_{c\sigma}(\omega) = [\omega + \mu - \varepsilon_k + i0 - \Sigma_{c\sigma}(\omega)]^{-1}, \quad (3.57)$$

where μ is the common chemical potential of defect electrons and conduction band electrons.

Through integration, one gains a new spin-dependent spectral function $\rho_{c\sigma}(\omega) = -\int \frac{d\omega}{\pi} \text{Im} G_{c\sigma}(\omega)$, which serves as the input for the next iteration of this self-consistent loop. The calculations are continued until the convergence of the conduction electron spectral functions.

Chapter 4

Multi-channel models

Nozières and Blandin [68] showed that an anomalous fixed point occurs in the multi-channel Kondo problem at finite coupling for $M > 2S_I$, where M is the number of channels and S_I the impurity spin. It corresponds to a situation where the conduction electron spins overcompensate the local moment of the impurity and thus the over-screened ground state of this system is not a ($S = 0$) singlet anymore, as in the ordinary one-channel Kondo (1CK) model. In the overcompensated regime non-Fermi liquid physics arises, providing possible explanations for the description of real materials. An overview over the various multi-channel Kondo impurity model candidates most extensively studied, specifically the two-level system (TLS) Kondo model, was given by Cox and Zawadowski [50].

In this chapter we first consider the two-channel Kondo (2CK) impurity model, for which Cragg *et al.* showed by renormalization group calculations that the ground state is not a state of spin zero in general [69]. For the isotropic 2CK model, a stable non-Fermi liquid fixed point occurs for intermediate values of the Kondo coupling J . The results for the isotropic as well as the channel anisotropic model, first found by Pang and Cox [70], are reproduced with the program set up for this thesis. Explicitly we then investigate the distribution $P(T_K)$ of the Kondo temperature T_K in the 2CK system as an explanation for the measurements on quantum point contacts.

4.1 Two-channel Kondo effect (2CK)

4.1.1 Motivation

In the 2CK effect, a two-fold degenerate system such as a local spin (a Kondo impurity) is antiferromagnetically coupled to two independent electron reservoirs. Since the reservoirs are not coupled to each other and do not communicate, each one attempts to screen the local impurity spin, leading to overall overscreening. Thus the ground state is no spin zero singlet and has residual entropy even at zero temperature. A 2CK system cannot be described by Fermi liquid theory [71] anymore, it exhibits low-energy

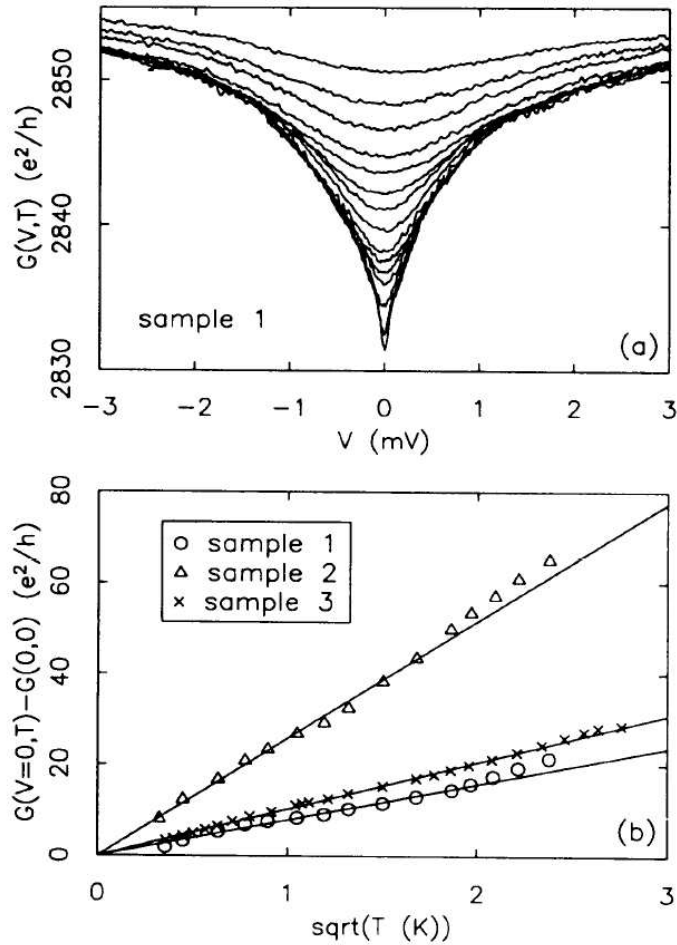


Figure 4.1: Conductance for a metal nano-constriction, showing the zero-bias (square-root) anomaly (taken from [76]).

non-Fermi liquid behavior [50, 27, 28, 72].

The interest in the 2CK model is due to a number of suggestions for experimental realizations of the 2CK overcompensated behavior. Oreg and Goldhaber-Gordon [73] used a modified single-electron transistor with two spatially separated sets of confined electrons to study the 2CK effect at experimentally accessible temperatures. Cox demonstrated 2CK behavior in the quadrupolar Kondo effect in heavy fermion compounds [74]. Ralph *et al.* reported observation of the 2CK effect in metal nanoconstrictions [75, 76, 77], where two-level tunneling systems (TLS) in a disordered metal provide the local (near-)degeneracies instead of the traditional spin. In Ralph's experiments, zero-bias conductance measurements on the quantum point contacts show an anomalous square-root dependence on the temperature (see Fig. 4.1). The measurements are consistent with the presence of 2CK impurities and are difficult to explain

by any other known microscopic mechanism. Arguments that contributions through the quantum interference between Coulomb interaction and scattering off defects in a nanojunction would lead to the same ($\propto \sqrt{T}$) scaling behavior could be invalidated by [78].

A microscopic, theoretical explanation of the 2CK effect is far from being complete. Two works, developed in our group [79], can possibly make an important step towards a better understanding in that issue. Still, as one of the unresolved problems within the 2CK scenario, the experimental results indicate a very narrow distribution $P(T_K)$ of the Kondo temperature T_K . For a nanoscopic point contact one expects the Kondo defects to be statistically generated, and consequently a wide distribution of the Kondo coupling constant J . Thus it a priori unclear why a sharp distribution of T_K is measured.

We investigate the distribution of $P(T_K)$ by means of explicit NRG calculations, described in the following section.

4.1.2 Solution with the NRG

It was known since Nozières and Blandin [68] that a non-trivial fixed point occurs for the isotropic 2CK model (the Kondo coupling strength J is equal for both conduction electron channels) for an intermediate, finite value of J . Since perturbative methods like perturbative RG are only able to deal with small values of the bare coupling, one has to use a non-perturbative way to cover the full range of initial values of J . The original (non-perturbative) NRG work confirming the non-trivial fixed point was performed by Cragg *et al.* [69], while subsequent calculations by Pang and Cox [70] and Affleck *et al.* [80] explored the weak coupling approach to the transition and the influence of exchange anisotropy, applied local and bulk spin fields as well as channel fields in greater detail. To validate our 2CK NRG program we first recalculated the results of Pang and Cox [70].

Hamiltonian

The 2CK Hamiltonian is

$$\frac{H_{2CK}}{D} = \sum_{k\alpha\sigma} \varepsilon_k c_{k\alpha\sigma}^\dagger c_{k\alpha\sigma} + \frac{1}{2} \sum_{\alpha} J_{\alpha} c_{0\alpha\sigma}^\dagger \vec{\sigma}_{\sigma\sigma'} c_{0\alpha\sigma'} \cdot \vec{s}_I \quad (4.1)$$

where D is the conduction bandwidth, $\alpha = \pm$ the channel index, $\sigma = \uparrow, \downarrow$ is the spin index, $c_{k\alpha\sigma}^\dagger$ are the usual electron creation operators, $c_{0\alpha\sigma}^\dagger$ the local Wannier state at the impurity site, $c_{0\alpha\sigma}^\dagger \vec{\sigma}_{\sigma\sigma'} c_{0\alpha\sigma'}$ the conduction electron spin-density at the impurity site and $s_I = \frac{1}{2}$ the impurity spin.

As common to the NRG solutions, the Hamiltonian (4.1) is logarithmically discretized. The conduction electron part is mapped onto the semi-infinite Wilson chain (now there are 2 independent semi-infinite chains) where the Wilson shell states correspond to creation operators $f_{0\alpha\sigma}^\dagger, f_{1\alpha\sigma}^\dagger, \dots$ having radial extent $\Lambda^{1/2}, \Lambda^{3/2}, \dots$ times

k_{Fermi}^{-1} about the impurity. Finally the discretized 2CK Hamiltonian takes the form

$$H/D = \sum_{n=0, \alpha, \sigma}^{\infty} t_n \left(f_{n\alpha\sigma}^{\dagger} f_{n+1\alpha\sigma} + h.c. \right) + \sum_{\alpha} J_{\alpha} f_{0\alpha\sigma}^{\dagger} \vec{\sigma}_{\sigma\sigma'} f_{0\alpha\sigma'} \cdot \vec{s}_I \quad (4.2)$$

with $t_n = \frac{\Lambda^{-n/2}(1+\Lambda^{-1})(1-\Lambda^{2n+1})}{2[(1-\Lambda^{2n+1})(1-\Lambda^{2n+3})]^{1/2}}$.

When $J_+ = J_-$ one has the isotropic 2CK Hamiltonian, while $J_+ \neq J_-$ corresponds to the channel asymmetric case. Hamiltonian (4.2) can be viewed as a series of Hamiltonians $H_N (N \geq 0)$ which approaches H in the limit $H \rightarrow \infty$:

$$H = \lim_{N \rightarrow \infty} \Lambda^{-(N-1)/2} H_N \quad (4.3)$$

with

$$H_N = \Lambda^{(N-1)/2} \left[\sum_{n=0, \alpha, \sigma}^{N-1} t_n \left(f_{n\alpha\sigma}^{\dagger} f_{n+1\alpha\sigma} + h.c. \right) + \sum_{\alpha} J_{\alpha} f_{0\alpha\sigma}^{\dagger} \vec{\sigma}_{\sigma\sigma'} f_{0\alpha\sigma'} \cdot \vec{s}_I \right] \quad (4.4)$$

H_0 corresponds to a Kondo impurity, coupled to the first site of the Wilson chain:

$$H_0 = \frac{2}{\sqrt{\Lambda}} \sum_{\alpha} J_{\alpha} \left[\frac{1}{2} (S_{\alpha}^{+} S_I^{-} + S_{\alpha}^{-} S_I^{+}) + S_{\alpha}^z S_I^z \right] \quad (4.5)$$

($S_{\alpha}^{+}/S_{\alpha}^{-}$ is the usual raising/lowering operator in channel α .)

The RG transformation reads ($\hat{=}$ two successive Hamiltonians are related by)

$$H_{N+1} = \sqrt{\Lambda} H_N + \Lambda^{N/2} \sum_{\alpha\sigma} t_N \left(f_{N\alpha\sigma}^{\dagger} f_{N+1\alpha\sigma} + h.c. \right) \quad (4.6)$$

As one adds a site in the Wilson chain, the Hamiltonian grows exponentially as 16^N , thus besides a proper truncation scheme the use of symmetries is essential for the numerical solution of the problem.

Symmetries

The M -channel Kondo spin- $\frac{1}{2}$ model has a full symmetry group of $SU(2)_{spin} \times Sp(M)$, where $Sp(M)$ is the so-called symplectic group [80]. In the two-channel case ($M = 2$), the only invariant subgroups of $Sp(2)$ (which is isomorphic to $SO(5)$) are $SU(2) \times U(1)$ which corresponds to the choice of channel spin and charge symmetries, and $SU(2) \times SU(2)$ which corresponds to the separate ‘‘axial charge’’ symmetries [50] (see below). As our standard NRG program for the 1CK model and SIAM already uses charge Q and z -component of the total spin S_{tot}^z as labels for the many particle states, we choose the channel spin and charge symmetries for our 2CK program. In the presence of channel symmetry breaking fields the full $SU(2)$ channel spin symmetry

is broken down to a $U(1)$ symmetry with the z -component S_{ch}^z of the channel spin as the conserved charge. Accordingly, our program uses a $U(1) \times U(1) \times U(1)$ symmetry, which is (charge) \times (spin) \times (channel spin) and yields the following quantumnumbers:

$$\hat{Q} = \sum_{n,\sigma,\alpha} \left[f_{n\alpha\sigma}^\dagger f_{n\alpha\sigma} - \frac{1}{2} \right] \quad (4.7)$$

$$\hat{S}_{tot}^z = \sum_{n=0,\sigma,\alpha} \sigma f_{n\alpha\sigma}^\dagger f_{n\alpha\sigma} + S_I^z \quad (4.8)$$

$$\hat{S}_{ch}^z = \frac{1}{2} \sum_{n,\alpha,\sigma} \alpha f_{n\alpha\sigma}^\dagger f_{n\alpha\sigma} \quad (4.9)$$

The Hamiltonians are diagonalized in each irreducible subspace $|Q, S_{tot}^z, S_{ch}^z\rangle$ and about 900 states are retained at each NRG iteration. Details on the iterative diagonalization can be found in appendix B.

An alternative way of dealing with the charge and channel degrees of freedom of the conduction electrons was first found by [81, 82, 83]. It was observed that the single-channel particle-hole symmetric Kondo model enjoys an additional global $SU(2)$ -symmetry specified by the ‘‘axial charge’’ generators

$$\begin{aligned} j_\alpha^+ &= \sum_n (-1)^n c_{n,\uparrow,\alpha}^\dagger c_{n,\downarrow,\alpha}^\dagger \\ j_\alpha^- &= \sum_n (-1)^n c_{n,\downarrow,\alpha} c_{n,\uparrow,\alpha} \\ j_\alpha^z &= \frac{1}{2} \sum_{n,\alpha} \left[c_{n,\uparrow,\alpha}^\dagger c_{n,\uparrow,\alpha} - c_{n,\downarrow,\alpha}^\dagger c_{n,\downarrow,\alpha} \right] \end{aligned}$$

The corresponding quantum numbers total axial charge j_α^2 and j_α^z may still be used in the presence of channel symmetry breaking fields. The ‘‘axial charge symmetry’’ or ‘‘isospin’’ symmetry was also used in the first NRG calculations of the 2CK model in [70]. More detailed considerations on the symmetries in the multi-channel Kondo problem can be found in [80].

Reproduced results

First, we considered the isotropic, strong-coupling limit to recover its non-Fermi liquid fixed point. Fig. (4.2) shows the lowest energy levels for $J_+ = J_- = 1.0$, $\Lambda = 3.0$. The eigenvalues of H_N (in units of the conduction bandwidth D) for sequential N are connected by a line in order to watch the energy level flow. One realizes that the fixed point is reached already after a few iterations, which tells us that the initial coupling

is only slightly different from its renormalized fixed-point value. Also there is no even-odd effect in the 2CK spectrum (the fixed point values are equal for the left and the right side of the plot). The results of Fig. (4.2) are in good agreement with Fig. 1 of [70], who used their results to compare it with the initial 2CK NRG work of Cragg *et al.* [69].

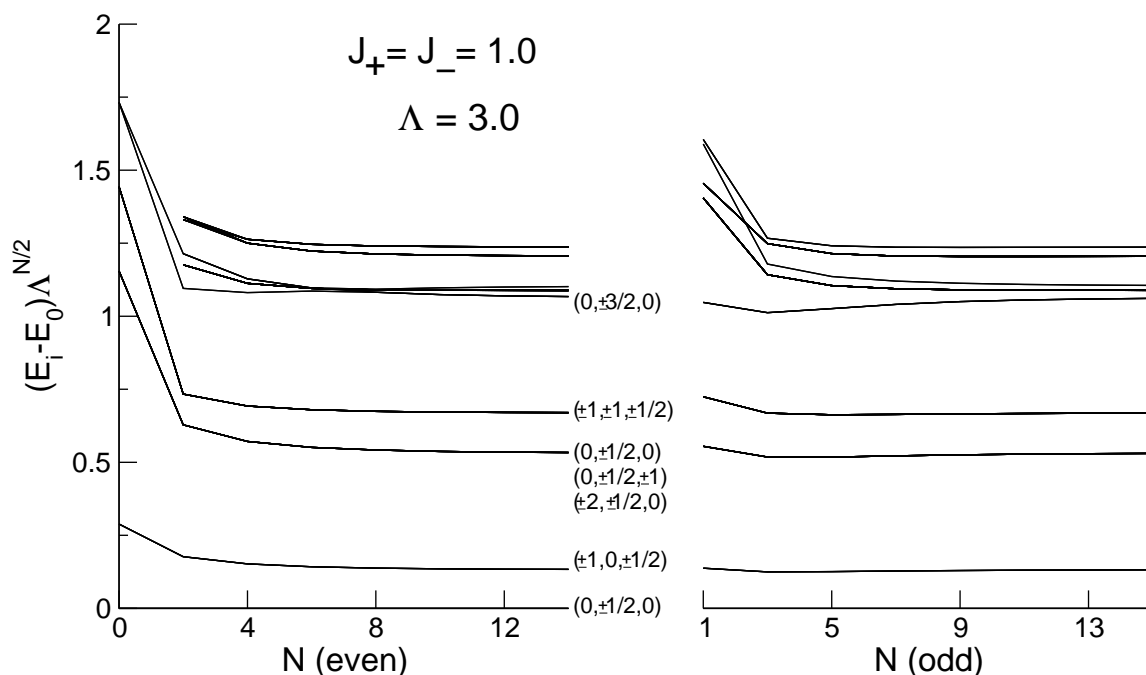


Figure 4.2: Lowest NRG energy levels for the strong-coupling isotropic 2CK Hamiltonian. The states are labeled by (Q, S_{tot}^z, S_{ch}^z) . Compare to Fig. 1 of [70].

The results for initial weak-coupling ($J_+ = J_- = 0.2$) are shown in Fig. 4.3. Quick convergence is ensured through $\Lambda = 9.0$. Since the initial J is small, it takes more NRG iterations to reach the fixed point as compared to an initial coupling of $J_+ = J_- = 1.0$. However, the spectra flow to a fixed structure independent of the original coupling value. Again, after the energy levels have converged, there is no even-odd effect. Fig. 4.3 confirms in a non-perturbative way that the 2CK model has a non-trivial fixed point which is stable in the absence of fields which break the full $SU(2)$ invariance of the exchange coupling [50]. We will use the crossover scale at which the low lying levels flow to the non-trivial fixed point as a measure for the Kondo temperature T_K .

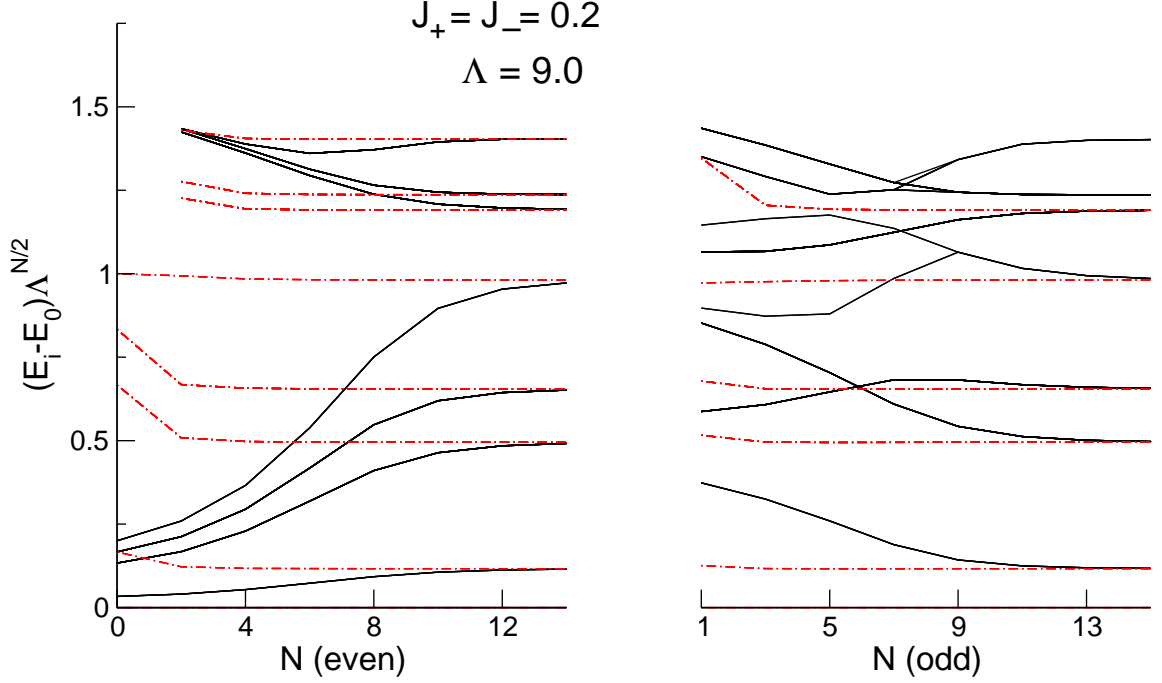


Figure 4.3: Lowest NRG energy levels for the weak-coupling isotropic 2CK Hamiltonian. The dashed-dot lines represent the energy levels for $J_+ = J_- = 1.0$ with the same $\Lambda = 9.0$. Compare to Fig. 2 of [70].

A major difference in comparison with the 1CK calculations is that the spectra of the 2CK model have a non-uniform spacing. While this is no rigorous proof, it is a consequence of the non-Fermi liquid character of the 2CK excitation spectrum. One way to verify that is by noting that the quantum numbers of the free states cannot be that of a Fermi liquid (further discussion can also be found in [50]). Another way of proving that the resulting spectra are non-Fermi liquid 2CK spectra is calculating the entropy, which has to be $S_{2CK} = \frac{1}{2} \log 2$ as $T \rightarrow 0$. But since there is a nearly 1 : 1 - agreement of our results with the results of Pang and Cox [70] we omit a more detailed analysis here. The reason for the difference of our fixed point energy values from the values of Pang and Cox is a factor of $(\frac{1}{2}(1 + \Lambda^{-1}))^{-1}$ which arises from different definitions of the rescaled Hamiltonian H_N . Note that e. g. in the original work for the SIAM of Krishna-murthy *et al.* [9] the system parameters are rescaled by a factor of $(\frac{2}{1+\Lambda^{-1}})$ in their N^{th} step Hamiltonian H_N (their Eq. (2.18ff)).

It is known from [68, 69] and the scaling analysis in [50] that the non-trivial 2CK fixed point is unstable if one breaks the channel $SU(2)$ symmetry, thus $J_+ \neq J_-$. The more strongly coupled channel will provide the ordinary Kondo effect (the corresponding coupling flows to $J = \infty$), while the weakly coupled channel produces a free Fermi gas ($J \rightarrow 0.0$).

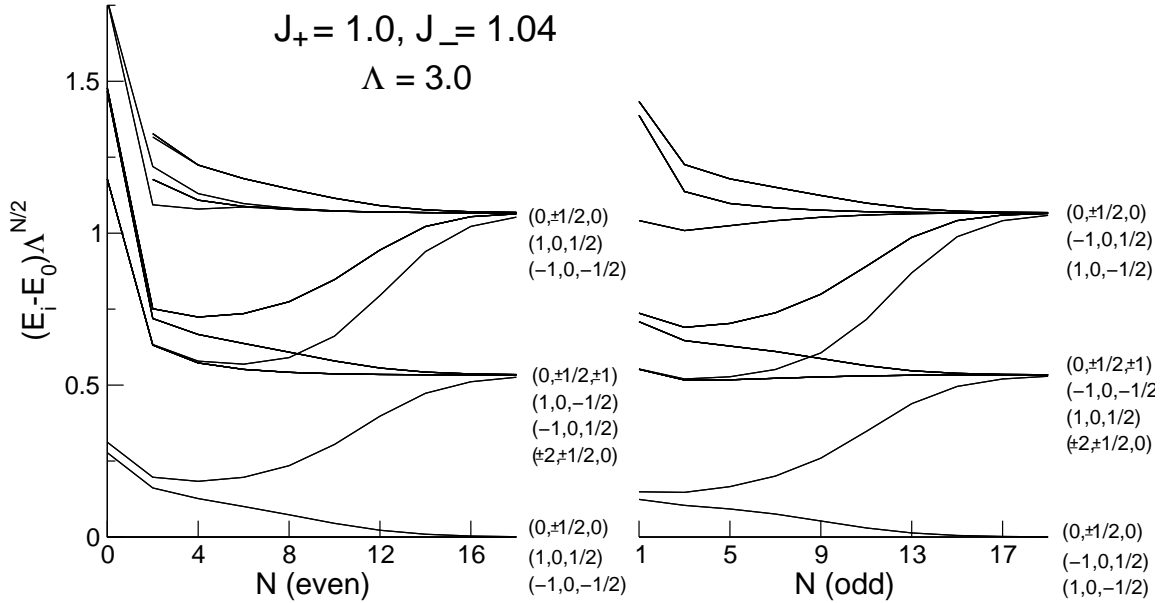


Figure 4.4: Lowest NRG energy levels for the strong-coupling channel-anisotropic 2CK Hamiltonian. Lifting the channel degeneracy produces a flow to a normal Kondo fixed point. States are labeled by (Q, S_{tot}^z, S_{ch}^z) . Compare to Fig. 6 of [70]

Fig. 4.4 confirms these results for a channel anisotropic situation. Since our program incorporates the $U(1)$ symmetry (by the quantum number S_{ch}^z) which is left after breaking the full $SU(2)$ channel symmetry, we are able to analyze the situation where $J_+ \neq J_-$. The spectrum flows to an ordinary Kondo fixed point with uniform level spacing, as anticipated by Fermi liquid theory. Note that there is a difference in the labels of the many-particle states in Fig. 4.4.

4.1.3 Results and discussion

We can now turn to the analysis of the distribution of T_K in the isotropic 2CK model. Therefore we examine the crossover scale at which the energy levels flow to the non-Fermi liquid fixed point which we use as a measure for the Kondo temperature T_K . This is done for a whole range of initial couplings J for different NRG discretization parameters Λ .

For every energy flow diagram one has to ensure that one really reaches the non-Fermi liquid fixed point and that for a fixed NRG discretization parameter Λ the same fixed point energy levels are obtained, independent of the initial coupling strength J . Our 2CK NRG program uses Fortran BLAS routines (Basic Linear Algebra Subroutines) for the matrix diagonalization. These are accurate to the desired precision, which in our case is double precision ($2^{-52} \approx 10^{-16}$), since we store the eigenvalues and eigen-

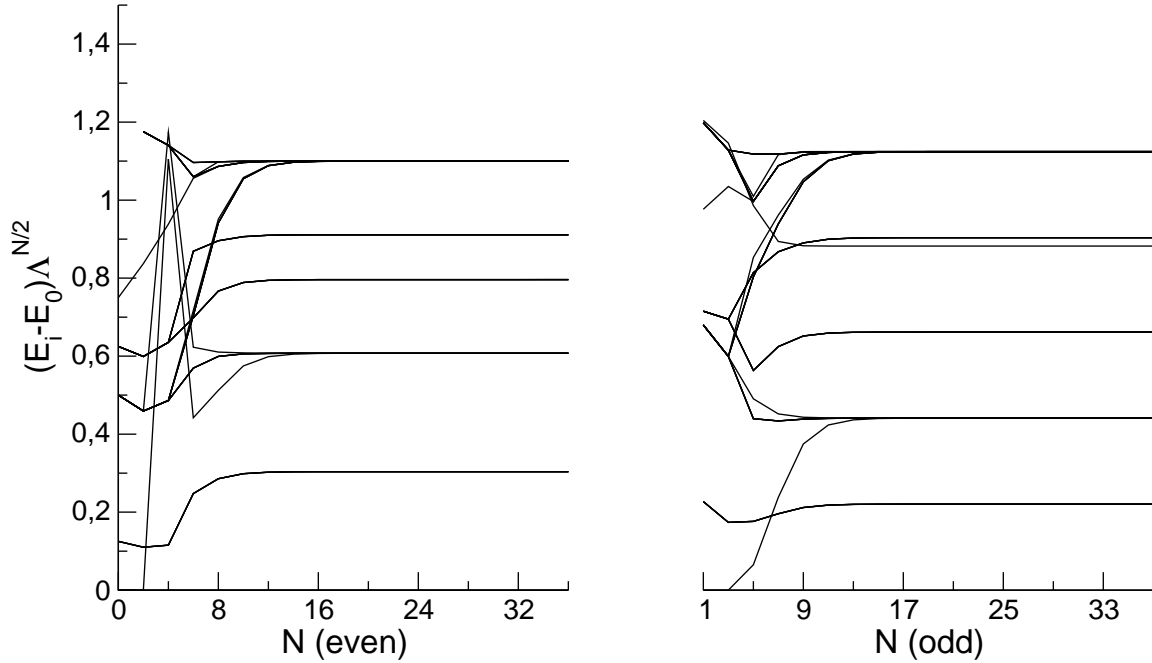


Figure 4.5: Energy flow diagram for the 2CK model, where the exact channel symmetry is broken due to numerical inaccuracy. Parameters were $J_a = J_b = 0.5$, $\Lambda = 4$ with 850 states kept.

vectors with double precision. This tiny inaccuracy might be enough to break the channel symmetry also in the case of initially assumed isotropic couplings. Thus numerical deviations can be the reason for that the system never reaches the non-Fermi liquid fixed point and, instead, a normal 1CK Fermi liquid behaviour occurs for large iteration numbers N . Fig. 4.5 shows that issue in the energy level flow for initially isotropic couplings. One realizes that at $N = 4$ an abnormal 'jump' occurs for some energy levels. After that obvious inaccuracy the system quickly evolves to a normal Fermi liquid fixed point with uniform level spacing. Note that now also an even-odd effect occurs, which is further evidence for a 1CK FL behaviour. A successful program convergence is thus no proof for the occurrence of the correct fixed point.

To avoid these inaccuracies a sufficiently large number of states is kept during each iteration, while still ensuring reasonable program runtimes. Each flow diagram for every value of J had to be checked carefully. For several values of J , the results were double-checked for two different values of the number of states kept. Another improvement in order to avoid the symmetry-breaking numerical instabilities was implemented in our program: It is checked whether the truncation of states in each iteration would happen right through a degenerate level. All eigenstates which have exactly the same

eigenenergy as the designated last state to be kept additionally remain in the NRG iteration and 'survive' the truncation procedure. This ensures that no quantumnumber is favored over another and thus any asymmetry enters the problem.

After one has checked for the stability of the non-Fermi liquid fixed point at the correct energy eigenvalues one can start with the analysis of the dependence of the crossover energy on J . Fig. 4.6 shows that regardless of which initial value of J the energy levels flow to the same fixed point values.

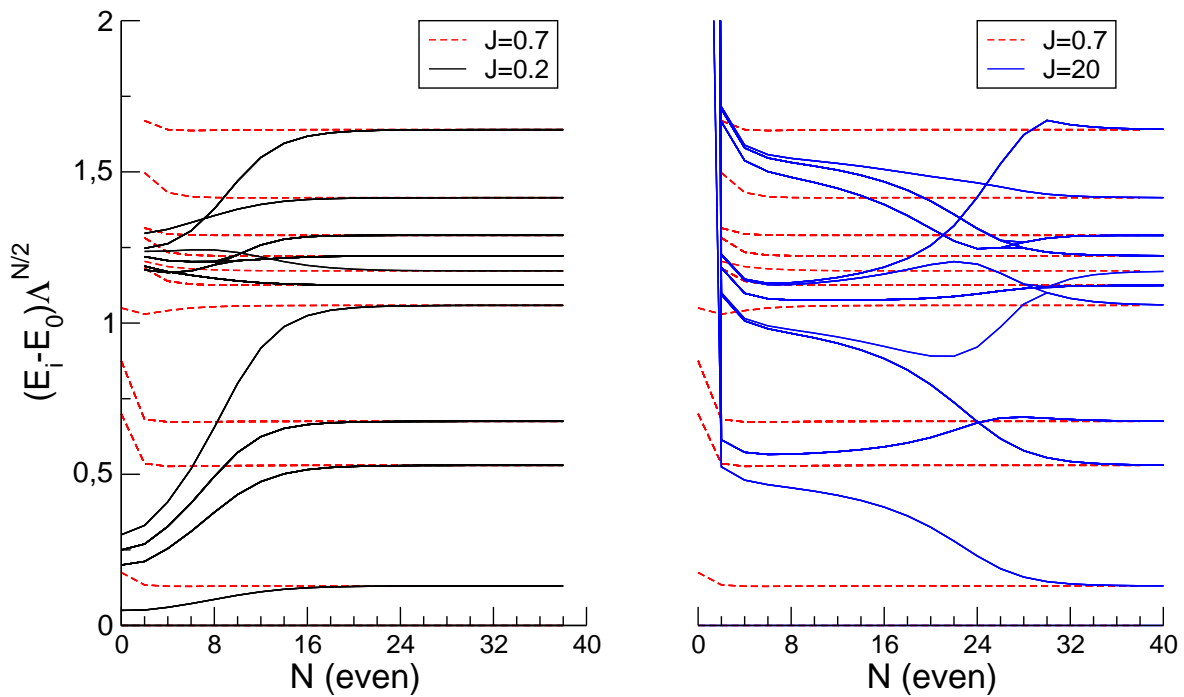


Figure 4.6: Lowest NRG energy levels of the isotropic 2CK model for different initial couplings J . Independently of initial weak-coupling ($J/D = 0.2$), intermediate coupling ($J/D = 0.7$) or strong-coupling ($J/D = 20$), the same fixed point values are reached.

By studying a variety of couplings, we can confirm the result of [50], that the renormalized fixed point value of J is about $J_c = 0.7D$. In this case the energy eigenvalues almost immediately settle to the fixed point value (see Fig. 4.6).

We define the crossover temperature scale T_K^* by $T_K^* = \Lambda^{-(N_K-1)/2}$, where N_K is the iteration number when the first excited energy level is reached within 10 percent of its fixed point value. This temperature scale T_K^* is taken as our value for the Kondo temperature T_K in the following. There are rather different definitions for T_K , one could e. g. take the inflection point of the first excited energy level line. But then every flow diagram where the first excited energy is already reached during the very

first iterations could not be evaluated, since there is no inflection point in this case. Our definition for T_K only fails for situations where the fixed point energy value is already reached within the first evaluated (even or odd) iteration. Anyhow it is sufficient to observe the expected peaked distribution of $P(T_K)$.

Our main result is shown in Fig. 4.7. For several initial couplings and two different NRG discretizations Λ the crossover temperature T_K^* was determined and the corresponding distribution $P(T_K^*)$ vs. J shows a strong peak at around $J = 0.7D$, as expected.

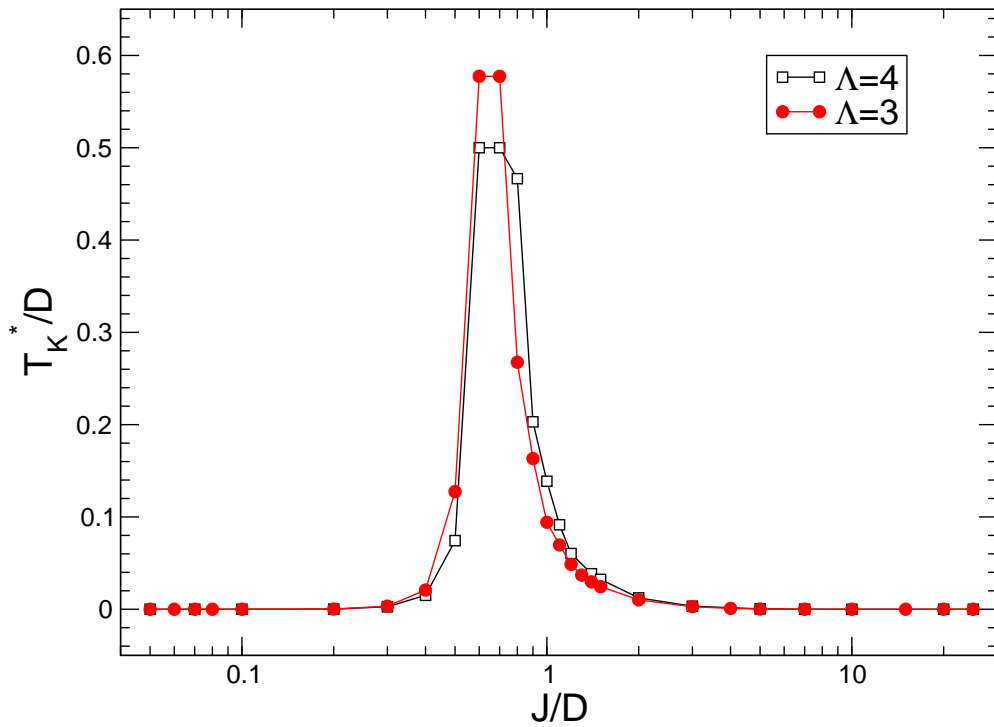


Figure 4.7: Distribution of the crossover temperature T_K^* (defined in the text) vs. the initial coupling strength J (both in units of D).

The results for the two considered discretizations Λ show no significant differences. Thus it could be excluded that we missed any Λ dependent factor in the derivations. The deviations in the intermediate coupling regime around the peak maximum in Figure 4.7 arise from the difficulty to determine the exact T_K^* when the crossover happens at the very beginning of the NRG iterations.

The behavior of T_K^* is examined over nearly three decades of J and extends over more than 10 decades in T_K^* , as illustrated in Figure 4.8.

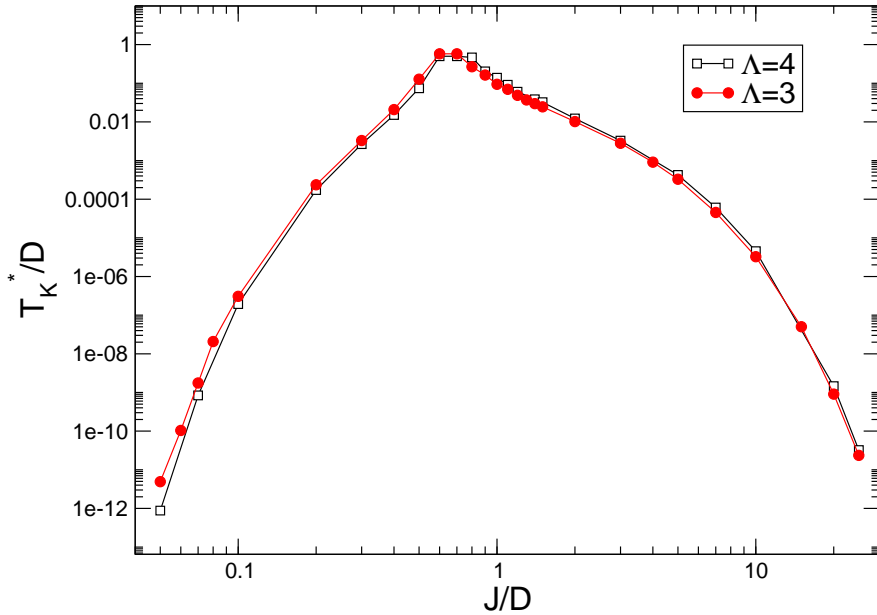


Figure 4.8: Distribution of the crossover temperature T_K^* on a logarithmic scale vs. the initial coupling strength J (both in units of D).

As was previously known from weak coupling perturbation theory, the Kondo scale T_K depends exponentially on the Kondo coupling J . Usually, one defines the Kondo temperature T_K at the point, where the second order term in perturbation theory is equal to the first-order term. The following expression for the one-channel Kondo model is also valid in the two-channel case with different prefactors:

$$k_B T_K \approx D e^{-\frac{1}{2N(0)J}}, \quad (4.10)$$

where $N(0)$ is the conduction electron DoS at E_F . As we use a flat density of states in our calculations ($N(0) = 1/2D$), one can identify the weak coupling regime in a log-linear plot of T_K^* vs. $-1/J$: For small values of $|J|$, $\log T_K^*$ is linearly related to $-1/J$ (see Figure 4.9). This is the parameter regime where one could still use perturbative methods. Beyond the weak coupling regime, a non-perturbative method as the NRG has to be used. For comparison, the Kondo temperature as determined from the inflection point of the first excited energy level is shown in Fig. 4.9. As already mentioned the determination of the inflection point is only possible if the level starts reasonably far away from its fixed point value, otherwise there is no change in the curvature of the energy level. Thus this method could only be used for the first five datapoints up to $J/D = 0.3$.

The results nicely show the exponential behavior of T_K vs. J in the weak coupling regime. The values of T_K following the inflection point method are by a factor higher than in our definition, since the inflection point is reached earlier in the flow as our 'within 10 percent' criterion. The slope in a $\ln(T_K^*/D)$ vs. $(-D/J)$ plot should be

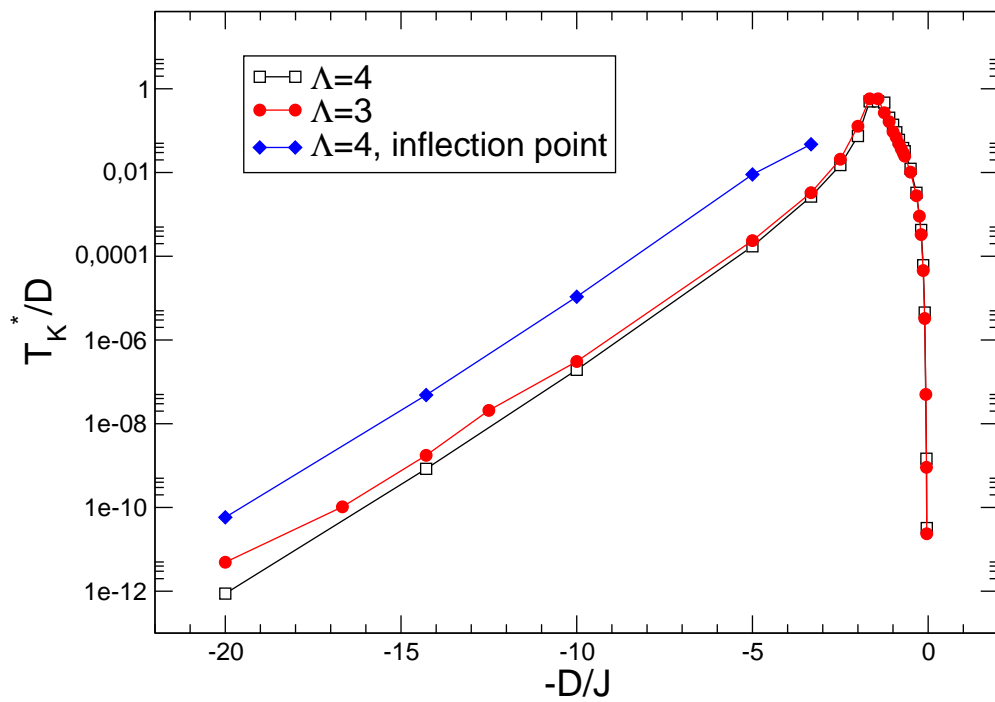


Figure 4.9: Distribution of the crossover temperature T_K^* on a logarithmic scale vs. $(-1/J)$ (both in units of D). The linear behavior for small $|J|$ reflects the exponential dependence of T_K on J as expected from perturbation theory.

exactly 1, if the Kondo temperature follows Eq. 4.10 with $N(0) = 1/2D$. A linear fit to the $\Lambda = 4$ data up to $J/D = 0.3$ yields 1.23 and 1.24 for our T_K^* and the inflection point T_K , respectively. The deviation from unity could possibly be explained with higher order correction terms to the estimate for T_K (Eq. 4.10). If one would include terms of order J^3 in the scaling equations (instead of the usual calculations up to order J^2), one arrives at $k_B T_K \sim D e^{-1/(2J\rho_0)+1/2(\ln(2J\rho_0)+\mathcal{O}(J\rho_0))}$ [1].

4.1.4 Conclusion and outlook

We confirmed by explicit non-perturbative NRG calculations that within the 2CK scenario a wide distribution of the Kondo coupling constant J leads to a narrow, peaked distribution of the Kondo temperature T_K . The fact that only a narrow region of T_K is measured in quantum point contact experiments can now be explained: Although the coupling constants J of the Kondo defects may be statistically distributed, the according Kondo temperature T_K is much too low to be measured for most of the values of J . Only a small region around a critical value of $J_c = 0.7D$ has a T_K high enough to be accessed experimentally and observed through the 2CK behavior. The exponential dependence of T_K on J in the weak coupling regime could be verified. Our results are summarized in the following paper [84].

A stable 2CK NRG code was developed, implementing the symmetries commonly used in NRG programs.

With slight modifications the existing 2CK code could be used to analyze other multi-channel Kondo or Anderson models as well. We implemented an NRG solution for an Anderson impurity model with an additional screening channel, also showing non-Fermi liquid behavior, which serves as a model for the high- T_c superconductivity in cuprates. The first results on this subject were reported by Perakis *et al.* [85, 86], extensively for the particle-hole symmetric case. With our program we are able to reconsider the model also away from particle-hole symmetry.

Chapter 5

Multiorbital Anderson impurities

In this chapter we present our work on explaining the lineshapes measured in scanning tunneling microscopy (STM) experiments of transition metal atoms on metal surfaces. In contrast to the previous chapters, there will be no application of the NRG here. All the calculations were performed using a modified multi-orbital Non-Crossing Approximation (NCA) program.

5.1 Experimental/Theoretical Situation

5.1.1 The Kondo effect in STM experiments

One of the first direct spectroscopic observations of the Kondo effect for an isolated magnetic impurity in a non-magnetic host was reported in [19]: In an STM experiment, the differential conductance dI/dV was measured for Cobalt (Co) atoms deposited onto the (111) face of a clean gold (Au) crystal at 4 K (see Fig. 5.1). When moving the tip across the position of a single Co impurity, one sees a resonance structure appearing around the Fermi energy E_F (see Fig. 5.2).

The vanishing of the features in the spectra at positions away from the impurity atom excludes the possibility of the tip material causing the features in the spectra. An interpretation of the lineshape can rather be given in terms of the Kondo effect: Below a characteristic temperature T_K , the excitation spectrum of a magnetic atom in a metallic host exhibits a narrow many-body (Kondo) resonance at the Fermi level. An electron out of the STM tip has now 2 possible tunneling channels: the d orbital and the continuum of the conduction band electrons of the host metal. Because of quantum interference between these 2 channels, the observed lineshape therefore does not reflect the d -orbital spectral density alone, which would yield a Lorentzian-like peak.

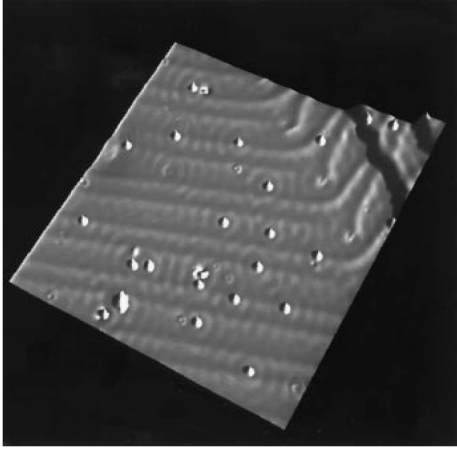


Figure 5.1: Constant-current image (400 \AA by 400 \AA) of the Au(111) surface after cobalt deposition at 4 K. Approximately 22 Co atoms can be seen [19].

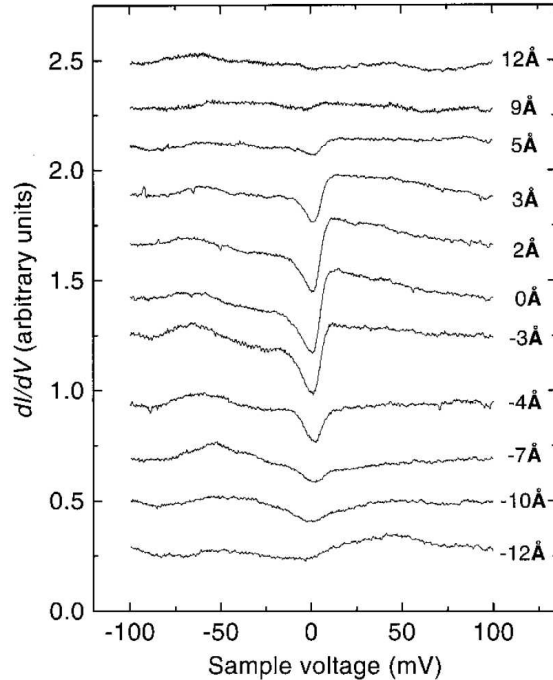


Figure 5.2: dI/dV spectra taken with the STM tip at various distances of a single cobalt atom [19].

The appearing peak-dip structure can be explained by the theory of Fano [87] who calculated, in the context of atomic physics, the effect of such an interference for transitions from an arbitrary initial state to a non-interacting discrete state in resonance with a continuum. Detailed explanations of the Fano lineshape follow in chapter 5.1.2.

Since the magnetic properties of an impurity atom vary depending on the nature of the impurity d -level, STM measurements across the whole transition metal $3d$ row were performed [88] (see Fig. 5.3).

The experiments show spectroscopic features at the beginning and at the end of the $3d$ row (see Fig. 5.4). Again, the interpretation is tunneling from the STM tip into the d -orbital and the conduction electron continuum. However, an absolute identification of the observed features remains to be done.

As e. g. in the case of Ni (see lower spectrum of Fig. 5.5) one is not able to decide if the spectral feature is a bare d -resonance or a broadened Kondo peak. Additionally, in [88] the question about the reason why particular d -resonances appear in the spectra and others do not could not be answered. The dependence on temperature and magnetic field also had to be addressed to further studies.

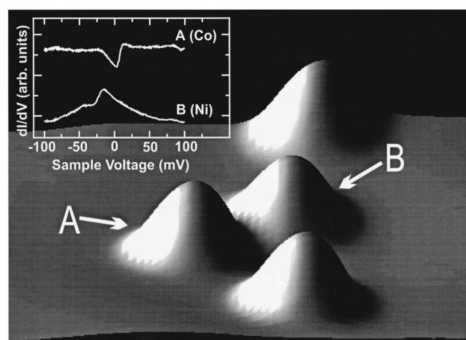


Figure 5.3: Constant-current image (50 Å across) of Co and Ni atoms on Au(111). The inset shows dI/dV spectra with the tip held over atoms *A* and *B*. Taken from [88].

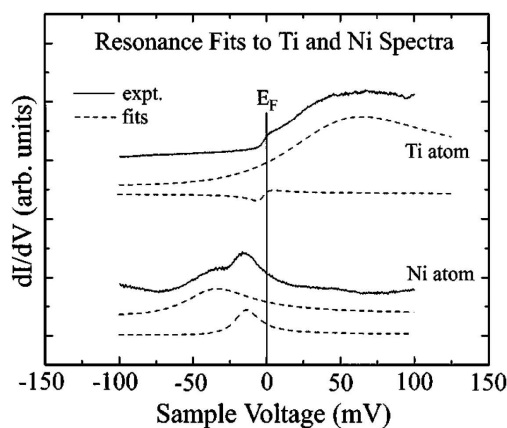


Figure 5.5: dI/dV spectra for Ti and Ni monomers shown with corresponding theoretical decomposition into adjacent Fano resonances [88].

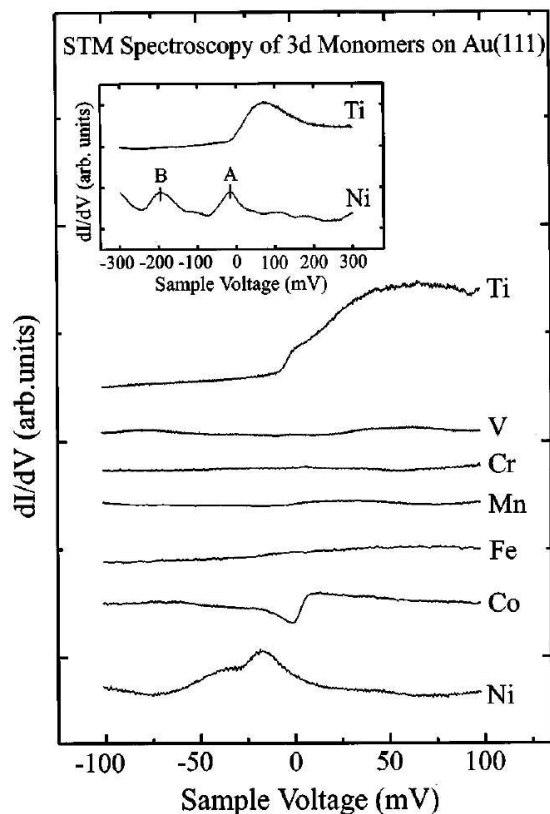


Figure 5.4: dI/dV spectra taken with the STM tip held over individual transition metal impurities on the surface of Au(111) at $T = 6K$ [88].

A study of the temperature dependence of the Kondo peak was then performed by [89] in a Ti/Ag(100) system (see Figure 5.6).

The temperature dependence of the Kondo resonance width follows Fermi liquid theory at low T . But still the exact origin of the two underlying resonances forming the dI/dV spectrum (see figure 5.7) could not be located in [89] (“The other, broader resonance (...) thus likely originates from a bare Ti d resonance”).

A microscopic theory of the Kondo line shape in STM experiments was studied in

[90] and will be described in the following chapter.

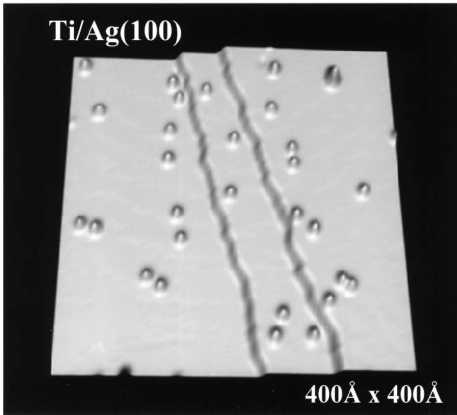


Figure 5.6: Constant-current topograph of a Ag(100) surface after deposition of titanium at 6.8K [89].

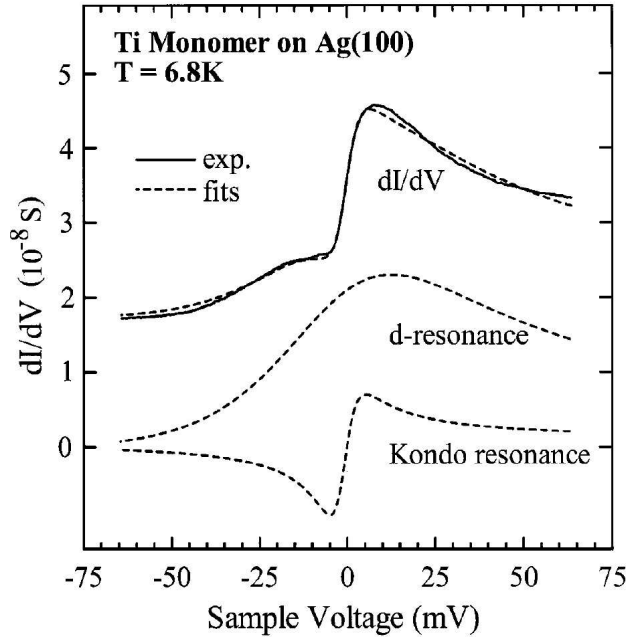


Figure 5.7: dI/dV spectrum for Ti on Ag(100) and two extracted resonances, identified as a Kondo resonance and a bare Ti d -resonance [89].

5.1.2 A microscopic theory in the Kondo regime

Ujsaghy *et al.* [90] combined band structure and strongly correlated calculations to obtain width and shift of the Kondo resonance in STM experiments with cobalt impurities. The magnetic Kondo impurity induces a narrow Fano resonance in the local conduction electron density of states (LDoS).

The following calculations assume that the STM current is predominantly due to tunneling into the conduction LDoS, neglecting direct tunneling into the d -level of the Co ion. This assumption is justified, since the d -level is localized deeply in the atomic core and thus the level cannot be excited easily from the outside. Direct experimental evidence is given in [22]: A Kondo ion is placed in one focus of an elliptic quantum corral. The conduction LDoS which can then be measured in the other focus of the ellipse (and thus separated from the d -level) still shows a Fano line shape.

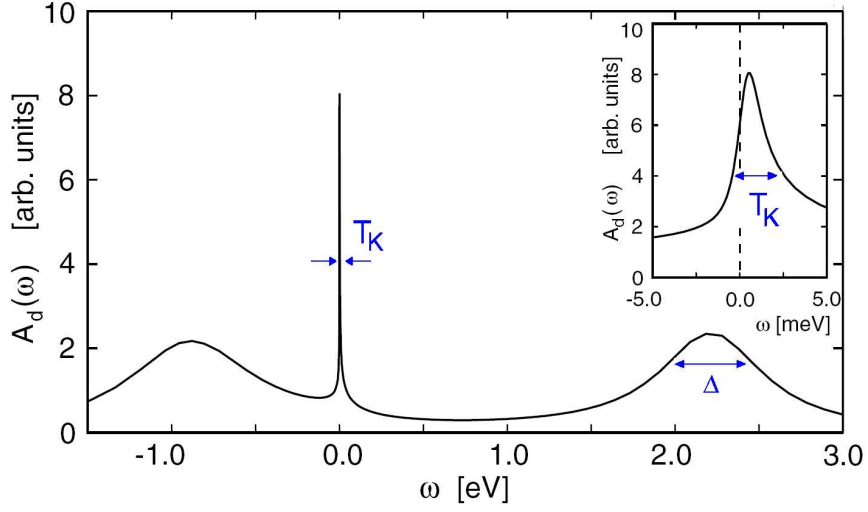


Figure 5.8: Local NCA spectral function $A_d(\omega)$ as obtained within [90].

The starting point for the calculations of a Co atom on a Au surface is the Anderson model [5] with fivefold degeneracy of the d -level $\varepsilon_d < 0$, $m = 1, \dots, 5$:

$$\begin{aligned} \mathcal{H} = & \mathcal{H}_0 + \varepsilon_d \sum_{m,\sigma} d_{m\sigma}^\dagger d_{m\sigma} + V \sum_{m\sigma\vec{k}} \left(c_{\vec{k}\sigma}^\dagger d_{m\sigma} + h.c. \right) \\ & + \frac{U}{2} \sum_{(m,\sigma) \neq (m',\sigma')} d_{m\sigma}^\dagger d_{m\sigma} d_{m'\sigma'}^\dagger d_{m'\sigma'} \end{aligned} \quad (5.1)$$

where $\mathcal{H}_0 = \sum_{\vec{k}} \varepsilon_{\vec{k}} c_{\vec{k}\sigma}^\dagger c_{\vec{k}\sigma}$ describes the conduction band with dispersion $\varepsilon_{\vec{k}}$ and $c_{\vec{k}\sigma}$, $d_{m\sigma}$ are the electron operators in the conduction band and in the titanium d -levels ($m = 1, \dots, 5$), respectively. U is the local Coulomb repulsion between two electrons in any of the d -levels. In the impurity d -level spectral function one can see two types of resonances (see also Figure 5.8):

- (i) the Co d -levels with a broadening $\Delta = \pi|V|^2\rho_0$, at positions ε_d and $\varepsilon_d + U$.
- (ii) the Kondo resonance with width T_K .

To get realistic parameters for the model in order to make contact with experiment, the authors of [90] calculated the electronic structure of a Co impurity placed onto a Au(111) surface using a Korringa-Kohn-Rostoker method in combination with the local spin-density approach (LSDA). The Co d -orbital spectral function was calculated using the NCA [36, 32] and is shown in Figure 5.8. To calculate the conduction electron LDoS as measured by the STM tip at a distance R from the impurity (see Figure 5.9),

one considers the exact conduction electron t -matrix of the Anderson model (5.1), which is given in terms of the d -electron Green's function as $t_\sigma(i\omega_n) = \frac{\Delta}{\pi\rho_0}G_{d,\sigma}(i\omega_n)$. The correction to the conduction electron Green's function due to the presence of the impurity, $\delta\mathcal{G}_{R,\sigma}(i\omega_n) = \mathcal{G}_{R,\sigma}(i\omega_n) - \mathcal{G}_{R,\sigma}^{(0)}(i\omega_n)$, is then

$$\delta\mathcal{G}_{R,\sigma}(i\omega_n) = \mathcal{G}_{R,\sigma}^{(0)}(i\omega_n)t_\sigma(i\omega_n)\mathcal{G}_{R,\sigma}^{(0)}(i\omega_n). \quad (5.2)$$

The STM tunneling current is proportional to the perturbation in the LDoS at distance R , which can be calculated via

$$\delta\rho_{R,\sigma}(\omega) = \frac{1}{\pi}\text{Im}\delta\mathcal{G}_{R,\sigma}(\omega - i\delta) \quad (5.3)$$

Evaluating equation (5.3) using equation (5.2), one gets combinations of real and imaginary parts of the bare conduction electron Green's function $\mathcal{G}_{R,\sigma}^{(0)}$:

$$\begin{aligned} \delta\rho_{R,\sigma}(\omega) &= \frac{1}{\pi} \left[\text{Im}\mathcal{G}_{R,\sigma}^{(0)}(\omega - i\delta) \right]^2 \\ &\times \left[(q_{R,\sigma}^2 - 1)\text{Im}t_\sigma(\omega - i\delta) + 2q_{R,\sigma}\text{Re}t_\sigma(\omega - i\delta) \right], \end{aligned} \quad (5.4)$$

where $q_{R,\sigma}$ is defined as

$$q_{R,\sigma} = \frac{\text{Re}\mathcal{G}_{R,\sigma}^{(0)}(\omega - i\delta)}{\text{Im}\mathcal{G}_{R,\sigma}^{(0)}(\omega - i\delta)}. \quad (5.5)$$

Dropping the spin index σ and considering only the $\omega = 0$ values for $\text{Im}\mathcal{G}_R^{(0)}(\omega - i\delta)$ and q_R , which is justified as these quantities depend only weakly on the energy on the scale T_K , at $R = 0$, $q_{R=0}$ is identical to the asymmetry factor q of the Fano theory [87]. Further taking $t(\omega - i\delta)$ to be simple single-particle level ($t(\omega - i\delta) = (\Delta/\pi\rho_0)/(\omega - \varepsilon_d - i\Delta)$), the lineshape of Eq. (5.4) reduces to Fano's expression

$$\rho(\omega) = \rho_0 + \delta\rho = \rho_0 \frac{(x + q)^2}{x^2 + 1}, \quad \text{with } x = \frac{\omega - \varepsilon_d}{\Delta}. \quad (5.6)$$

What is important to notice is that the Fano line shape of equation (5.6) arises from the mixing of real and imaginary parts in Eq. (5.4). Ujsaghy et al. further examined the LDoS correction (Eq. (5.4)) also in the interacting case and finally arrived at the following expression, valid in the Kondo regime:

$$\delta\rho_R(\omega) = \frac{\left[\text{Im}\mathcal{G}_{R,\sigma}^{(0)}(\omega - i\delta) \right]^2}{\pi\rho_0} \cdot \left\{ \frac{2q_R\varepsilon + q_R^2 - 1}{\varepsilon^2 + 1} + C_R \right\}, \quad (5.7)$$

with $\varepsilon = (\omega - \varepsilon_K)/T_K$ and a correction factor C_R due to potential scattering by the d -level.

Equation (5.7) could be used to fit the experimental data for a Co atom on a Au(111) surface [19] with excellent agreement (see Figure 5.10).

In summary, Ujsaghy *et al.* [90] succeeded to explain the peak-dip lineshapes in STM experiments of magnetic impurities on metal surfaces. The Fano shape arises independently whether the local level is a single-particle orbital of a many-body resonance like in the Kondo effect. Qualitatively they also could reproduce the dependence of the lineshape on the distance of the STM tip from the impurity.

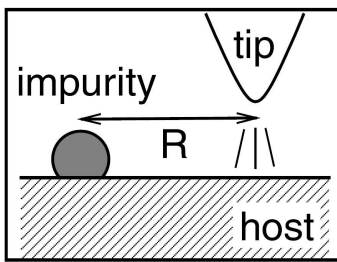


Figure 5.9: Sketch of an STM experiment setup [90].

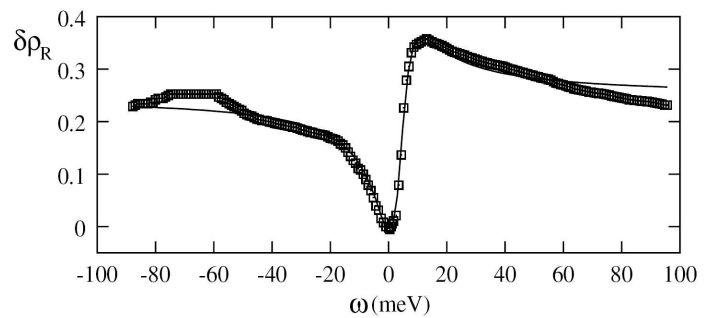


Figure 5.10: Fit (solid line) to the experimental data [19] (squares) as obtained in [90]. The corresponding Fano asymmetry parameter here is $q_{R=0} = 0.66$.

5.2 Motivation

5.2.1 A theory for the mixed valence regime

In the work of Luo *et al.* [91] it is claimed that a “unified microscopic picture for the Fano resonance in both Kondo and mixed valence regimes in the Anderson impurity systems” is established. As the authors of [91] compare their results to the results of [90], but made conceptual mistakes in their derivation, we were triggered to comment on their failures in [92].

Luo *et al.*’s work is about Fano resonance lineshapes arising in STM experiments of Co and Ti impurities on Au or Ag surfaces. Especially the differential conductance dI/dV spectra of the Ti/Ag(100) and Ti/Au(111) systems [89, 88] are claimed to be fully understood. The key point of Luo *et al.*’s analysis is that there is not only a Fano interference effect between the impurity d orbital and the conduction electron continuum, but that the Kondo resonance has by itself a *second* Fano line shape. In [92] we explain why this is conceptually incorrect and thus the quantitative agreement with the experimental spectra is meaningless.

Luo et al. adopt an effective Fermi liquid (FL) picture, where the local impurity spectral function consists of three well-defined quasiparticle states, the two single-particle peaks at ε_d and $\varepsilon_d + U$, respectively, and the Kondo resonance near the Fermi energy ε_F (compare also the peaks in Fig. 5.8). Phenomenologically, the authors describe that by means of a Dyson equation (Eq. (4) in [91]) with a potential scattering T matrix $T_d(\omega)$. But their Dyson equation wrongly mixes many-body and single-particle physics: Their “unperturbed” Green’s function G_d^0 already corresponds to an interacting Hamiltonian with finite Coulomb onsite repulsion U . Thus Wick’s theorem cannot be used in such a case and the Dyson equation cannot be formulated in terms of G_d^0 (Eq. (5) in [91]). Consequently, Luo et al.’s assumption for $T_d(\omega)$ (their Eq. (7)) is unjustified and without any derivation. The most striking evidence for the failure of Luo et al.’s theory is their Fano lineshape for the local spectral density $\rho_d(\omega)$ (their Eq.(8)). Figure 5.11 shows $\rho_d(\omega)$ as obtained by Eq. (8) and the fit results of [91].

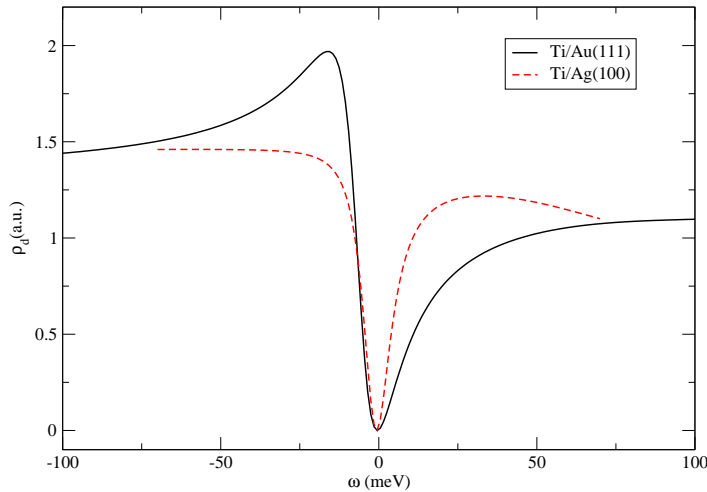


Figure 5.11: Local spectral density $\rho_d(\omega)$ as obtained with Eq. (8) and the fit parameters of [91]

It is known from numerous exact NRG solutions of the Anderson impurity model (see e.g. [32, 1, 43]) that the local spectral density $\rho_d(\omega)$ has a simple peak near the Fermi energy – which may become slightly asymmetric in the case of particle-hole asymmetry ($\varepsilon_d \neq -U/2$) – but by no means the peak-dip shape of a Fano resonance (as in Fig. 5.11).

Another mistake in the paper of Luo et al. is their statement of having two distinct energy scales Δ and Γ_K even in the mixed valence regime. But in this regime the low-energy spin-flip scattering (leading to the Kondo peak of width Γ_K) and the high-energy Coulomb and hybridization processes (giving rise to the scale Δ) are not separated

anymore. The two peaks merge into a single broad peak (of width $\sim \Delta$) around the Fermi energy.

The fitting of Luo *et al.*'s expressions to the Ti/Ag(100) and Ti/Au(111) systems yields a “mixed valence” resonance width of $\Delta = 29.2$ meV and $\Delta = 54.5$ meV, respectively. By contrast, in other transition metal systems as well as in rare earth systems (e.g. Ce compounds) the measured resonance width Δ using photoemission are in the order of 0.5 eV, thus one order of magnitude higher. The narrow experimental peak widths rather suggest that the peaks are Kondo resonances. This idea will be picked up in our theoretical approach to the STM lineshape analysis of the Ti systems (see the following sections).

We finally want to comment on the, at first glance, perfect agreement of the fits of Luo *et al.* to the experimental spectra. By introducing a second Fano interference, a second Fano factor q_d in [91] occurs in their analysis (or an additional phase factor $e^{i\delta}$ in their Reply to our Comment [93]), which is not justified by theory. But with an extra fit parameter a better fitting agreement can be reached quite naturally.

5.2.2 Multiple Kondo resonances

As described in chapter 2.2.5, one observes satellite Kondo resonances around the Fermi energy in magnetic multi-orbital Anderson impurity systems. A multi-orbital NCA solution was used to explain the photoemission spectra of cerium impurity systems [38]. The multiple Kondo peaks have not been seen in STM spectroscopy so far. Our first attempt to model the system of titanium atoms on gold and silver surfaces was an Anderson Hamiltonian with orbital degeneracy (and infinite Coulomb repulsion $U \rightarrow \infty$):

$$\mathcal{H} = \mathcal{H}_0 + \sum_{m,\sigma} \varepsilon_{dm} d_{m\sigma}^\dagger d_{m\sigma} + \sum_{m\sigma\vec{k}} \left(V_{\vec{k}m} c_{\vec{k}\sigma}^\dagger d_{m\sigma} + h.c. \right) \quad (5.8)$$

where $\mathcal{H}_0 = \sum_{\vec{k}} \varepsilon_{\vec{k}} c_{\vec{k}\sigma}^\dagger c_{\vec{k}\sigma}$ describes the conduction band with dispersion $\varepsilon_{\vec{k}}$ and $c_{\vec{k}\sigma}$, $d_{m\sigma}$ are the electron operators in the conduction band and in the titanium d -levels ($\varepsilon_{dm} < E_F$), respectively. The hybridization matrix elements $V_{\vec{k}m}$ lead to an effective coupling matrix between $3d$ -states: $\Gamma_{mm'} = \pi \sum_{\vec{k}} V_{m\vec{k}}^* V_{\vec{k}m'} A_{\vec{k}}(0)$, where $A_{\vec{k}}(\omega)$ is the conduction electron spectral function.

It turned out that similar lineshapes to the ones of the Ti/Ag(100) and Ti/Au(111) experiments could not be recovered if one uses the full hybridization matrix, i. e. with non-zero off-diagonal matrix elements ($\Gamma_{mm'} \neq 0$ for $m \neq m'$). For a diagonal hybridization matrix for $m = 2$ local orbitals the NCA spectral peaks already show a good resemblance with the experimental data (see Fig. 5.12).

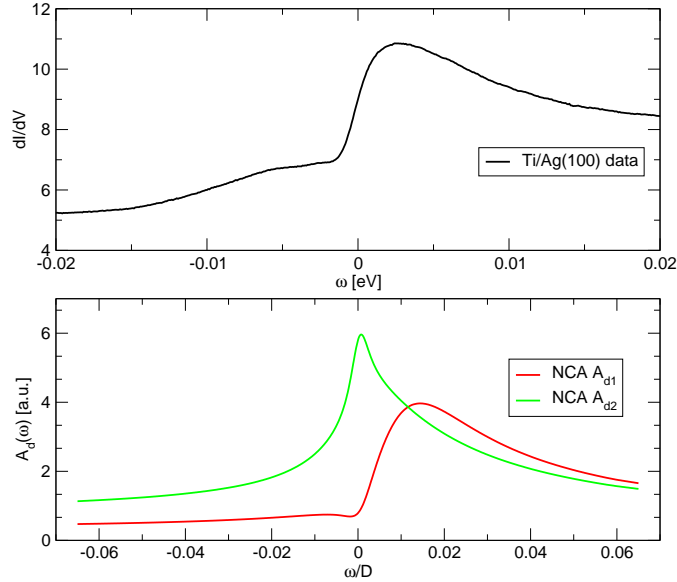


Figure 5.12: Comparison of experimental STM lineshapes (*upper plot*) with NCA spectral peaks for $m = 2$ local orbitals and diagonal hybridization matrix $\Gamma_{mm'}$ (*lower plot*).

5.3 A more realistic model

A realistic description of a $3d$ transition metal system would involve $m = 5$ local d -orbitals, leading to a large parameter space (ε_{dm} , $\Gamma_{mm'}$, possibly phases, ...) which would have to be scanned completely, as the NCA results for the spectral functions are not strictly deterministic. To get further insight into the problem and in order to extract reasonable parameters for our model, we thus used local density functional theory (DFT) calculations for titanium adatoms on silver and gold surfaces, respectively. A minimal set of quantities which enter the NCA calculation are determined with this *ab-initio* method. In particular, the hybridization and the average occupancy of the d -levels can be accurately found. Within the local spin density approximation (LSDA) to DFT we employed the Korringa-Kohn-Rostocker (KKR) Green function method [94], whose results for the local spin-resolved d density of states are shown in figure 5.13 (further details can be found in [95]). The main results of the DFT calculations are

- a local spin moment (within the Wigner-Seitz cell) of $2\mu_B$ at Ti/Ag(001) and $1.98\mu_B$ at Ti/Au(111)
- Hybridization widths of ranging from 0.12–0.31 eV (determined as Lorentzian fits to the peaks in Fig. 5.13)

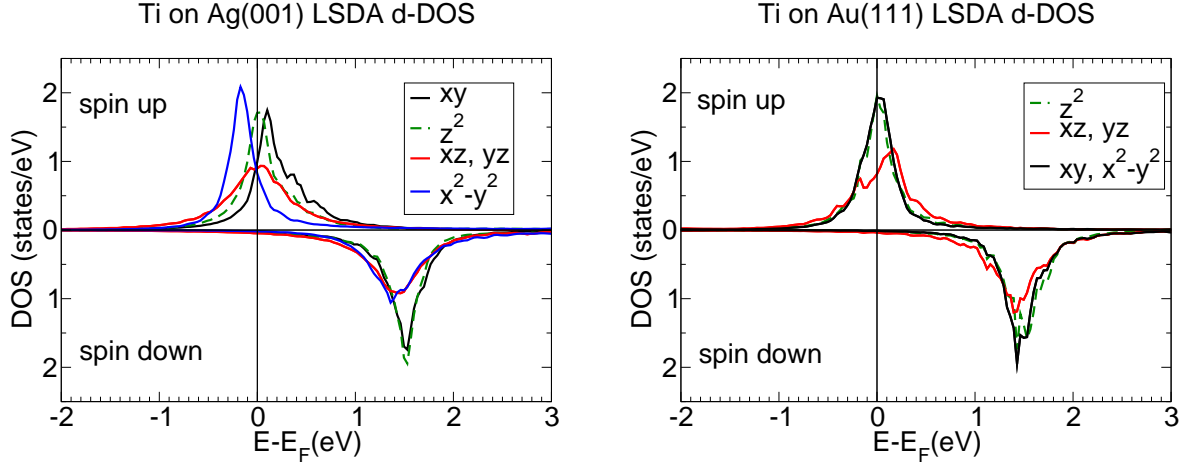


Figure 5.13: *Left plot:* LSDA result for the d density of states for a Ti adatom on Ag(001). The DOS is resolved with respect to spin and to the orbitals corresponding to the point group symmetry of the adatom: d_{xy} , d_{z^2} , $d_{x^2-y^2}$, d_{xz} , and d_{yz} . The last two are degenerate. *Right:* The same for Ti on Au(111). Here there is a splitting of the d orbitals in three irreducible representations: d_{z^2} (singly degenerate), d_{xy} and $d_{x^2-y^2}$ (double degeneracy), and d_{xz} , and d_{yz} (double degeneracy).

- an orbital occupancy of 2 (adding/removing an electron costs 2.86/2.45 eV for Ti/Ag(100))

Thus our improved model incorporates an orbital occupancy of 2 through effective 2-electron impurity states with local spin 1. Due to Hund's rule coupling, the triplet state (total spin $S = 1$) is the three-fold degenerate ground state and the singlet ($S = 0$) is the excited state with excitation energy Δ (see Fig.5.14).

5.3.1 Method of solution

As the NCA proved to give reliable results for multi-orbital Anderson impurity systems, we modified the multi-orbital NCA according to our improved model. To formulate the effective model in auxiliary particle representation, we denote the 2-electron states with pseudo-fermion operators f_{lm} (l being the total local spin and m its z -component):

$$\begin{aligned}
\mathcal{H} = & \sum_{\vec{k}} \varepsilon_{\vec{k}} c_{\vec{k}\sigma}^\dagger c_{\vec{k}\sigma} + \sum_{lm} \varepsilon_{lm} f_{lm}^\dagger f_{lm} \\
& + \sum_{\vec{k}} \left[V_1 \left(c_{\vec{k}\uparrow}^\dagger b_{\uparrow}^\dagger f_{11} + c_{\vec{k}\downarrow}^\dagger b_{\downarrow}^\dagger f_{1-1} \right) + V_2 \sum_{\sigma} \left(c_{\vec{k}-\sigma}^\dagger b_{\sigma}^\dagger f_{10} \right) \right. \\
& \left. + V_3 \sum_{\sigma} c_{\vec{k}-\sigma}^\dagger b_{\sigma}^\dagger f_{00} + h.c. \right] \tag{5.9}
\end{aligned}$$

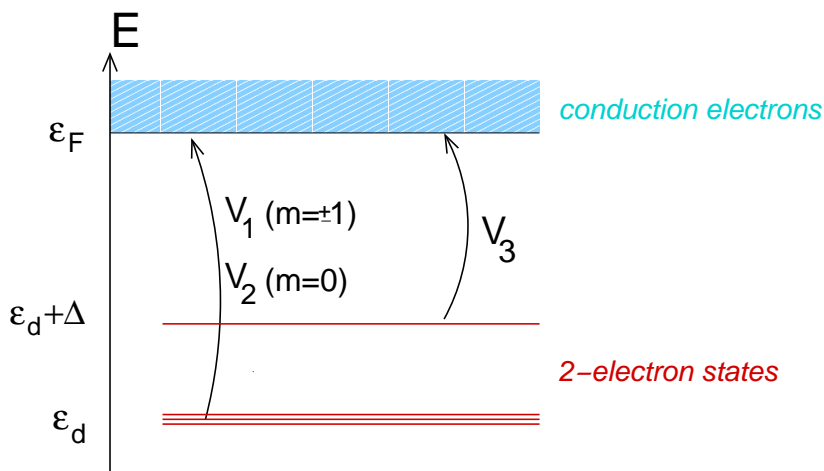


Figure 5.14: Minimal model for 2-electron states in Ti/Au(111) and Ti/Ag(100) systems. Hybridization processes that change the impurity occupation by one unit are shown. There is a different hopping amplitude depending on the initial z -component m of the initial state.

where $\varepsilon_{lm} = \varepsilon_d$ for $l = 1$ and $\varepsilon_{00} = \varepsilon_d + \Delta$ (see Fig. 5.14).

Note that the slave 'boson' operator b_σ represents a singly occupied impurity with spin σ . Due to the projection procedure, already described in section 2.2, it does not matter if one has Fermi or Bose statistics, since they both become a simple Boltzmann distribution function in the limit of infinite chemical potential $\lambda \rightarrow \infty$.

The Green's functions which have to be included in the modified NCA are

$$\begin{aligned}
 G_{1\pm 1}^f &= \left(\omega - \varepsilon_d - \lambda - \Sigma_{1\pm 1}^f \right)^{-1}, \\
 G_{10}^f &= \left(\omega - \varepsilon_d - \lambda - \sum_{\sigma} \Sigma_{10\sigma}^f \right)^{-1}, \\
 G_{00}^f &= \left(\omega - (\varepsilon_d + \Delta) - \lambda - \sum_{\sigma} \Sigma_{00\sigma}^f \right)^{-1}, \\
 G_{\sigma}^b &= \left(\omega - \Sigma_{\sigma}^b \right)^{-1},
 \end{aligned}$$

where the superscript f (b) denotes fermionic (bosonic) Green's functions and $\Sigma^{f(b)}$ the self-energies derived from our Hamiltonian 5.9.

5.4 Results and interpretation

The modified NCA calculations require an estimate for the conduction electron bandwidth D . Following [90] we assume a full bandwidth of 5.5 eV and thus our input for

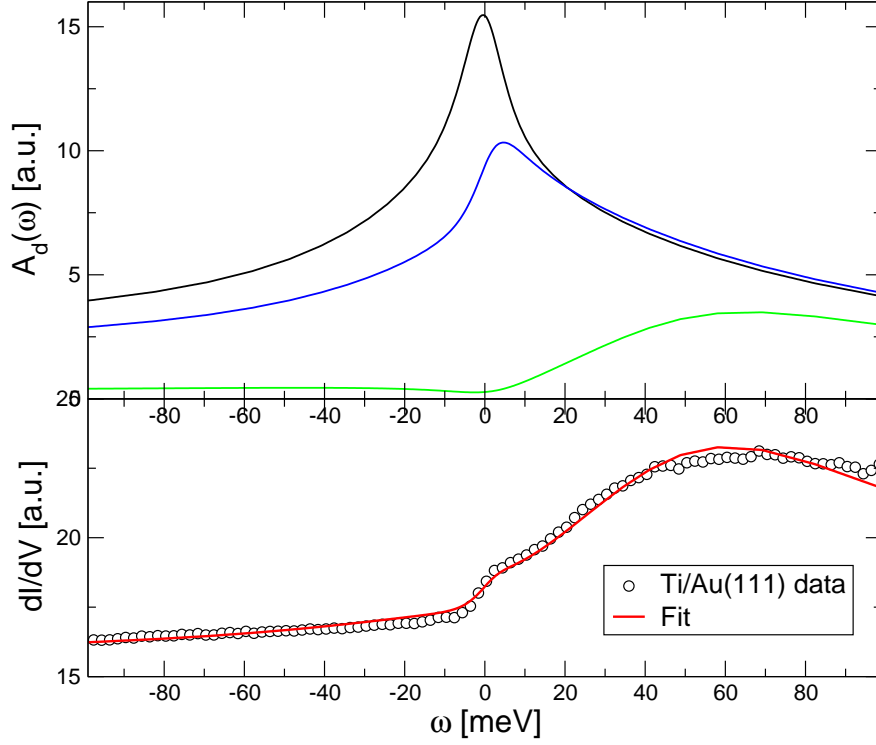


Figure 5.15: NCA spectral functions (*upper plot*) as obtained with the parameters: $\varepsilon_{1m} = 0.66$ eV, $\varepsilon_{00} = 0.655$ eV, $\Gamma_1 = 0.36$ eV, $\Gamma_2 = \Gamma_3 = 0.22$ eV. Superposition of the NCA peaks as a fit to the STM data of Ti/Au(111) (*lower plot*): $dI/dV \propto A_{d1} + 0.18 \cdot A_{d2}$.

the NCA calculations is $D_{NCA} = 2.75$ eV, denoting half of the bandwidth. Starting with hybridization width of about 300 meV, as expected from our DFT results, the rest of the parameters (ε_{dm} , Δ) was tuned such that the resulting NCA spectral peaks reproduce the experimental STM lineshapes. For instance the Ti/Au(111) measurement exhibits a broad Kondo peak for positive frequencies and a sharp feature right at the Fermi energy. Our best fit to the Ti/Au(111) data is shown in Figure 5.15. The NCA yields three different spectral peaks of different width. If one combines the broader resonance (green line, called A_{d1} in the following) and the Kondo peak at the Fermi energy (*blue line*, A_{d2}) with different weight, we are able to recover the experimental STM lineshape: $dI/dV \propto A_{d1} + 0.18 \cdot A_{d2}$.

Also the Ti/Ag(100) data could be explained as a superposition of the NCA spectral peaks with different weight, as illustrated in Figure 5.16.

The usual explanation for the STM lineshapes in transition metal or rare earth systems is tunneling in the single-electron orbitals, eventually combined with a Fano interference effect due to simultaneous tunneling into the conduction electron sea [19, 88, 89, 90]. Our results show that in the titanium systems the STM tunneling current

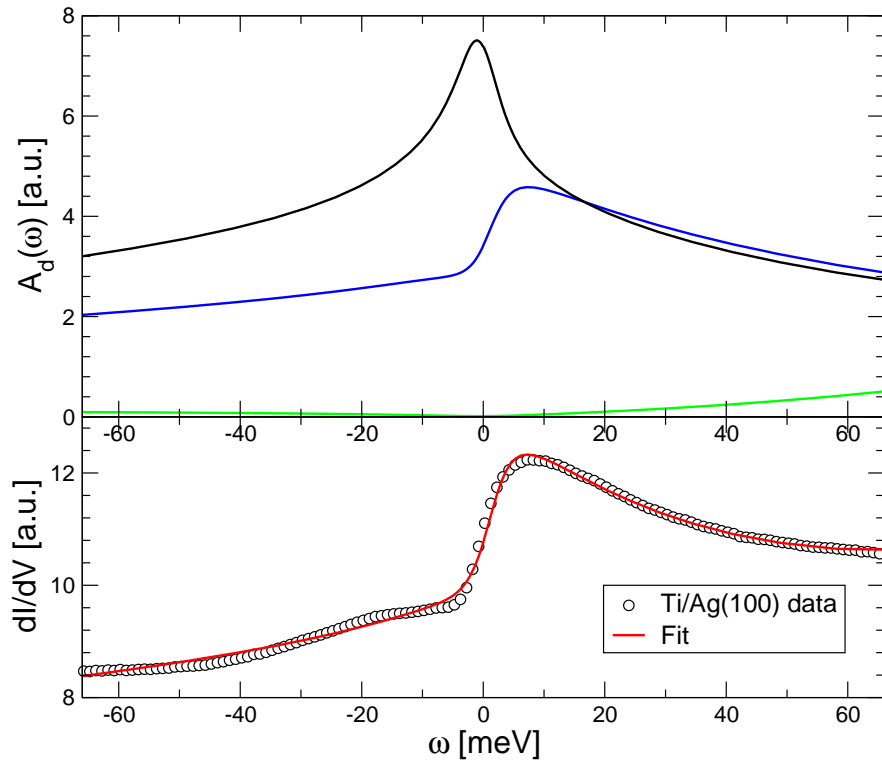


Figure 5.16: NCA spectral functions (*upper plot*) as obtained with the parameters: $\varepsilon_{1m} = 0.55$ eV, $\varepsilon_{00} = 0.54$ eV, $\Gamma_1 = 0.33$ eV, $\Gamma_2 = 0.261$ eV, $\Gamma_3 = 0.275$ eV. Superposition of the NCA peaks as a fit to the STM data of Ti/Ag(100) (*lower plot*): $dI/dV \propto 0.05 \cdot A_{d1} + 0.6 \cdot A_{d2} + A_{d3}$.

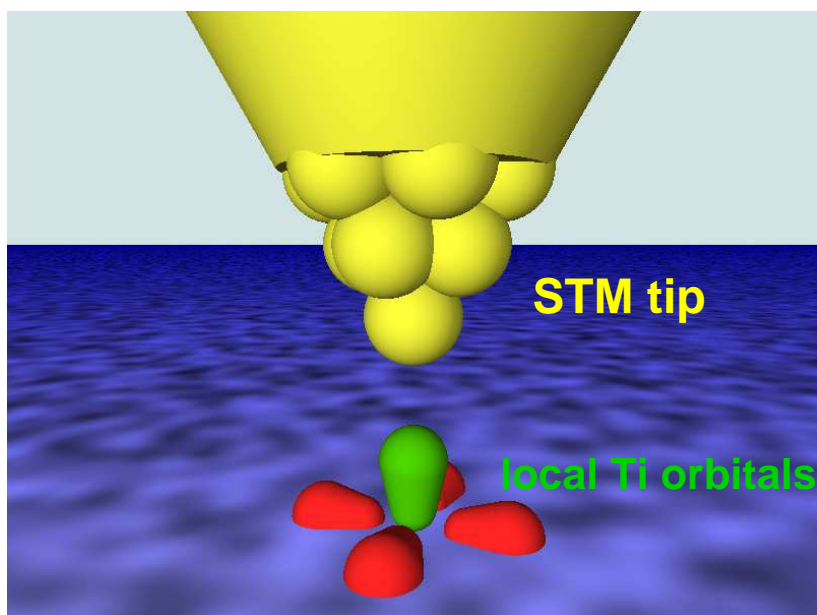


Figure 5.17: Schematic picture of the STM tip (yellow) moving across the host metal surface (blue). Tunneling is favored into local orbitals which stick out of the surface (green orbital as opposed to the red one).

is rather carried by the total spin-1 states consisting of the two electrons in the local titanium orbital. The different occurring relative strengths of the transmission channels can be interpreted by the geometrical orientation of the local orbitals: The STM current will happen predominantly into the local orbital which sticks most out of the metal surface and thus is nearer to the STM tip (see Figure 5.17).

In summary, we combined density functional calculations with a strongly correlated method (the NCA) to develop a method which can explain the complex STM lineshapes occurring for magnetic transition metal atoms on metal surfaces. The relative strengths of the transmission channels in turn provide insight into the orbital geometry of the atomic-size contact. Our results are summarized in [95].

Chapter 6

Summary and Outlook

This thesis contains the description and the application of various numerical methods for quantum impurity systems as examples for strongly correlated electron systems.

We begin with description of the Kondo effect as it is a common problem in condensed matter theory. The explanation of the observed resistance minimum in non-magnetic metals with magnetic impurities was given by J. Kondo in terms of resonant spin-flip scattering of the conduction electrons at the local impurity moment. We then show how Kondo's perturbative calculations break down at a temperature scale T_K , the Kondo temperature, and how Anderson's scaling approach leads to an infinitely strong coupling between conduction electrons and impurity. The non-perturbative solution to the Kondo problem, which has to give results in the low temperature regime $T \ll T_K$, is the numerical renormalization group (NRG) technique, devised by K. G. Wilson. The NRG will be the central topic of this thesis and covered in a later chapter in full detail. Following the course of this thesis, we motivate why the investigation of Kondo phenomena is still an active field of research in modern condensed matter physics.

Besides the NRG there exist many more methods which can tackle problems in quantum impurity systems. Some of them are presented in this thesis. We shortly sketch an analytical method, the Bethe ansatz (BA) technique, which yields reliable results on exact many-body wavefunctions, spectra and thermodynamics over the whole range of temperatures and magnetic field. As the BA is not capable of accessing dynamical properties, we then outline another renormalization group procedure, the density matrix renormalization group (DMRG), which is able to yield results on dynamic properties of a strongly correlated system. The DMRG is one of the most common techniques for one-dimensional quantum systems and is also used for the exact determination of ground state energies. For the treatment of more complex quantum impurity systems, as e. g. models with orbital degeneracy, we describe the Non-Crossing Approximation (NCA) as an approximative, but very flexible, advanced perturbative method. We show in more detail, how an NCA solution is constructed and how the NCA gives valuable results in the context of multi-orbital Anderson impurities.

Our description of the numerical renormalization group (NRG) is the central part

of this thesis. We present a comprehensive overview over the NRG technique and how we implemented it for this thesis. Therefore we derive the NRG method for the single impurity Anderson model (SIAM). We reproduce the original NRG results of Wilson for the Kondo model and of Krishna-murthy *et al.* for the SIAM, where they computed static properties and thermodynamic information. Our NRG program was extended to additionally yield dynamic properties as the impurity spectral function. Again, we present well-known results for the SIAM and sketch how the connection can be made to experiments. Recent extensions of the NRG method are described, as the consideration of additional conduction channels or the investigation of non-equilibrium problems. For the application of the NRG in dynamical mean-field theory (DMFT) calculations we implemented an arbitrary hybridization between conduction band electrons and the impurity. We sketch how we want to use our NRG code for the explanation of the simultaneous semiconductor to metal and para-to-ferromagnetic transition in oxygen-depleted europium oxide (EuO).

Our NRG program is extended to deal with two independent conduction bands, thus modeling the two-channel Kondo (2CK) system. Multi-channel Kondo systems display non-trivial non-Fermi liquid physics in the overcompensated regime, when $M > 2S_I$, where M is the number of conduction channels and S_I the impurity spin. In the 2CK model that we considered ($M = 2$, $S_I = \frac{1}{2}$), the two independent conduction channels try to screen the impurity moment, leading to an overall overscreening. The ground state is not a spin singlet anymore and there is residual entropy. Renewed interest in the multi-channel models arose, since there are several experimental proposals to realize 2CK physics. Furthermore, the 2CK effect may be of importance in the explanation of heavy fermion systems and high- T_c superconductivity. With our work on the 2CK effect, we want to explain the anomalous conductance measurements on quantum point contacts, which are hardly to explain by any other microscopic mechanism. It is expected for nanoscopic point contacts that the Kondo coupling strength J is statistically distributed over the Kondo impurities. In contrast, the experiments reveal a very sharp distribution of the Kondo temperature T_K . With our NRG calculations we explicitly investigate the distribution of T_K versus the initial coupling J . To extract T_K we computed energy flow diagrams for a whole range of initial couplings J and determined the crossover scale to the non-Fermi liquid fixed point. The resulting distribution of T_K versus J is strongly peaked around a critical value of $J_c \approx 0.7D$, where D is the bandwidth. In the weak coupling regime ($J \ll D$) we can confirm the exponential dependence of T_K on J , which can be predicted by perturbative scaling analysis. The fact that the Kondo temperature is very low for coupling strengths different from the intermediate coupling around $0.7D$ explains why the experiments only show a very narrow region for T_K despite an assumed wide distribution of J .

We analyze differential conductance measurements using scanning tunneling microscopy (STM) of transition metal atoms on metal surfaces. We review the role of the Kondo effect in such experiments from the experimental and the theoretical point of view. So far unexplained are the anomalous STM lineshapes occurring for titanium

atoms on gold and silver surfaces. We develop a theory that permits to explain these lineshapes through multiple Kondo resonances. Density functional theory calculations show us that the local titanium orbitals are occupied on average by two electrons and a local spin moment of roughly $2\mu_B$ resides at the impurity site. Additionally we get a rough measure of the hybridization strength between the two-electron states and the conduction electrons of the host metal. We adapt a multi-orbital NCA program to our effective model and calculate the local spectral densities of the titanium orbitals. Our results show that we can recover the measured STM lineshapes through combining the spectral functions with different strengths. These different strengths of transmission channels can be interpreted by the spatial orientation of the titanium orbitals on the metal surface. The tunneling out the STM tip happens predominantly into the orbital which sticks out of the gold or silver surface. To conclude, we used a combination of ab initio band structure calculations with a strongly correlated method to explain the electronic transport and geometry of Kondo atoms on metal surfaces.

Outlook

With the NRG code, which was developed within this thesis, we can tackle a number of problems of quantum impurity systems. The complete thermodynamics and spectral functions can be calculated for the one-channel Kondo model as well as the single impurity Anderson model. The complete eigenstates and eigenenergies can be computed for the two-channel Kondo case. The application of an additional, spinless screening channel is also already implemented. With the extension of spin- and energy-dependent conduction electron density of states, our NRG program is able to act as 'impurity solver' in DMFT calculations. In the near future we want to use the NRG in the explanation of the europium oxide problem.

With our method we developed for the STM lineshape analysis we can now investigate further experimental systems like cerium atoms on metal surfaces.

Chapter 7

Deutsche Zusammenfassung

Die vorliegende Arbeit enthält die Beschreibung und die Anwendung verschiedener numerischer Methoden für Quanten-Störstellensysteme als Beispiele für stark korrelierte Elektronensysteme.

Zu Beginn präsentieren wir den Kondo Effekt als ein oft behandeltes Problem in der Theorie der kondensierten Materie. Das experimentell beobachtete Widerstandsminimum bei nicht-magnetischen Metallen mit metallischen Verunreinigungen erklärte Jun Kondo durch resonante Spinflip-Streuung der Leitungsbandelektronen am lokalen magnetischen Moment der Störstelle. Wir zeigen, wie Kondos störungstheoretische Rechnungen unterhalb der Temperaturskala T_K , der sogenannten Kondotemperatur, zusammenbrechen und wie Anderson's Scaling-Ansatz eine unendlich starke Kopplung zwischen Leitungselektronen und Störstelle erklärt. Eine nicht-störungstheoretische Erklärung dieses Kondo-Problems, nämlich die Berechnung des Tieftemperaturzustandes für $T \ll T_K$, liefert die numerische Renormierungsgruppe (NRG), entwickelt von K. G. Wilson. Die NRG wird das zentrale Thema dieser Arbeit sein, und wir beschreiben sie im Detail im Hauptteil der Arbeit. Zunächst motivieren wir im weiteren Verlauf der Arbeit, warum die Untersuchung von Kondo-artigen Phänomenen immer noch ein sehr aktives Feld moderner festkörperphysikalischer Forschung ist.

Neben der NRG existieren noch viele weitere Methoden, die Einsichten in Quanten-Störstellensysteme liefern. Wir präsentieren einige davon im Rahmen dieser Arbeit. Kurz gehen wir auf eine analytische Methode zur Lösung des Kondo-Problems ein, die sogenannte Bethe-Ansatz (BA) Technik. Sie liefert verlässliche Resultate über Vielteilchen-Wellenfunktionen, Spektren und die Thermodynamik für den gesamten Temperaturbereich und alle Magnetfeldstärken. Der BA ist jedoch nicht geeignet für die Berechnung von dynamischen Größen. Deshalb skizzieren wir danach kurz eine andere Renormierungsgruppen-Technik, die Dichtematrix-Renormierungsgruppe (DMRG), die auch Ergebnisse zu dynamischen Eigenschaften stark korrelierter Systeme liefern kann. Die DMRG ist eine der meistgebrauchten Techniken für ein-dimensionale Systeme und erlaubt beispielsweise die exakte Bestimmung von Grundzustandsenergien. Zur Behandlung von komplexeren Quanten-Störstellensystemen, zum Beispiel

Modelle mit orbitaler Entartung, erläutern wir die Non-Crossing Approximation (NCA) als eine sehr flexible, fortgeschrittene störungstheoretische Methode. Wir beschreiben ausführlich, wie man die NCA konstruiert und wie sie wertvolle Ergebnisse bei der Analyse von Multi-Orbital Anderson-Störstellensystemen liefert.

Die Beschreibung der numerischen Renormierungsgruppe (NRG) stellt den Hauptteil der vorliegenden Arbeit dar. Wir geben einen umfassenden Überblick über die NRG-Prozedur und zeigen wie wir sie für diese Arbeit implementiert haben. Dafür zeigen wir die Methode im Detail am Beispiel des Einstörstellen-Anderson-Modelles (single impurity Anderson model, SIAM). Mit unserem NRG Programm reproduzieren wir die ersten Resultate von Wilson für das Kondo-Modell und von Krishna-murthy *et al.* für das SIAM, in denen statische Eigenschaften und die Thermodynamik betrachtet wurden. Wir haben unser Programm auf die Berechnung dynamischer Größen wie die lokale Spektralfunktion erweitert. Wiederum können wir bereits wohlbekannt Resultate nachrechnen, und wir beschreiben, wie damit der Bezug zu Experimenten gemacht werden kann. Wir beschreiben neuerliche Erweiterungen der NRG Technik wie die Berücksichtigung zusätzlicher Leitungsbänder oder die Behandlung von Problemen außerhalb des thermodynamischen Gleichgewichts. Um die NRG in dynamischen Molekularfeld-theoretischen (DMFT) Rechnungen einsetzen zu können, wurde unsere NRG auf beliebige Spin- und Energie-abhängige Leitungsband-Zustandsdichten erweitert. Wir zeigen, wie wir unser NRG Programm zur Erklärung des gleichzeitigen Halbleiter-Metall und Para-zu-Ferromagnetismus-Phasenübergangs in sauerstoff-verarmten Europiumoxid (EuO) einsetzen wollen.

Wir erweiterten unsere NRG auf die Einbindung von zwei unabhängigen Leitungsbändern, also um ein Zwei-Kanal-Kondo (2CK) System zu modellieren. Viel-Kanal-Kondo Systeme zeigen nicht-triviales nicht-Fermi-Flüssigkeitsverhalten im überkompensierten Regime, bei dem $M > 2S_I$ ist, wobei M die Zahl der Leitungsbänder und S_I den Störstellenspin beschreibt. Im von uns behandelten 2CK System ($M = 2$, $S_I = \frac{1}{2}$) versuchen die beiden Leitungsbänder unabhängig voneinander, das lokale Störstellenmoment abzuschirmen, was insgesamt eine Überabschirmung zur Folge hat. Der Grundzustand ist kein simples Spin-Singlett mehr und es gibt endliche Entropie. Neuerliches Interesse in die Viel-Kanal-Kondo-Modellen wurde durch einige experimentelle Vorschläge geweckt, die 2CK-Physik realisieren wollen. Außerdem liefert der 2CK Effekt möglicherweise Erklärungen im Zusammenhang mit Schwer-Fermionsystemen und Hochtemperatur-Supraleitung. Mit unserer Arbeit zum 2CK Effekt wollen wir anomale Leitwertmessungen an Quanten-Punktkontakten erklären, die schwerlich durch andere theoretische, mikroskopische Modelle erklärbar sind. Für nanoskopische Punktkontakte erwartet man eine statistische, breite Verteilung für die Kondo-Kopplungsstärke J . Im Gegensatz dazu zeigen die Experimente eine sehr scharfe Verteilung für die Kondo Temperatur. Mit unserem NRG Programm berechnen wir explizit die Verteilung von T_K in Abhängigkeit von der anfänglichen Kopplungsstärke J . Dabei analysieren wir die Crossover-Skala zum nicht-Fermiflüssigkeits-Fixpunkt für eine breite Verteilung von J . Unsere resultierende Verteilung T_K gegen J ist stark um ein intermediäres

$J = 0.7D$ gepeakt, wobei D die Bandbreite der Leitungselektronen ist. Im Bereich schwacher Kopplung ($J \ll D$) können wir die exponentielle Abhängigkeit der Kondotemperatur von J bestätigen, wie man aus störungstheoretischen Scaling-Ansätzen vorhersehen kann. Die Tatsache, daß T_K für die meisten Werte von J außerhalb des intermediären Bereiches sehr niedrig ist, kann erklären, warum man in den Experimenten nur einen sehr engen Bereich für die Kondotemperatur erkennen kann, obwohl man eine statistische Verteilung für J annehmen kann.

Wir analysieren differentielle Leitwertmessungen in Rastertunnelmikroskop- (STM) Experimenten von Übergangsmetallatomen auf metallischen Oberflächen und fassen zusammen, welche wichtige Rolle der Kondo Effekt in solchen Experimenten spielt. Bisher unerklärt sind die anomalen STM-Linienformen, die bei Messungen von Titan-Atomen auf Gold- und Silber-Oberflächen auftreten. Wir haben eine Theorie entwickelt, die es erlaubt, diese Linienformen mittels Vielfach-Kondoresonanzen zu erklären. Dichtefunktional-Rechnungen zeigen uns, daß ein Titan-Orbital auf Gold oder Silber im Mittel mit zwei Elektronen besetzt ist und daß die Titan-Störstelle ein lokales Spin-Moment von ungefähr $2\mu_B$ trägt. Außerdem erhalten wir eine grobe Abschätzung für die Hybridisierungsstärke zwischen den Zwei-Elektronenzuständen im lokalen Orbital und den Leitungsbandelektronen des unterliegenden Metalls. Mittels einer auf unser effektives Modell erweiterten NCA-Rechnung können wir die lokalen Spektraldichten der Titan-Orbitale berechnen. Unsere Ergebnisse zeigen, daß man die gemessenen STM-Linienformen erhält, wenn man die Spektralfunktionen mit unterschiedlicher Stärke überlagert. Diese unterschiedliche Stärke der Transmissionskanäle kann durch die unterschiedliche räumliche Orientierung der Titan-Orbitale auf der Oberfläche interpretiert werden. Der Tunnelstrom wird hauptsächlich von dem Orbital getragen, das am meisten aus der Oberfläche herausragt. Somit haben wir durch eine Kombination von Bandstruktur-Rechnungen und einer stark korrelierten Methode die Möglichkeit, den elektronischen Transport und die Geometrie von Kondo-Atomen auf Metalloberflächen zu erklären.

Ausblick

Mit dem NRG-Programm, das für diese Arbeit entwickelt wurde, können wir vielfältige Quanten-Störstellenprobleme untersuchen. Für das Ein-Kanal-Kondo-Modell und das Ein-Störstellen-Anderson-Modell kann die komplette Thermodynamik sowie Spektralfunktionen berechnet werden. Das gesamte Eigenspektrum kann sowohl im Zwei-Kanal-Kondo Fall, als auch für ein System mit einem zusätzlichen, spinlosen Abschirmkanal bestimmt werden. Mit der Erweiterung auf beliebige Leitungsbandzustandsdichten ist unsere NRG befähigt, als wichtiger Teil in DMFT-Rechnungen eingesetzt zu werden. In nächster Zukunft benutzen wir die NRG, um eine Erklärung für unser Modell für Europiumoxid zu liefern.

Mit unser neu entwickelten Methode zur Analyse von STM-Linienformen können wir nun auch weitere Kondosysteme betrachten, zum Beispiel Cer-Atome auf Metal-

oberflächen.

Appendix A

Technical details for deriving the NRG equations

This chapter describes technical details on the derivation of the NRG procedure.

A.1 Mapping on a semi-infinite chain

In the discretized version (3.23) of the SIAM Hamiltonian, the impurity still couples to an infinite number of CB electrons (though only to the average part in each logarithmic interval). To solve the the system numerically, the conduction band part is mapped onto the semi-infinite (Wilson) chain:

$$\underbrace{\sum_{n=0,\sigma}^{\infty} (\xi_{n\sigma}^+ a_{n\sigma}^\dagger a_{n\sigma} + \xi_{n\sigma}^- b_{n\sigma}^\dagger b_{n\sigma})}_{\mathcal{H}_{\text{cond.band}}} = \underbrace{\sum_{n=0,\sigma}^{\infty} \left[\varepsilon_{n\sigma} c_{n\sigma}^\dagger c_{n\sigma} + t_{n\sigma} (c_{n\sigma}^\dagger c_{n+1\sigma} + h.c.) \right]}_{\mathcal{H}_{\text{Wilsonchain}}} \quad (\text{A.1})$$

Therefore a tridiagonalization procedure developed by Lánczos [49] with diagonal matrix elements $\varepsilon_{n\sigma}$ and off-diagonal elements $t_{n\sigma}$ is used, equivalent to a Gram-Schmidt orthonormalization. Starting from an initial one-particle state $|\Psi_0\rangle = c_{0\sigma}^\dagger |0\rangle$ (where $|0\rangle$ denotes the Fock vacuum¹), a new single-particle basis is constructed [46] according to:

$$\mathcal{H}_{CB} |\Psi_{n\sigma}\rangle - \underbrace{\langle \Psi_{n\sigma} | \mathcal{H}_{CB} | \Psi_{n\sigma} \rangle}_{\varepsilon_{n\sigma}} |\Psi_{n\sigma}\rangle = \underbrace{\langle \Psi_{n+1\sigma} | \mathcal{H}_{CB} | \Psi_{n\sigma} \rangle}_{t_{n\sigma}} |\Psi_{n+1\sigma}\rangle - \underbrace{\langle \Psi_{n-1\sigma} | \mathcal{H}_{CB} | \Psi_{n\sigma} \rangle}_{t_{n-1\sigma}} |\Psi_{n-1\sigma}\rangle \quad (\text{A.2})$$

¹ $|\Psi_0\rangle$ is called the *maximally localized* state, since it is maximally delocalized in momentum space and hence maximally localized at the impurity site in position space

where the $c_{n\sigma}$ are defined via $|\Psi_n\rangle = c_{n\sigma}^\dagger |0\rangle$, $n \in \mathbb{N}$.

In the following, we make an ansatz for the single-particle operators $c_{n\sigma}$:

$$c_{n\sigma} = \sum_{m=0}^{\infty} (u_{nm\sigma} a_{m\sigma} + v_{nm\sigma} b_{m\sigma}) \quad (\text{A.3})$$

where the coefficients $u_{nm\sigma}$ and $v_{nm\sigma}$ are determined recursively (we follow the calculations of [58]).

Comparing Qq. (3.13) with the ansatz Eq. (A.3) yields the starting values $u_{0m\sigma}$ and $v_{0m\sigma}$ of the recursion:

$$u_{0m\sigma} = \frac{\gamma_{m\sigma}^+}{\sqrt{\xi_{0\sigma}}}, \quad v_{0m\sigma} = \frac{\gamma_{m\sigma}^-}{\sqrt{\xi_{0\sigma}}} \quad (\text{A.4})$$

Inversion of the ansatz leads to $a_{n\sigma} = \sum_{m=0}^{\infty} u_{nm\sigma} c_{m\sigma}$ and $b_{n\sigma} = \sum_{m=0}^{\infty} v_{nm\sigma} c_{m\sigma}$. Inserting $a_{n\sigma}$ and $b_{n\sigma}$ in the l.h.s. of Eq. (A.1) and comparing corresponding operators $c_{n\sigma}$ on both sides of this equation yields

$$\sum_{m=0}^{\infty} (\xi_{m\sigma}^+ u_{nm\sigma} a_{m\sigma}^\dagger + \xi_{m\sigma}^- v_{nm\sigma} b_{m\sigma}^\dagger) = \varepsilon_{n\sigma} c_{n\sigma}^\dagger + t_{n\sigma} c_{n+1\sigma}^\dagger + t_{n-1\sigma} c_{n-1\sigma}^\dagger \quad (\text{A.5})$$

Comparing the ($n = 0$)-component in Eq. (A.5) and using Eq. (A.4) yields

$$\sum_{m=0}^{\infty} \left(\frac{\xi_{m\sigma}^+ \gamma_{m\sigma}^+}{\sqrt{\xi_{0\sigma}}} a_{m\sigma}^\dagger + \frac{\xi_{m\sigma}^- \gamma_{m\sigma}^-}{\sqrt{\xi_{0\sigma}}} b_{m\sigma}^\dagger \right) = \varepsilon_{0\sigma} c_{0\sigma}^\dagger + t_{0\sigma} c_{1\sigma}^\dagger \quad (\text{A.6})$$

Since the $c_{n\sigma}$ are (anti-commuting) Fermi operators ($\{c_{n\sigma}, c_{n'\sigma'}^\dagger\} = \delta_{nn'} \delta_{\sigma\sigma'}$), the anti-commutator of the r.h.s. of Eq. (A.6) together with $c_{0\sigma}$ yields $\{(\varepsilon_{0\sigma} c_{0\sigma}^\dagger + t_{0\sigma} c_{1\sigma}^\dagger), c_{0\sigma}\} = \varepsilon_{0\sigma}$. Finally, the expression for $\varepsilon_{0\sigma}$ can be obtained by evaluation of the anticommutator of the l.h.s. of Eq. (A.6) with $c_{0\sigma}$ as given in (3.13)²:

$$\varepsilon_{0\sigma} = \sum_{m=0}^{\infty} (\xi_{m\sigma}^+ u_{0m\sigma}^2 + \xi_{m\sigma}^- v_{0m\sigma}^2) \quad (\text{A.7})$$

From Eq. (A.5) we also obtain

$$t_{0\sigma} c_{1\sigma}^\dagger = \sum_{m=0}^{\infty} \left[\left(\xi_{m\sigma}^+ - \varepsilon_{0\sigma} \right) u_{0m\sigma} a_{m\sigma}^\dagger + \left(\xi_{m\sigma}^- - \varepsilon_{0\sigma} \right) v_{0m\sigma} b_{m\sigma}^\dagger \right] \quad (\text{A.8})$$

which gives immediately

$$\begin{aligned} u_{1m\sigma} &= \frac{1}{t_{0\sigma}} \left(\xi_{m\sigma}^+ - \varepsilon_{0\sigma} \right) u_{0m\sigma} \\ v_{1m\sigma} &= \frac{1}{t_{0\sigma}} \left(\xi_{m\sigma}^- - \varepsilon_{0\sigma} \right) v_{0m\sigma} \end{aligned} \quad (\text{A.9})$$

²The discrete operators $a_{n\sigma}$ and $b_{n\sigma}$ are anticommuting as well

The initial hopping matrix element $t_{0\sigma}$ can now be calculated by taking the anticommutator with the corresponding adjoint operator on both sides of Eq. (A.8):

$$t_{0\sigma} = \frac{1}{\sqrt{\xi_{0\sigma}}} \left[\sum_{m=0}^{\infty} \left(\xi_{m\sigma}^+ - \varepsilon_{0\sigma} \right)^2 \left(\gamma_{m\sigma}^+ \right)^2 + \left(\xi_{m\sigma}^- - \varepsilon_{0\sigma} \right)^2 \left(\gamma_{m\sigma}^- \right)^2 \right]^{\frac{1}{2}} \quad (\text{A.10})$$

Equations (A.4), (A.7), (A.9) and (A.10) initialize the recursion relations for the calculation of $\varepsilon_{n\sigma}$, $t_{n\sigma}$, $u_{nm\sigma}$ and $v_{nm\sigma}$. Starting with Eq. (A.5) and following the arguments as above (building anticommutators etc.) one arrives at the spin-dependent parameters of the n -th site of the Wilson chain, namely the on-site energies $\varepsilon_{n\sigma}$ and the hopping matrix elements $t_{n\sigma}$:

$$\varepsilon_{n\sigma} = \sum_{m\sigma}^{\infty} \left(\xi_{m\sigma}^+ (u_{nm\sigma})^2 + \xi_{m\sigma}^- (v_{nm\sigma})^2 \right) \quad (\text{A.11})$$

$$t_{n\sigma} = \left\{ \sum_{m=0}^{\infty} \left[\left(\xi_{m\sigma}^+ - \varepsilon_{n\sigma} \right) u_{nm\sigma} - t_{n-1\sigma} u_{n-1m\sigma} \right]^2 + \left[\left(\xi_{m\sigma}^- - \varepsilon_{n\sigma} \right) v_{nm\sigma} - t_{n-1\sigma} v_{n-1m\sigma} \right]^2 \right\}^{\frac{1}{2}} \quad (\text{A.12})$$

with the coefficients of the single-particle operator $c_{n+1\sigma}$, defined in Eq. (A.3)

$$u_{n+1m\sigma} = \frac{1}{t_{n\sigma}} \left[\left(\xi_{m\sigma}^+ - \varepsilon_{n\sigma} \right) u_{nm\sigma} - t_{n-1\sigma} u_{n-1m\sigma} \right] \quad (\text{A.13})$$

$$v_{n+1m\sigma} = \frac{1}{t_{n\sigma}} \left[\left(\xi_{m\sigma}^- - \varepsilon_{n\sigma} \right) v_{nm\sigma} - t_{n-1\sigma} v_{n-1m\sigma} \right] \quad (\text{A.14})$$

Although only the parameters of the Wilson chain $\varepsilon_{n\sigma}$ and $t_{n\sigma}$ are finally used in the iterative numerical diagonalization, also the coefficients $u_{nm\sigma}$ and $v_{nm\sigma}$ have to be determined as well, since they are required in the recursive relations of $\varepsilon_{n\sigma}$ and $t_{n\sigma}$, see Eqs. (A.11) and (A.12).

Since the mapping of the conduction band onto the Wilson chain is a unitary transformation (see Eq. (A.3)), it does not change particle-hole symmetry. A particle-hole symmetric hybridization $\Delta_{\sigma}(\varepsilon)$ therefore implies vanishing on-site energies $\varepsilon_{n\sigma}$ of the Wilson chain (A.1): $\varepsilon_{n\sigma} = 0, \forall n \in \mathbb{N}_0$. This can also be deduced from the recursion relations: For particle-hole symmetry ($\Delta_{\sigma}(\varepsilon) = \Delta_{\sigma}(-\varepsilon)$) the relations $\xi_{n\sigma}^+ = \xi_{n\sigma}^-$ and $\gamma_{n\sigma}^+ = \gamma_{n\sigma}^-$ hold, yielding $\varepsilon_{0\sigma} = 0$ (Eq. (A.7)). Then the coefficients $u_{1m\sigma}$ and $v_{1m\sigma}$ are equal (Eq. (A.9)), resulting in $\varepsilon_{1\sigma} = 0$ (Eq. (A.11)), leading to $u_{2m\sigma} = v_{2m\sigma}$ (Eqs. (A.13),(A.14)), etc. .

Due to the exponentially fast decay of the Wilson chain parameters $\varepsilon_{n\sigma}$ and $t_{n\sigma}$ (due to exponentially decaying band energies), rather advanced numerical methods are required. For the calculations in this thesis the GNU Multiple Precision Arithmetic Library (GMP) was used.

Despite the 'arbitrary' precision of the GMP, the successful convergence of the described recursion procedure could not be guaranteed for an arbitrary DoS of the CB. Especially for a rather structured CB, the resulting chain parameters $\varepsilon_{n\sigma}$ and $t_{n\sigma}$ were not decaying exponentially for large n . These problems were solved with a trick by Bulla [96]: Since (A.3) denotes a *unitary* transformation, the norm of every 'column vector' of the matrices $u_{nm\sigma}$ and $v_{nm\sigma}$ is equal to unity. Thus after every step in the recursion procedure, each coefficient $u_{nm\sigma}$ and $v_{nm\sigma}$ was re-normalized according to its norm $\sqrt{\sum_m u_{nm\sigma}^2}$ and $\sqrt{\sum_m v_{nm\sigma}^2}$, respectively. With this modification, a stable calculation of the Wilson chain parameters could be ensured.

Note that for a flat conduction band, as in the original work of Wilson [3], and for a power-law density of states (in pseudo-gap Fermi systems) [45], analytical expressions for the hopping matrix elements t_n exist. For the flat conduction electron DoS ($\Delta_\sigma(\varepsilon) = \Delta$), as also considered in Krishna-murthy *et al.*'s work [9], the hopping matrix elements are

$$t_{n\sigma} = \frac{1}{2} (1 + \Lambda^{-1}) \Lambda^{-n/2} \frac{\overbrace{1 - \Lambda^{-n-1}}^{\xi_n^K}}{\sqrt{(1 - \Lambda^{-(2n+1)})(1 - \Lambda^{-(2n+3)})}} \quad (\text{A.15})$$

(Compare the ξ_n^K to Eq. (2.15) of [9] and the $t_{n\sigma}$ to Eq. (VII.35) of [3]).

A.2 Details on the solution by iterative diagonalization

In order to solve the sequence of Hamiltonians (Eq.(3.30)) in a useful representation, one identifies the underlying symmetries of the problem. For the SIAM, Krishna-murthy *et al.* [9] used total particle number (charge) Q , total spin S and its z -component S_z . To be able to include a local magnetic field, which would lift the full spin $SU(2)$ symmetry, and to avoid Clebsch-Gordan coefficients, we use Q and S_z only to label the many-particle states. For the initial impurity Hamiltonian H_{-1} the corresponding eigenstates in the representation $|Q, S_z, r\rangle_N$ (r denoting the degeneracy) have the form

$$\begin{aligned} |-1, 0, 1\rangle_{-1} &= |0\rangle \\ |0, \sigma, 1\rangle_{-1} &= c_{-1\sigma}^\dagger |0\rangle \\ |1, 0, 1\rangle_{-1} &= c_{-1\uparrow}^\dagger c_{-1\downarrow}^\dagger |0\rangle \end{aligned}$$

with the eigenenergies

$$\begin{aligned} E_{-1}(-1, 0, 1) &= 0 \\ E_{-1}(0, \sigma, 1) &= \frac{1}{\Lambda} \varepsilon_d \\ E_{-1}(1, 0, 1) &= \frac{1}{\Lambda} (2\varepsilon_d + U) \end{aligned}$$

To set up a general procedure the following notation is used

$$\begin{aligned} |Q, S_z, r; 0\rangle &= |Q, S_z, r\rangle_N \\ |Q, S_z, r; \uparrow\rangle &= c_{N+1\uparrow}^\dagger |Q, S_z, r\rangle_N \\ |Q, S_z, r; \downarrow\rangle &= c_{N+1\downarrow}^\dagger |Q, S_z, r\rangle_N \\ |Q, S_z, r; \uparrow\downarrow\rangle &= c_{N+1\uparrow}^\dagger c_{N+1\downarrow}^\dagger |Q, S_z, r\rangle_N \end{aligned}$$

with which we can, starting from the eigenstates of H_N , which we write as $|Q, S_z, r\rangle_N$, construct basis states of H_{N+1} that are also eigenstates of Q_{N+1} and $(S_z)_{N+1}$:

$$\begin{aligned} |Q, S_z, r; 1\rangle_{N+1} &= |Q + 1, S_z, r; 0\rangle \\ |Q, S_z, r; 2\rangle_{N+1} &= |Q, S_z - \frac{1}{2}, r; \uparrow\rangle \\ |Q, S_z, r; 3\rangle_{N+1} &= |Q, S_z + \frac{1}{2}, r; \downarrow\rangle \\ |Q, S_z, r; 4\rangle_{N+1} &= |Q - 1, S_z, r; \uparrow\downarrow\rangle \end{aligned} \quad (\text{A.16})$$

This basis is used to set up the Hamiltonian matrix of H_{N+1} in each (Q, S_z) -subspace:

$$\begin{aligned} H_{Q, S_z}(ri, r'j) &= {}_{N+1}\langle Q, S_z, r; i | H_{N+1} | Q, S_z, r'; j \rangle_{N+1} \\ &= \sqrt{\Lambda} {}_{N+1}\langle Q, S_z, r; i | H_N | Q, S_z, r'; j \rangle_{N+1} \\ &+ \Lambda^{N/2} \sum_{\sigma} \varepsilon_{N+1\sigma} {}_{N+1}\langle Q, S_z, r; i | c_{N+1\sigma}^\dagger c_{N+1\sigma} | Q, S_z, r'; j \rangle_{N+1} \\ &+ \Lambda^{N/2} \sum_{\sigma} t_{N\sigma} {}_{N+1}\langle Q, S_z, r; i | \left(c_{N\sigma}^\dagger c_{N+1\sigma} + c_{N+1\sigma}^\dagger c_{N\sigma} \right) | Q, S_z, r'; j \rangle_{N+1} \end{aligned} \quad (\text{A.17})$$

The first term simply denotes the eigenenergies of the preceding NRG iteration:

$$\begin{aligned} &{}_{N+1}\langle Q, S_z, r; i | H_N | Q, S_z, r'; j \rangle_{N+1} \\ &= \delta_{rr'} \begin{cases} E_N(Q + 1, S_z, r) & \text{for } i = j = 1 \\ E_N(Q, S_z - \frac{1}{2}, r) & \text{for } i = j = 2 \\ E_N(Q, S_z + \frac{1}{2}, r) & \text{for } i = j = 3 \\ E_N(Q - 1, S_z, r) & \text{for } i = j = 4 \end{cases} \end{aligned}$$

In absence of particle-hole symmetry, also the on-site energies $\varepsilon_{N\sigma}$ contribute:

$$\begin{aligned} & {}_{N+1}\langle Q, S_z, r; i | c_{N+1\sigma}^\dagger c_{N+1\sigma} | Q, S_z, r'; j \rangle_{N+1} \\ &= \begin{cases} 0 & \text{for } i = j = 1 \\ \delta_{rr'} \delta_{\sigma\uparrow} & \text{for } i = j = 2 \\ \delta_{rr'} \delta_{\sigma\downarrow} & \text{for } i = j = 3 \\ \delta_{rr'} & \text{for } i = j = 4 \end{cases} \end{aligned}$$

Finally, the off-diagonal terms of Eq. (A.17) have to be computed. There are only certain combinations of (i, j) for which the corresponding matrix element is non-zero. E.g. for $(i, j) = (1, 2)$ one finds:

$$\begin{aligned} & {}_{N+1}\langle Q, S_z, r; 1 | c_{N\uparrow}^\dagger c_{N+1\uparrow} | Q, S_z, r'; 2 \rangle_{N+1} \\ &= {}_N\langle Q + 1, S_z, r | c_{N\uparrow}^\dagger \underbrace{c_{N+1\uparrow} c_{N+1\uparrow}^\dagger}_{=1} | Q, S_z - \frac{1}{2}, r' \rangle_N \\ &= {}_N\langle Q + 1, S_z, r | c_{N\uparrow}^\dagger | Q, S_z - \frac{1}{2}, r' \rangle_N \end{aligned}$$

Due to fermionic anti-commutation rules of the $c_{N\sigma}$ there may arise signs for other combinations (i, j) . All the non-vanishing off-diagonal terms of Eq. (A.17) are:

$$\begin{aligned} {}_{N+1}\langle Q, S_z, r; 1 | c_{N\uparrow}^\dagger c_{N+1\uparrow} | Q, S_z, r'; 2 \rangle_{N+1} &= {}_N\langle Q + 1, S_z, r | c_{N\uparrow}^\dagger | Q, S_z - \frac{1}{2}, r' \rangle_N \\ {}_{N+1}\langle Q, S_z, r; 3 | c_{N\uparrow}^\dagger c_{N+1\uparrow} | Q, S_z, r'; 4 \rangle_{N+1} &= -{}_N\langle Q, S_z + \frac{1}{2}, r | c_{N\uparrow}^\dagger | Q - 1, S_z, r' \rangle_N \\ {}_{N+1}\langle Q, S_z, r; 1 | c_{N\downarrow}^\dagger c_{N+1\downarrow} | Q, S_z, r'; 3 \rangle_{N+1} &= {}_N\langle Q + 1, S_z, r | c_{N\downarrow}^\dagger | Q, S_z + \frac{1}{2}, r' \rangle_N \\ {}_{N+1}\langle Q, S_z, r; 2 | c_{N\downarrow}^\dagger c_{N+1\downarrow} | Q, S_z, r'; 4 \rangle_{N+1} &= {}_N\langle Q, S_z - \frac{1}{2}, r | c_{N\downarrow}^\dagger | Q - 1, S_z, r' \rangle_N \end{aligned}$$

Diagonalization of the matrices $H_{Q,S_z}(ri, r'j)$ yields the eigenvalues $E_{N+1}(Q, S_z, w)$ and the eigenstates

$$|Q, S_z, w\rangle_{N+1} = \sum_{ri} U_{Q,S_z}(w, ri) |Q, S_z, r; i\rangle_{N+1} \quad (\text{A.18})$$

The knowledge of all unitary transformation matrices U_{Q,S_z} is then sufficient to calculate the matrix elements necessary to set up the Hamiltonian matrices in the following step ($N + 2$):

$$\begin{aligned} & {}_{N+1}\langle Q, S_z, w | c_{N+1\uparrow}^\dagger | Q', S'_z, w' \rangle_{N+1} \\ &= \sum_r \left[U_{Q,S_z}(w, r2) U_{Q-1, S_z - \frac{1}{2}}(w', r1) + U_{Q,S_z}(w, r4) U_{Q-1, S_z - \frac{1}{2}}(w', r3) \right] \end{aligned}$$

$$\begin{aligned}
& {}_{N+1}\langle Q, S_z, w | c_{N+1\downarrow}^\dagger | Q', S'_z, w' \rangle_{N+1} \\
&= \sum_r \left[U_{Q, S_z}(w, r3) U_{Q-1, S_z+\frac{1}{2}}(w', r1) - U_{Q, S_z}(w, r4) U_{Q-1, S_z+\frac{1}{2}}(w', r2) \right]
\end{aligned}$$

Every NRG iteration yields the eigenenergies and eigenstates of the corresponding Hamiltonian H_N . This knowledge enables us to calculate physical properties (as e.g. static susceptibility, free energy, etc.) at a scale $\omega_N \sim \Lambda^{-(N-1)/2} D$. The calculation of dynamical properties such as the impurity spectral function $A_{d\sigma}(\omega) = -\frac{1}{\pi} \text{Im}(G_{d\sigma}(\omega))$ requires computation of the impurity matrix elements

$${}_{N+1}\langle Q, S_z, w | c_{-1\sigma}^\dagger | Q', S'_z, w' \rangle_{N+1}$$

Therefore, using the unitary transformation (A.18), the spectral function can be represented in the basis (A.16):

$$\begin{aligned}
& {}_{N+1}\langle Q, S_z, w | c_{-1\sigma}^\dagger | Q', S'_z, w' \rangle_{N+1} \\
&= \sum_{rr'} \sum_{pp'} U_{Q, S_z}^T(w, rp) U_{Q', S'_z}(w', r'p') {}_{N+1}\langle Q, S_z, r; p | c_{-1\sigma}^\dagger | Q', S'_z, r'; p' \rangle_{N+1}
\end{aligned}$$

Evaluation of the matrix elements yields:

$$\begin{aligned}
{}_{N+1}\langle Q, S_z, r; 1 | c_{-1\sigma}^\dagger | Q', S'_z, r'; 1 \rangle_{N+1} &= {}_N\langle Q+1, S_z, r | c_{-1\sigma}^\dagger | Q, S_z - \sigma, r' \rangle_N \\
{}_{N+1}\langle Q, S_z, r; 2 | c_{-1\sigma}^\dagger | Q', S'_z, r'; 2 \rangle_{N+1} &= -{}_N\langle Q, S_z - \frac{1}{2}, r | c_{-1\sigma}^\dagger | Q-1, S_z - \frac{1}{2} - \sigma, r' \rangle_N \\
{}_{N+1}\langle Q, S_z, r; 3 | c_{-1\sigma}^\dagger | Q', S'_z, r'; 3 \rangle_{N+1} &= -{}_N\langle Q, S_z + \frac{1}{2}, r | c_{-1\sigma}^\dagger | Q-1, S_z + \frac{1}{2} - \sigma, r' \rangle_N \\
{}_{N+1}\langle Q, S_z, r; 4 | c_{-1\sigma}^\dagger | Q', S'_z, r'; 4 \rangle_{N+1} &= {}_N\langle Q-1, S_z, r | c_{-1\sigma}^\dagger | Q-2, S_z - \sigma, r' \rangle_N
\end{aligned}$$

All other matrix elements are zero.

The initial values for the matrix elements are

$$\begin{aligned}
-1\langle 0, \frac{1}{2}, 1 | c_{-1\uparrow}^\dagger | -1, 0, 1 \rangle_{-1} &= 1 \\
-1\langle 1, 0, 1 | c_{-1\uparrow}^\dagger | 0, -\frac{1}{2}, 1 \rangle_{-1} &= 1 \\
-1\langle 0, -\frac{1}{2}, 1 | c_{-1\downarrow}^\dagger | -1, 0, 1 \rangle_{-1} &= 1 \\
-1\langle 1, 0, 1 | c_{-1\downarrow}^\dagger | 0, \frac{1}{2}, 1 \rangle_{-1} &= -1
\end{aligned}$$

Appendix B

Details on the two-channel Kondo (2CK) NRG

This chapter contains details on the 2CK calculations of chapter 4. To diagonalize the 2CK Hamiltonian (Eq. (4.1)), the following discretized Hamiltonian in the N^{th} iteration (Eq. (4.4)) is used:

$$H_N = \Lambda^{(N-1)/2} \left[\sum_{n=0, \alpha, \sigma}^{N-1} t_n \left(f_{n\alpha\sigma}^\dagger f_{n+1\alpha\sigma} + h.c. \right) + \sum_{\alpha} J_{\alpha} f_{0\alpha\sigma}^\dagger \vec{\sigma}_{\sigma\sigma'} f_{0\alpha\sigma'} \cdot \vec{S}_I \right]$$

If one denotes the eigenstates of H_N with $|Q, S_{tot}^z, S_{ch}^z, r\rangle_N$, one can construct the following 16 states:

$$\begin{aligned} |Q, S_{tot}^z, S_{ch}^z, r; 0, 0\rangle &= |Q, S_{tot}^z, S_{ch}^z, r\rangle_N \\ |Q, S_{tot}^z, S_{ch}^z, r; \uparrow, 0\rangle &= f_{N+1,+, \uparrow}^\dagger |Q, S_{tot}^z, S_{ch}^z, r\rangle_N \\ |Q, S_{tot}^z, S_{ch}^z, r; \downarrow, 0\rangle &= f_{N+1,+, \downarrow}^\dagger |Q, S_{tot}^z, S_{ch}^z, r\rangle_N \\ |Q, S_{tot}^z, S_{ch}^z, r; \uparrow\downarrow, 0\rangle &= f_{N+1,+, \uparrow}^\dagger f_{N+1,+, \downarrow}^\dagger |Q, S_{tot}^z, S_{ch}^z, r\rangle_N \\ |Q, S_{tot}^z, S_{ch}^z, r; 0, \uparrow\rangle &= f_{N+1,-, \uparrow}^\dagger |Q, S_{tot}^z, S_{ch}^z, r\rangle_N \\ |Q, S_{tot}^z, S_{ch}^z, r; \uparrow, \uparrow\rangle &= f_{N+1,+, \uparrow}^\dagger f_{N+1,-, \uparrow}^\dagger |Q, S_{tot}^z, S_{ch}^z, r\rangle_N \\ |Q, S_{tot}^z, S_{ch}^z, r; \downarrow, \uparrow\rangle &= f_{N+1,+, \downarrow}^\dagger f_{N+1,-, \uparrow}^\dagger |Q, S_{tot}^z, S_{ch}^z, r\rangle_N \\ |Q, S_{tot}^z, S_{ch}^z, r; \uparrow\downarrow, \uparrow\rangle &= f_{N+1,+, \uparrow}^\dagger f_{N+1,+, \downarrow}^\dagger f_{N+1,-, \uparrow}^\dagger |Q, S_{tot}^z, S_{ch}^z, r\rangle_N \\ |Q, S_{tot}^z, S_{ch}^z, r; 0, \downarrow\rangle &= f_{N+1,-, \downarrow}^\dagger |Q, S_{tot}^z, S_{ch}^z, r\rangle_N \\ |Q, S_{tot}^z, S_{ch}^z, r; \uparrow, \downarrow\rangle &= f_{N+1,+, \uparrow}^\dagger f_{N+1,-, \downarrow}^\dagger |Q, S_{tot}^z, S_{ch}^z, r\rangle_N \\ |Q, S_{tot}^z, S_{ch}^z, r; \downarrow, \downarrow\rangle &= f_{N+1,+, \downarrow}^\dagger f_{N+1,-, \downarrow}^\dagger |Q, S_{tot}^z, S_{ch}^z, r\rangle_N \\ |Q, S_{tot}^z, S_{ch}^z, r; \uparrow\downarrow, \downarrow\rangle &= f_{N+1,+, \uparrow}^\dagger f_{N+1,+, \downarrow}^\dagger f_{N+1,-, \downarrow}^\dagger |Q, S_{tot}^z, S_{ch}^z, r\rangle_N \\ |Q, S_{tot}^z, S_{ch}^z, r; 0, \uparrow\downarrow\rangle &= f_{N+1,-, \uparrow}^\dagger f_{N+1,-, \downarrow}^\dagger |Q, S_{tot}^z, S_{ch}^z, r\rangle_N \\ |Q, S_{tot}^z, S_{ch}^z, r; \uparrow, \uparrow\downarrow\rangle &= f_{N+1,+, \uparrow}^\dagger f_{N+1,-, \uparrow}^\dagger f_{N+1,-, \downarrow}^\dagger |Q, S_{tot}^z, S_{ch}^z, r\rangle_N \\ |Q, S_{tot}^z, S_{ch}^z, r; \downarrow, \uparrow\downarrow\rangle &= f_{N+1,+, \downarrow}^\dagger f_{N+1,-, \uparrow}^\dagger f_{N+1,-, \downarrow}^\dagger |Q, S_{tot}^z, S_{ch}^z, r\rangle_N \\ |Q, S_{tot}^z, S_{ch}^z, r; \uparrow\downarrow, \uparrow\downarrow\rangle &= f_{N+1,+, \uparrow}^\dagger f_{N+1,+, \downarrow}^\dagger f_{N+1,-, \uparrow}^\dagger f_{N+1,-, \downarrow}^\dagger |Q, S_{tot}^z, S_{ch}^z, r\rangle_N \end{aligned}$$

Ordered with respect to their quantumnumbers and labeled with an index i these 16 states are illustrated in table B.1:

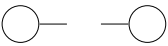
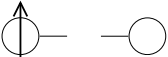
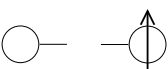
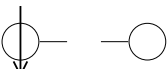
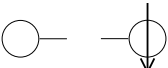
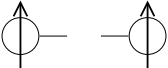
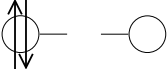
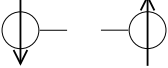
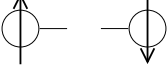
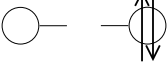
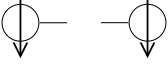

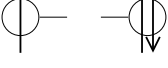
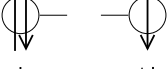
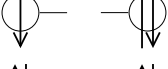
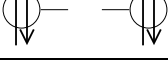
$ i\rangle$		(Q, S_{tot}^z, S_{ch}^z)
$ 1\rangle$		$(-2, 0, 0)$
$ 2\rangle$		$(-1, \frac{1}{2}, \frac{1}{2})$
$ 3\rangle$		$(-1, \frac{1}{2}, -\frac{1}{2})$
$ 4\rangle$		$(-1, -\frac{1}{2}, \frac{1}{2})$
$ 5\rangle$		$(-1, -\frac{1}{2}, -\frac{1}{2})$
$ 6\rangle$		$(0, 1, 0)$
$ 7\rangle$		$(0, 0, 1)$
$ 8\rangle$		$(0, 0, 0)$
$ 9\rangle$		$(0, 0, 0)$
$ 10\rangle$		$(0, 0, -1)$
$ 11\rangle$		$(0, -1, 0)$
$ 12\rangle$		$(1, \frac{1}{2}, \frac{1}{2})$
$ 13\rangle$		$(1, \frac{1}{2}, -\frac{1}{2})$
$ 14\rangle$		$(1, -\frac{1}{2}, \frac{1}{2})$
$ 15\rangle$		$(1, -\frac{1}{2}, -\frac{1}{2})$
$ 16\rangle$		$(2, 0, 0)$

Table B.1: These 16 combinations form a basis for one shell of a 2CK Wilson chain.

Note that the states $|8\rangle$ and $|9\rangle$ have the same quantum numbers and thus should carry an additional label, e. g. $r = 1, 2$. The program distinguishes the 2 states according to their index i .

Using these 16 states, one forms the following basis states of H_{N+1} , which are also eigenstates of $(Q)_{N+1}, (S_{tot}^z)_{N+1}, (S_{ch}^z)_{N+1}$:

$$\begin{aligned}
|Q, S_{tot}^z, S_{ch}^z, r;1\rangle_{N+1} &= |Q + 2, S_{tot}^z, S_{ch}^z, r;0, 0\rangle_N \\
|Q, S_{tot}^z, S_{ch}^z, r;2\rangle_{N+1} &= |Q + 1, S_{tot}^z - \frac{1}{2}, S_{ch}^z - \frac{1}{2}, r; \uparrow, 0\rangle_N \\
|Q, S_{tot}^z, S_{ch}^z, r;3\rangle_{N+1} &= |Q + 1, S_{tot}^z - \frac{1}{2}, S_{ch}^z + \frac{1}{2}, r;0, \uparrow\rangle_N \\
|Q, S_{tot}^z, S_{ch}^z, r;4\rangle_{N+1} &= |Q + 1, S_{tot}^z + \frac{1}{2}, S_{ch}^z - \frac{1}{2}, r; \downarrow, 0\rangle_N \\
|Q, S_{tot}^z, S_{ch}^z, r;5\rangle_{N+1} &= |Q + 1, S_{tot}^z + \frac{1}{2}, S_{ch}^z + \frac{1}{2}, r;0, \downarrow\rangle_N \\
|Q, S_{tot}^z, S_{ch}^z, r;6\rangle_{N+1} &= |Q, S_{tot}^z - 1, S_{ch}^z, r; \uparrow, \uparrow\rangle_N \\
|Q, S_{tot}^z, S_{ch}^z, r;7\rangle_{N+1} &= |Q, S_{tot}^z, S_{ch}^z - 1, r; \uparrow \downarrow, 0\rangle_N \\
|Q, S_{tot}^z, S_{ch}^z, r;8\rangle_{N+1} &= |Q, S_{tot}^z, S_{ch}^z, r; \downarrow, \uparrow\rangle_N \\
|Q, S_{tot}^z, S_{ch}^z, r;9\rangle_{N+1} &= |Q, S_{tot}^z, S_{ch}^z, r; \uparrow, \downarrow\rangle_N \\
|Q, S_{tot}^z, S_{ch}^z, r;10\rangle_{N+1} &= |Q, S_{tot}^z, S_{ch}^z + 1, r;0, \uparrow \downarrow\rangle_N \\
|Q, S_{tot}^z, S_{ch}^z, r;11\rangle_{N+1} &= |Q, S_{tot}^z + 1, S_{ch}^z, r; \downarrow, \downarrow\rangle_N \\
|Q, S_{tot}^z, S_{ch}^z, r;12\rangle_{N+1} &= |Q - 1, S_{tot}^z - \frac{1}{2}, S_{ch}^z - \frac{1}{2}, r; \uparrow \downarrow, \uparrow\rangle_N \\
|Q, S_{tot}^z, S_{ch}^z, r;13\rangle_{N+1} &= |Q - 1, S_{tot}^z - \frac{1}{2}, S_{ch}^z + \frac{1}{2}, r; \uparrow, \uparrow \downarrow\rangle_N \\
|Q, S_{tot}^z, S_{ch}^z, r;14\rangle_{N+1} &= |Q - 1, S_{tot}^z + \frac{1}{2}, S_{ch}^z + \frac{1}{2}, r; \uparrow \downarrow, \downarrow\rangle_N \\
|Q, S_{tot}^z, S_{ch}^z, r;15\rangle_{N+1} &= |Q - 1, S_{tot}^z + \frac{1}{2}, S_{ch}^z + \frac{1}{2}, r; \downarrow, \uparrow \downarrow\rangle_N \\
|Q, S_{tot}^z, S_{ch}^z, r;16\rangle_{N+1} &= |Q - 2, S_{tot}^z, S_{ch}^z, r; \uparrow \downarrow, \uparrow \downarrow\rangle_N
\end{aligned}$$

This basis is used to set up the Hamiltonian matrices of H_{N+1} for each subspace (Q, S_{tot}^z, S_{ch}^z) :

$$\begin{aligned}
H_{Q, S_{tot}^z, S_{ch}^z}(ri, r'j) &= \tag{B.1} \\
&= {}_{N+1}\langle Q, S_{tot}^z, S_{ch}^z, r; i | H_{N+1} | Q, S_{tot}^z, S_{ch}^z, r'; j \rangle_{N+1} \\
&= \sqrt{\Lambda}_{N+1} \langle Q, S_{tot}^z, S_{ch}^z, r; i | H_N | Q, S_{tot}^z, S_{ch}^z, r'; j \rangle_{N+1} \\
&+ \Lambda^{N/2} \sum_{\alpha\sigma} t_{N+1} \langle Q, S_{tot}^z, S_{ch}^z, r; i | (f_{N\alpha\sigma}^\dagger f_{N+1\alpha\sigma} + h.c.) | Q, S_{tot}^z, S_{ch}^z, r'; j \rangle_{N+1}
\end{aligned}$$

The first term of Eq. (B.1) can simply be calculated using the eigenenergies of the

previous step:

$$\begin{aligned}
& {}_{N+1}\langle Q, S_{tot}^z, S_{ch}^z, r; i | H_N | Q, S_{tot}^z, S_{ch}^z, r'; j \rangle_{N+1} = \\
& = \delta_{rr'} \left\{ \begin{array}{ll}
E_N(Q+2, S_{tot}^z, S_{ch}^z, r) & \text{for } i=j=1 \\
E_N(Q+1, S_{tot}^z - \frac{1}{2}, S_{ch}^z - \frac{1}{2}, r) & \text{for } i=j=2 \\
E_N(Q+1, S_{tot}^z - \frac{1}{2}, S_{ch}^z + \frac{1}{2}, r) & \text{for } i=j=3 \\
E_N(Q+1, S_{tot}^z + \frac{1}{2}, S_{ch}^z - \frac{1}{2}, r) & \text{for } i=j=4 \\
E_N(Q+1, S_{tot}^z + \frac{1}{2}, S_{ch}^z + \frac{1}{2}, r) & \text{for } i=j=5 \\
E_N(Q, S_{tot}^z - 1, S_{ch}^z, r) & \text{for } i=j=6 \\
E_N(Q, S_{tot}^z, S_{ch}^z - 1, r) & \text{for } i=j=7 \\
E_N(Q, S_{tot}^z, S_{ch}^z, r) & \text{for } i=j=8 \\
E_N(Q, S_{tot}^z, S_{ch}^z, r) & \text{for } i=j=9 \\
E_N(Q, S_{tot}^z, S_{ch}^z + 1, r) & \text{for } i=j=10 \\
E_N(Q, S_{tot}^z + 1, S_{ch}^z, r) & \text{for } i=j=11 \\
E_N(Q-1, S_{tot}^z - \frac{1}{2}, S_{ch}^z - \frac{1}{2}, r) & \text{for } i=j=12 \\
E_N(Q-1, S_{tot}^z - \frac{1}{2}, S_{ch}^z + \frac{1}{2}, r) & \text{for } i=j=13 \\
E_N(Q-1, S_{tot}^z + \frac{1}{2}, S_{ch}^z + \frac{1}{2}, r) & \text{for } i=j=14 \\
E_N(Q-1, S_{tot}^z + \frac{1}{2}, S_{ch}^z - \frac{1}{2}, r) & \text{for } i=j=15 \\
E_N(Q-2, S_{tot}^z, S_{ch}^z, r) & \text{for } i=j=16
\end{array} \right.
\end{aligned}$$

For the second term of Eq. (B.1), only certain combinations of (i, j) have non-vanishing matrix elements. E.g. for $(\sigma = \uparrow, \alpha = +)$ we get for $(i, j) = (1, 2)$:

$$\begin{aligned}
& {}_{N+1}\langle Q, S_{tot}^z, S_{ch}^z, r; 1 | f_{N,+,\uparrow}^\dagger f_{N+1,+,\uparrow} | Q, S_{tot}^z, S_{ch}^z, r'; 2 \rangle_{N+1} \\
& = {}_N\langle Q+2, S_{tot}^z, S_{ch}^z, r | f_{N,+,\uparrow}^\dagger \underbrace{f_{N+1,+,\uparrow} f_{N+1,+,\uparrow}^\dagger}_{=1} | Q+1, S_{tot}^z - \frac{1}{2}, S_{ch}^z - \frac{1}{2}, r' \rangle_N \\
& = {}_N\langle Q+2, S_{tot}^z, S_{ch}^z, r | f_{N,+,\uparrow}^\dagger | Q+1, S_{tot}^z - \frac{1}{2}, S_{ch}^z - \frac{1}{2}, r' \rangle_N
\end{aligned}$$

For other possible combinations of (i, j) there may arise signs due to fermionic anticommutation rules of the $f_{N\alpha\sigma}$. The following tables list all non-zero off-diagonal matrix elements occurring in Eq. (B.1).

$$(\sigma = \uparrow, \alpha = +)$$

(i,j)	matrix element
(1,2)	$N \langle Q + 2, S_{tot}^z, S_{ch}^z, r f_{N,+,\uparrow}^\dagger Q + 1, S_{tot}^z - \frac{1}{2}, S_{ch}^z - \frac{1}{2}, r' \rangle_N$
(4,7)	$-N \langle Q + 1, S_{tot}^z + \frac{1}{2}, S_{ch}^z - \frac{1}{2}, r f_{N,+,\uparrow}^\dagger Q, S_{tot}^z, S_{ch}^z - 1, r' \rangle_N$
(3,6)	$-N \langle Q + 1, S_{tot}^z - \frac{1}{2}, S_{ch}^z + \frac{1}{2}, r f_{N,+,\uparrow}^\dagger Q, S_{tot}^z - 1, S_{ch}^z, r' \rangle_N$
(8,12)	$N \langle Q, S_{tot}^z, S_{ch}^z, r f_{N,+,\uparrow}^\dagger Q - 1, S_{tot}^z - \frac{1}{2}, S_{ch}^z - \frac{1}{2}, r' \rangle_N$
(5,9)	$-N \langle Q + 1, S_{tot}^z + \frac{1}{2}, S_{ch}^z + \frac{1}{2}, r f_{N,+,\uparrow}^\dagger Q, S_{tot}^z, S_{ch}^z, r' \rangle_N$
(11,14)	$N \langle Q, S_{tot}^z + 1, S_{ch}^z, r f_{N,+,\uparrow}^\dagger Q - 1, S_{tot}^z + \frac{1}{2}, S_{ch}^z - \frac{1}{2}, r' \rangle_N$
(10,13)	$N \langle Q, S_{tot}^z, S_{ch}^z + 1, r f_{N,+,\uparrow}^\dagger Q - 1, S_{tot}^z - \frac{1}{2}, S_{ch}^z + \frac{1}{2}, r' \rangle_N$
(15,16)	$-N \langle Q - 1, S_{tot}^z + \frac{1}{2}, S_{ch}^z + \frac{1}{2}, r f_{N,+,\uparrow}^\dagger Q - 2, S_{tot}^z, S_{ch}^z, r' \rangle_N$

$$(\sigma = \downarrow, \alpha = +)$$

(i,j)	matrix element
(1,4)	$N \langle Q + 2, S_{tot}^z, S_{ch}^z, r f_{N,+,\downarrow}^\dagger Q + 1, S_{tot}^z + \frac{1}{2}, S_{ch}^z - \frac{1}{2}, r' \rangle_N$
(2,7)	$N \langle Q + 1, S_{tot}^z - \frac{1}{2}, S_{ch}^z - \frac{1}{2}, r f_{N,+,\downarrow}^\dagger Q, S_{tot}^z, S_{ch}^z - 1, r' \rangle_N$
(3,8)	$-N \langle Q + 1, S_{tot}^z - \frac{1}{2}, S_{ch}^z + \frac{1}{2}, r f_{N,+,\downarrow}^\dagger Q, S_{tot}^z, S_{ch}^z, r' \rangle_N$
(6,12)	$-N \langle Q, S_{tot}^z - 1, S_{ch}^z, r f_{N,+,\downarrow}^\dagger Q - 1, S_{tot}^z - \frac{1}{2}, S_{ch}^z - \frac{1}{2}, r' \rangle_N$
(5,11)	$-N \langle Q + 1, S_{tot}^z + \frac{1}{2}, S_{ch}^z + \frac{1}{2}, r f_{N,+,\downarrow}^\dagger Q, S_{tot}^z + 1, S_{ch}^z, r' \rangle_N$
(9,14)	$-N \langle Q, S_{tot}^z, S_{ch}^z, r f_{N,+,\downarrow}^\dagger Q - 1, S_{tot}^z + \frac{1}{2}, S_{ch}^z - \frac{1}{2}, r' \rangle_N$
(10,15)	$N \langle Q, S_{tot}^z, S_{ch}^z + 1, r f_{N,+,\downarrow}^\dagger Q - 1, S_{tot}^z + \frac{1}{2}, S_{ch}^z + \frac{1}{2}, r' \rangle_N$
(13,16)	$N \langle Q - 1, S_{tot}^z - \frac{1}{2}, S_{ch}^z + \frac{1}{2}, r f_{N,+,\downarrow}^\dagger Q - 2, S_{tot}^z, S_{ch}^z, r' \rangle_N$

$$(\sigma = \uparrow, \alpha = -)$$

(i,j)	matrix element
(1,3)	$N \langle Q + 2, S_{tot}^z, S_{ch}^z, r f_{N,-,\uparrow}^\dagger Q + 1, S_{tot}^z - \frac{1}{2}, S_{ch}^z + \frac{1}{2}, r' \rangle_N$
(2,6)	$N \langle Q + 1, S_{tot}^z - \frac{1}{2}, S_{ch}^z - \frac{1}{2}, r f_{N,-,\uparrow}^\dagger Q, S_{tot}^z - 1, S_{ch}^z, r' \rangle_N$
(4,8)	$N \langle Q + 1, S_{tot}^z + \frac{1}{2}, S_{ch}^z - \frac{1}{2}, r f_{N,-,\uparrow}^\dagger Q, S_{tot}^z, S_{ch}^z, r' \rangle_N$
(7,12)	$N \langle Q, S_{tot}^z, S_{ch}^z - 1, r f_{N,-,\uparrow}^\dagger Q - 1, S_{tot}^z - \frac{1}{2}, S_{ch}^z - \frac{1}{2}, r' \rangle_N$
(5,10)	$-N \langle Q + 1, S_{tot}^z + \frac{1}{2}, S_{ch}^z + \frac{1}{2}, r f_{N,-,\uparrow}^\dagger Q, S_{tot}^z, S_{ch}^z + 1, r' \rangle_N$
(9,13)	$-N \langle Q, S_{tot}^z, S_{ch}^z, r f_{N,-,\uparrow}^\dagger Q - 1, S_{tot}^z - \frac{1}{2}, S_{ch}^z + \frac{1}{2}, r' \rangle_N$
(11,15)	$-N \langle Q, S_{tot}^z + 1, S_{ch}^z, r f_{N,-,\uparrow}^\dagger Q - 1, S_{tot}^z + \frac{1}{2}, S_{ch}^z + \frac{1}{2}, r' \rangle_N$
(14,16)	$-N \langle Q - 1, S_{tot}^z + \frac{1}{2}, S_{ch}^z - \frac{1}{2}, r f_{N,-,\uparrow}^\dagger Q - 2, S_{tot}^z, S_{ch}^z, r' \rangle_N$

$$\boxed{(\sigma = \downarrow, \alpha = -)}$$

(i,j)	matrix element
(1,5)	${}_N\langle Q+2, S_{tot}^z, S_{ch}^z, r f_{N,-,\downarrow}^\dagger Q+1, S_{tot}^z + \frac{1}{2}, S_{ch}^z + \frac{1}{2}, r' \rangle_N$
(2,9)	${}_N\langle Q+1, S_{tot}^z - \frac{1}{2}, S_{ch}^z - \frac{1}{2}, r f_{N,-,\downarrow}^\dagger Q, S_{tot}^z, S_{ch}^z, r' \rangle_N$
(4,11)	${}_N\langle Q+1, S_{tot}^z + \frac{1}{2}, S_{ch}^z - \frac{1}{2}, r f_{N,-,\downarrow}^\dagger Q, S_{tot}^z + 1, S_{ch}^z, r' \rangle_N$
(7,14)	${}_N\langle Q, S_{tot}^z, S_{ch}^z - 1, r f_{N,-,\downarrow}^\dagger Q-1, S_{tot}^z + \frac{1}{2}, S_{ch}^z - \frac{1}{2}, r' \rangle_N$
(3,10)	${}_N\langle Q+1, S_{tot}^z - \frac{1}{2}, S_{ch}^z + \frac{1}{2}, r f_{N,-,\downarrow}^\dagger Q, S_{tot}^z, S_{ch}^z + 1, r' \rangle_N$
(6,13)	${}_N\langle Q, S_{tot}^z - 1, S_{ch}^z, r f_{N,-,\downarrow}^\dagger Q-1, S_{tot}^z - \frac{1}{2}, S_{ch}^z + \frac{1}{2}, r' \rangle_N$
(8,15)	${}_N\langle Q, S_{tot}^z, S_{ch}^z, r f_{N,-,\downarrow}^\dagger Q-1, S_{tot}^z + \frac{1}{2}, S_{ch}^z + \frac{1}{2}, r' \rangle_N$
(12,16)	${}_N\langle Q-1, S_{tot}^z - \frac{1}{2}, S_{ch}^z - \frac{1}{2}, r f_{N,-,\downarrow}^\dagger Q-2, S_{tot}^z, S_{ch}^z, r' \rangle_N$

Diagonalization of the matrices $H_{Q, S_{tot}^z, S_{ch}^z}(ri, r'j)$ yields the eigenvalues $E_{N+1}(Q, S_{tot}^z, S_{ch}^z, w)$ and the eigenstates

$$|Q, S_{tot}^z, S_{ch}^z, w\rangle_{N+1} = \sum_{ri} U_{Q, S_{tot}^z, S_{ch}^z}(w, ri) |Q, S_{tot}^z, S_{ch}^z, r; i\rangle_{N+1} \quad (\text{B.2})$$

To set up the Hamiltonian matrices in the following step ($N+2$), the matrix elements

$$\begin{aligned} & {}_{N+1}\langle Q, S_{tot}^z, S_{ch}^z, w | f_{N+1, \alpha, \sigma}^\dagger | Q', S_{tot}'^z, S_{ch}'^z, w' \rangle_{N+1} \\ &= \sum_{ri, r'i'} U_{Q, S_{tot}^z, S_{ch}^z}^\top(w, ri) U_{Q', S_{tot}'^z, S_{ch}'^z}(w', r'i') {}_{N+1}\langle Q, S_{tot}^z, S_{ch}^z, r; i | f_{N+1, \alpha, \sigma}^\dagger | Q', S_{tot}'^z, S_{ch}'^z, r'; i' \rangle_{N+1} \end{aligned}$$

are required. E.g. for $\alpha = +, \sigma = \uparrow$ and $(i, j) = (2, 1)$:

$$\begin{aligned} & {}_{N+1}\langle Q, S_{tot}^z, S_{ch}^z, r; 2 | f_{N+1, +, \uparrow}^\dagger | Q', S_{tot}'^z, S_{ch}'^z, r'; 1 \rangle_{N+1} \\ &= {}_N\langle Q+1, S_{tot}^z - \frac{1}{2}, S_{ch}^z - \frac{1}{2}, r | \underbrace{f_{N+1, +, \uparrow}^\dagger f_{N+1, +, \uparrow}^\dagger}_{=1} | Q'+2, S_{tot}'^z, S_{ch}'^z, r' \rangle_N \\ &= \delta_{Q, Q'+1} \delta_{S_{tot}^z - \frac{1}{2}, S_{tot}'^z} \delta_{S_{ch}^z - \frac{1}{2}, S_{ch}'^z} \delta_{rr'} \end{aligned}$$

This results in the following operators which can be calculated with the knowledge of

the unitary transformation matrices of the previous NRG iteration.

$$\begin{aligned}
& {}_{N+1}\langle Q, S_{tot}^z, S_{ch}^z, w | f_{N+1,+,\uparrow}^\dagger | Q', S_{tot}^z, S_{ch}^z, w' \rangle_{N+1} \\
&= \sum_r [U_{QN1}^\top(w, r2) U_{QN2}(w', r1) \\
&\quad + U_{QN1}^\top(w, r7) U_{QN2}(w', r4) \\
&\quad + U_{QN1}^\top(w, r6) U_{QN2}(w', r3) \\
&\quad + U_{QN1}^\top(w, r12) U_{QN2}(w', r8) \\
&\quad + U_{QN1}^\top(w, r9) U_{QN2}(w', r5) \\
&\quad + U_{QN1}^\top(w, r14) U_{QN2}(w', r11) \\
&\quad + U_{QN1}^\top(w, r13) U_{QN2}(w', r10) \\
&\quad + U_{QN1}^\top(w, r16) U_{QN2}(w', r15)]
\end{aligned}$$

with $QN1 \equiv (Q, S_{tot}^z, S_{ch}^z)$ and $QN2 \equiv (Q - 1, S_{tot}^z - \frac{1}{2}, S_{ch}^z - \frac{1}{2})$.

$$\begin{aligned}
& {}_{N+1}\langle Q, S_{tot}^z, S_{ch}^z, w | f_{N+1,+,\downarrow}^\dagger | Q', S_{tot}^z, S_{ch}^z, w' \rangle_{N+1} \\
&= \sum_r [U_{QN1}^\top(w, r4) U_{QN2}(w', r1) \\
&\quad - U_{QN1}^\top(w, r7) U_{QN2}(w', r2) \\
&\quad + U_{QN1}^\top(w, r8) U_{QN2}(w', r3) \\
&\quad - U_{QN1}^\top(w, r12) U_{QN2}(w', r6) \\
&\quad + U_{QN1}^\top(w, r11) U_{QN2}(w', r5) \\
&\quad - U_{QN1}^\top(w, r14) U_{QN2}(w', r9) \\
&\quad + U_{QN1}^\top(w, r15) U_{QN2}(w', r10) \\
&\quad - U_{QN1}^\top(w, r16) U_{QN2}(w', r13)]
\end{aligned}$$

with $QN1 \equiv (Q, S_{tot}^z, S_{ch}^z)$ and $QN2 \equiv (Q - 1, S_{tot}^z + \frac{1}{2}, S_{ch}^z - \frac{1}{2})$.

$$\begin{aligned}
& {}_{N+1}\langle Q, S_{tot}^z, S_{ch}^z, w | f_{N+1,-,\uparrow}^\dagger | Q', S_{tot}'^z, S_{ch}'^z, w' \rangle_{N+1} \\
&= \sum_r [U_{QN1}^\top(w, r3) U_{QN2}(w', r1) \\
&\quad - U_{QN1}^\top(w, r6) U_{QN2}(w', r2) \\
&\quad - U_{QN1}^\top(w, r8) U_{QN2}(w', r4) \\
&\quad + U_{QN1}^\top(w, r12) U_{QN2}(w', r7) \\
&\quad + U_{QN1}^\top(w, r10) U_{QN2}(w', r5) \\
&\quad - U_{QN1}^\top(w, r13) U_{QN2}(w', r9) \\
&\quad - U_{QN1}^\top(w, r15) U_{QN2}(w', r11) \\
&\quad + U_{QN1}^\top(w, r16) U_{QN2}(w', r14)]
\end{aligned}$$

with $QN1 \equiv (Q, S_{tot}^z, S_{ch}^z)$ and $QN2 \equiv (Q - 1, S_{tot}^z - \frac{1}{2}, S_{ch}^z + \frac{1}{2})$.

$$\begin{aligned}
& {}_{N+1}\langle Q, S_{tot}^z, S_{ch}^z, w | f_{N+1,-,\downarrow}^\dagger | Q', S_{tot}'^z, S_{ch}'^z, w' \rangle_{N+1} \\
&= \sum_r [U_{QN1}^\top(w, r5) U_{QN2}(w', r1) \\
&\quad - U_{QN1}^\top(w, r9) U_{QN2}(w', r2) \\
&\quad - U_{QN1}^\top(w, r11) U_{QN2}(w', r4) \\
&\quad + U_{QN1}^\top(w, r14) U_{QN2}(w', r7) \\
&\quad - U_{QN1}^\top(w, r10) U_{QN2}(w', r3) \\
&\quad + U_{QN1}^\top(w, r13) U_{QN2}(w', r6) \\
&\quad + U_{QN1}^\top(w, r15) U_{QN2}(w', r8) \\
&\quad - U_{QN1}^\top(w, r16) U_{QN2}(w', r12)]
\end{aligned}$$

with $QN1 \equiv (Q, S_{tot}^z, S_{ch}^z)$ and $QN2 \equiv (Q - 1, S_{tot}^z + \frac{1}{2}, S_{ch}^z + \frac{1}{2})$.

To summarize, for one NRG iteration one has to diagonalize the Hamiltonians of each $|Q, S_{tot}^z, S_{ch}^z\rangle$ subspace and store the resulting eigenstates and eigenvectors. As already the smallest channel anisotropy destabilizes the 2CK non-Fermi liquid fixed point one has to look carefully at the energy level flow. In our 2CK NRG program the truncation procedure is adopted such that the cutoff of the eigenstates does not happen right within a degenerate level: If the last energy level, which is kept for the next iteration, is degenerate, then only eigenstates with higher energy are truncated. In

our calculation, it was sufficient to retain about 900 states at each iteration for $\Lambda = 3$. For calculation the free conduction electron chain, the higher degree of degeneracy made it necessary to keep as many as about 3000 states.

List of Abbreviations

1CK	One-channel Kondo
2CK	Two-channel Kondo
BA	Bethe ansatz
CB	Conduction band
CF	Crystal-field
CPU	Central processing unit
CTMA	Conserving T -matrix approximation
D	Conduction electron bandwidth
DFT	Density functional theory
dI/dV	Differential conductance
DMFT	Dynamical mean-field theory
DMRG	Density matrix renormalization group
DoS	Density of states
E_F	Fermi energy
FL	Fermi liquid
FP	Fixed point
GC	Grand-canonical
IPES	Inverse photoemission spectroscopy
LDoS	Local density of states
LSDA	Local spin-density approach
NCA	Non-crossing approximation
NRG	Numerical renormalization group
PES	Photoemission spectroscopy
QD	Quantum dot
RG	Renormalization group
SIAM	Single impurity Anderson model
SO	Spin-orbit
STM	Scanning tunneling microscopy
STS	Scanning tunneling spectroscopy
SUNCA	Symmetrized finite- U NCA
T_K	Kondo temperature
TLS	Two-level system

List of publications

Parts of the results of this thesis are published in the following papers:

Comment on “Fano Resonance for Anderson Impurity Systems”
Ch. Kolf, J. Kroha, M. Ternes, W. -D. Schneider,
Phys. Rev. Lett. **96**, 019701 (2006)

“Orbital geometry and electronic transport through Kondo atoms”
Ch. Kolf, J. Kroha, P. Mavropoulos,
preprint, to be submitted to Nature Physics

*“Strong vs. Weak Coupling Duality and Coupling Dependence
of the Kondo Temperature in the Two-Channel Kondo Model”*
Christian Kolf and Johann Kroha,
Preprint, Electronic archive, [http://arxiv.org/abs/cond-mat,
cond-mat/0610631](http://arxiv.org/abs/cond-mat,cond-mat/0610631), submitted to Physical Review B

During the time of my PhD studies, amongst others the following paper related to my diploma thesis was published:

Drift chamber with a c-shaped frame
J. Smyrski, Ch. Kolf et al.,
Nucl. Instrum. Meth. **A541**, 574-582 (2005)

Bibliography

- [1] A. C. Hewson. *The Kondo Problem to Heavy Fermions*. Cambridge University Press (1993).
- [2] J. Kondo. *Resistance Minimum in Dilute magnetic Alloys*. Prog. Theor. Phys., **32** (1964) 37.
- [3] K. G. Wilson. *The renormalization group: Critical phenomena and the Kondo problem*. Rev. Mod. Phys., **47** (1975) 773–840.
- [4] W. J. de Haas, J. H. de Boer, and G. J. van den Berg. *The electrical resistance of gold, copper and lead at low temperatures*. Physica, **1** (1934) 1115.
- [5] P. W. Anderson. *Localized Magnetic States in Metals*. Phys. Rev. , **124** (1961) 41.
- [6] J. R. Schrieffer and P. A. Wolff. *Relation between the Anderson and Kondo Hamiltonians*. Phys. Rev. , **149** (1966) 491.
- [7] P. W. Anderson. *A poor man's derivation for the scaling laws of the Kondo problem*. J. Phys. C, **3** (1970) 2436.
- [8] K. G. Wilson and J. Kogut. *The renormalization group and the ϵ expansion*. Phys. Rep., **12** (1974) 75–199.
- [9] H. R. Krishna-murthy, J. W. Wilkins, and K. G. Wilson. *Renormalization-group approach to the Anderson model of dilute magnetic alloys. I. Static properties for the symmetric case*. Phys. Rev. B, **21** (1980) 1003–1043.
- [10] H. R. Krishna-murthy, J. W. Wilkins, and K. G. Wilson. *Renormalization-group approach to the Anderson model of dilute magnetic alloys. II. Static properties for the asymmetric case*. Phys. Rev. B, **21** (1980) 1044–1083.
- [11] N. Andrei, K. Furuya, and J. H. Lowenstein. *Solution of the Kondo problem*. Rev. Mod. Phys., **55** (1983) 331.
- [12] P. B. Wiegmann. *Exact solution of s-d exchange model at $T=0$* . Pis'ma Zh. Eksp. Teor. Fiz., **31** (1983) 392.

- [13] L. Kouwenhoven and L. Glazman. *Revival of the Kondo effect*. Physics World (January 2001), (2001) 33–38.
- [14] D. Goldhaber-Gordon et al. *Kondo effect in a single-electron transistor*. Nature, **391** (1998) 156–159.
- [15] L. I. Glazman and M. E. Raikh. *Resonant Kondo transparency of a barrier with quasilocal impurity states*. JETP Lett., **47** (1988) 452.
- [16] T. K. Ng and P. A. Lee. *On-site Coulomb repulsion and resonant tunneling*. Phys. Rev. Lett., **61** (1988) 1768–1771.
- [17] W. G. van der Wiel et al. *The Kondo Effect in the Unitary Limit*. Science, **289** (2000) 2105.
- [18] D. Goldhaber-Gordon et al. *From the Kondo regime to the Mixed-Valence Regime in a single-electron transistor*. Phys. Rev. Lett., **81** (1998) 5225.
- [19] V. Madhavan et al. *Tunneling into a Single Magnetic Atom: Spectroscopic Evidence of the Kondo Resonance*. Science, **280** (1998) 567.
- [20] J. Li, et al. *Kondo Scattering Observed at a Single Magnetic Impurity*. Phys. Rev. Lett., **80** (1998) 2893–2896.
- [21] Picture created by Don Eigler, IBM. Taken from the IBM website at http://www.almaden.ibm.com/almaden/media/image_mirage.html.
- [22] H. C. Manoharan et al. *Quantum mirages formed by coherent projection of electronic structure*. Nature, **403** (2000) 512.
- [23] J. Kroha and P. Wölfle. *Conserving Diagrammatic Approximations for Quantum Impurity Models: NCA and CTMA*. J. Phys. Soc. Jpn., **74** (2005) 16–26.
- [24] H. Bethe. *Eigenwerte und Eigenfunktionen der linearen Atomkette*. Z. Phys., **71** (1931) 205.
- [25] N. Andrei. *Diagonalization of the Kondo Hamiltonian*. Phys. Rev. Lett., **45** (1980) 379.
- [26] A. M. Tsvelick and P. B. Wiegmann. *Exact results in the theory of magnetic alloys*. Adv. Phys., **32** (1983) 453–713.
- [27] N. Andrei and C. Destri. *Solution of the Multichannel Kondo Problem*. Phys. Rev. Lett., **52** (1984) 364.
- [28] A. M. Tsvelick and P. B. Wiegmann. *Solution of the n -channel Kondo problem (scaling and integrability)*. Z. Phys. B, **54** (1984) 201–206.

- [29] S. R. White. *Density matrix formulation for quantum renormalization groups*. Phys. Rev. Lett., **69** (1992) 2863–2866.
- [30] S. R. White. *Density-matrix algorithms for quantum renormalization groups*. Phys. Rev. Lett., **48** (1993) 10345.
- [31] I. Peschel et al., editors. *Lecture Notes in Physics Vol. 528: Density Matrix Renormalization*. Springer Verlag (1999).
- [32] T. Costi, J. Kroha, and P. Wölfle. *Spectral properties of the Anderson impurity model: Comparison of numerical-renormalization-group and noncrossing-approximation results*. Phys. Rev. B, **53** (1996) 1850.
- [33] G. Baym and L. P. Kadanoff. *Conservation Laws and Correlation Functions*. Phys. Rev. , **124** (1961) 287.
- [34] G. Baym. *Self-Consistent Approximations in Many-Body Systems*. Phys. Rev. , **127** (1962) 1391.
- [35] S. Kirchner and J. Kroha. *Self-consistent Conserving Theory for Quantum Impurity Systems: Renormalization Group Analysis*. J. Low Temp. Phys., **126** (2002) 1233.
- [36] N. Bickers. *Review of techniques in the large- N expansion for dilute magnetic alloys*. Rev. Mod. Phys., **59** (1987) 845.
- [37] K. Haule et al. *Anderson impurity model at finite Coulomb interaction U : Generalized noncrossing approximation*. Phys. Rev. B, **64** (2001) 155111.
- [38] F. Reinert et al. *Temperature dependence of the Kondo resonance and its satellites in $CeCu_2Si_2$* . Phys. Rev. Lett., **87** (2001) 106401.
- [39] H. O. Frota and L. N. Oliveira. *Photoemission spectroscopy for the spin-degenerate Anderson model*. Phys. Rev. B, **33** (1986) 7871.
- [40] O. Sakai, Y. Shimizu, and T. Kasuya. *Single-Particle and Magnetic Excitation Spectra of Degenerate Anderson Model with Finite $f - f$ Coulomb Interaction*. J. Phys. Soc. Jpn., **58** (1989) 3666.
- [41] T. A. Costi and A. C. Hewson. *Resistivity cross-over for the non-degenerate Anderson model*. Philos. Mag. B, **65** (1992) 1165.
- [42] T. A. Costi and A. C. Hewson. *Transport coefficients of the Anderson model*. J. Phys. Condens. Matter, **5** (1993) L361.

-
- [43] T. A. Costi, A. C. Hewson, and V. Zlatić. *Transport coefficients of the Anderson model via the numerical renormalization group*. J. Phys. Condens. Matter, **6** (1994) 2519–2558.
- [44] R. Bulla. *Entwicklung neuer Methoden zur Untersuchung des Anderson-Modells*. Dissertation, Universität Regensburg (1994).
- [45] R. Bulla, T. Pruschke, and A. C. Hewson. *Anderson impurity in pseudo-gap Fermi systems*. J. Phys. Condensed Matter, **9** (1997) 10463–10474.
- [46] W. Hofstetter. *Renormalization Group Methods for Quantum Impurity Systems*. Dissertation, Universität Augsburg (2000).
- [47] M. Sindel. *Numerical Renormalization Group studies of Quantum Impurity Models in the Strong Coupling Limit*. Dissertation, Ludwig-Maximilians-Universität München (2004).
- [48] K. Chen and C. Jayaprakash. *X-ray-edge singularities with nonconstant density of states: A renormalization-group approach*. Phys. Rev. B, **52** (1995) 14436–14440.
- [49] C. Lánczos. *An Iteration Method for the Solution of the Eigenvalue Problem of Linear Differential and Integral Operators*. J. Res. Natl. Bur. Stand., **45** (1950) 255.
- [50] D. L. Cox and A. Zawadowski. *Exotic Kondo Effects in Metals: Magnetic Ions in a Crystalline Electric Field and Tunneling Centers*. Adv. Phys., **47** (1998) 599.
- [51] S. C. Costa et al. *Numerical renormalization-group computation of specific heats*. Phys. Rev. B, **55** (1997) 30.
- [52] W. C. Oliveira and L. N. Oliveira. *Generalized numerical renormalization-group method to calculate the thermodynamical properties of impurities in metals*. Phys. Rev. B, **49** (1994) 11986.
- [53] R. Bulla, T. A. Costi, and D. Vollhardt. *Finite-temperature numerical renormalization group study of the Mott transition*. Phys. Rev. B, **64** (2001) 045103.
- [54] D. C. Langreth. *Friedel sum rule for Anderson's Model of Localized Impurity States*. Phys. Rev. , **150** (1966) 516.
- [55] R. Bulla, A. C. Hewson, and T. Pruschke. *Numerical Renormalization Group Calculations for the Self-energy of the impurity Anderson model*. J. Phys. Condensed Matter, **10** (1998) 8365.
- [56] J. Martinek et al. *Gate-controlled spin splitting in quantum dots with ferromagnetic leads in the Kondo regime*. Phys. Rev. B, **72** (2005) 121302.

- [57] W. Hofstetter. *Generalized Numerical Renormalization Group for Dynamical Quantities*. Phys. Rev. Lett. , **85** (2000) 1508.
- [58] R. Bulla et al. *Numerical Renormalization Group for Quantum Impurities in a Bosonic Bath*. Phys. Rev. B, **71** (2005) 045122.
- [59] F. B. Anders and A. Schiller. *Real-Time Dynamics in Quantum-Impurity Systems: A Time-Dependent Numerical Renormalization-Group Approach*. Phys. Rev. Lett., **95** (2005) 196801.
- [60] F. B. Anders and A. Schiller. *Spin Precession and Real Time Dynamics in the Kondo model: A Time-Dependent Numerical Renormalization-Group Study*. Electronic archive, <http://arxiv.org/abs/cond-mat>, cond-mat/0604517.
- [61] T. A. Costi. *Renormalization-group approach to nonequilibrium Green functions in correlated impurity systems*. Phys. Rev. B, **55** (1997) 003003.
- [62] F. B. Anders. *Real-time dynamics of a single spin coupled to Fermionic and Bosonic Baths: A time-dependent numerical renormalization group study*. Talk given at the Non-equilibrium Dynamics in Interacting Systems (NEQDIS) workshop in Dresden, April/May 2006.
- [63] A. Georges, et al. *Dynamical mean-field theory of strongly correlated fermion systems and the limit of infinite dimensions*. Rev. Mod. Phys., **68** (1996) 13.
- [64] W. Metzner and D. Vollhardt. *Correlated Lattice Fermions in $d = \infty$ Dimensions*. Phys. Rev. Lett. , **62** (1989) 324.
- [65] G. Kotliar and D. Vollhardt. *Strongly Correlated Materials: Insights from Dynamical Mean-Field Theory*. Physics Today, **57** (2006) 53.
- [66] R. Bulla. *Dynamical mean-field theory: from quantum impurity physics to lattice problems*. Phil. Mag. , **86** (2006) 1877.
- [67] M. Arnold and J. Kroha. *Simultaneous ferromagnetic and semiconductor-metal transition in EuO* , article submitted to Physica C.
- [68] P. Nozières and A. Blandin. *Kondo effect in real metals*. Journal de Physique (Paris), **41** (1980) 193–211.
- [69] D. M. Cragg, P. Lloyd, and P. Nozières. *On the ground states of some s-d exchange Kondo Hamiltonians*. J. Phys. C, **13** (1980) 803–817.
- [70] H. B. Pang and D. L. Cox. *Stability of the fixed point of the two-channel Kondo Hamiltonian*. Phys. Rev. B, **44** (1991) 9454–9457.

- [71] P. Nozières. *A "fermi-liquid" description of the Kondo problem at low temperatures*. J. Low Temp. Phys., **17** (1974) 31–42.
- [72] I. Affleck and A. W. Ludwig. *Exact conformal-field-theory results on the multichannel Kondo effect: Single-fermion Green's function, self-energy, and resistivity*. Phys. Rev. B, **48** (1993) 7297–7321.
- [73] Y. Oreg and D. Goldhaber-Gordon. *Two-Channel Kondo Effect in a Modified Single Electron Transistor*. Phys. Rev. Lett., **90** (2003) 136602.
- [74] D. L. Cox. *Quadrupolar Kondo effect in uranium heavy-electron materials*. Phys. Rev. Lett., **59** (1987) 1240.
- [75] D. C. Ralph and R. A. Buhrmann. *Observation of Kondo Scattering without Magnetic Impurities: A Point Contact Study of Two-Level Tunneling Systems in Metals*. Phys. Rev. Lett., **69** (1992) 2118.
- [76] D. C. Ralph et al. *2-Channel Kondo Scaling in Conductance Signals from 2-Level Tunneling Systems*. Phys. Rev. Lett., **72** (1994) 1064.
- [77] D. C. Ralph and R. A. Buhrmann. *Kondo scattering from atomic two-level tunneling systems in metals: Enhanced conductance, critical-bias transitions, and the non-Fermi-liquid electronic state*. Phys. Rev. B, **51** (1995) 3554.
- [78] M. H. Hettler, J. Kroha, and S. Hershfield. *Nonlinear Conductance for the Two Channel Anderson Model*. Phys. Rev. Lett., **73** (1994) 1967.
- [79] M. Arnold and T. Langenbruch. Diploma theses at the Physics Institute, Universität Bonn.
- [80] I. Affleck et al. *Relevance of anisotropy in the multichannel Kondo effect: Comparison of conformal field theory and numerical renormalization-group results*. Phys. Rev. B, **45** (1992) 7918–7935.
- [81] B. A. Jones. Dissertation, Cornell University (1988).
- [82] B. A. Jones and C. M. Varma. *Study of two magnetic impurities in a Fermi gas*. Phys. Rev. Lett., **58** (1987) 843–846.
- [83] B. A. Jones, C. M. Varma, and J. W. Wilkins. *Low-Temperature Properties of the Two-Impurity Kondo Hamiltonian*. Phys. Rev. Lett., **61** (1988) 125–128.
- [84] C. Kolf and J. Kroha. *Strong vs. Weak Coupling Duality and Coupling Dependence of the Kondo Temperature in the Two-Channel Kondo Model*. Preprint, Electronic archive, <http://arxiv.org/abs/cond-mat>, cond-mat/0610631, submitted to Phys. Rev. B.

- [85] I. E. Perakis and C. M. Varma. *Non-Fermi-Liquid States of a Magnetic Ion in a Metal*. Phys. Rev. Lett., **70** (1993) 3467–3470.
- [86] I. E. Perakis and C. M. Varma. *Non-Fermi-liquid states of a magnetic ion in a metal: Particle-hole symmetric case*. Phys. Rev. B, **49** (1994) 9041–9051.
- [87] U. Fano. *Effects of Configuration Interaction on Intensities and Phase Shifts*. Phys. Rev., **124** (1961) 1866.
- [88] T. Jamneala et al. *Scanning tunneling spectroscopy of transition-metal impurities at the surface of gold*. Phys. Rev. B, **61** (2000) 9990.
- [89] K. Nagaoka et al. *Temperature Dependence of a Single Kondo Impurity*. Phys. Rev. Lett., **88** (2002) 077205.
- [90] O. Újsághy et al. *Theory of the Fano Resonance in the STM Tunneling Density of States due to a Single Kondo Impurity*. Phys. Rev. Lett., **85** (2000) 2557.
- [91] H. G. Luo et al. *Fano Resonance for Anderson Impurity Systems*. Phys. Rev. Lett., **92** (2004) 256602.
- [92] C. Kolf, et al. *Comment on "Fano Resonance for Anderson Impurity Systems"*. Phys. Rev. Lett., **96** (2006) 019701.
- [93] H. G. Luo et al. *Luo et al. Reply*. Phys. Rev. Lett., **96** (2006) 019702.
- [94] N. Papanikolaou, R. Zeller, and P. H. Dederichs. *Conceptual improvements of the KKR method*. J. Phys. Condens. Matter, **14** (2002) 2799.
- [95] C. Kolf, J. Kroha, and P. Mavropoulos. *Orbital geometry and electronic transport through single Kondo atoms*, to be submitted to Nature Physics.
- [96] R. Bulla. *private communication*.